



Skukauskas, Vainius (2024) *Investigating the dynamics of species relevant to the partial oxidation of methane using neutrons & muons*. PhD thesis

<https://theses.gla.ac.uk/84759/>

Copyright and moral rights for this work are retained by the author

A copy can be downloaded for personal non-commercial research or study, without prior permission or charge

This work cannot be reproduced or quoted extensively from without first obtaining permission in writing from the author

The content must not be changed in any way or sold commercially in any format or medium without the formal permission of the author

When referring to this work, full bibliographic details including the author, title, awarding institution and date of the thesis must be given

Enlighten: Theses

<https://theses.gla.ac.uk/>  
[research-enlighten@glasgow.ac.uk](mailto:research-enlighten@glasgow.ac.uk)



# University of Glasgow

## **Investigating the Dynamics of Species Relevant to the Partial Oxidation of Methane using Neutrons & Muons**

Vainius Skukauskas

School of Chemistry

College of Science & Engineering

University of Glasgow

August 2024

*Submitted in fulfilment of the requirements for the degree of  
Doctor of Philosophy*

I hereby declare that this thesis, presented in fulfilment of the requirements for the Doctor of Philosophy degree, is my own work except where due reference is made; and that this work has not been submitted for any other degree at this or any other institution.

Vainius Skukauskas,

University of Glasgow

# Acknowledgements

---

First and foremost, I would like to express my deepest thanks to my supervisors, Dr Emma K. Gibson and Dr Ian P. Silverwood, for their invaluable guidance, support and encouragement throughout this whole research project. Your patience and dedication have been instrumental in getting me here, and I am profoundly grateful for your mentorship and the opportunities you have provided me.

A sincere thank you goes to my colleagues at the UK Catalysis Hub and ISIS Neutron & Muon Source. You have made this journey – with all its highs and lows – an incredible experience, and I am thankful to have worked with all of you. I particularly want to extend my gratitude to Dr Adam Berlie. Your help and guidance through the world of muons, as well as your unparalleled enthusiasm, have been invaluable. I would also like to thank Dr June Callison and Dr Ines Lezcano-Gonzalez. Your support over the last few years has been immeasurable; and working alongside you unforgettable.

Of course, I must also thank my incredible friends who have been with me throughout this whole journey. Rebecca, Maxamilian, Jessica, Marco, Samson, Isidro and David – there is no word big enough to describe how much I value you; but know that I would not be here without you.

Finally, to my family, I want to thank you for your unwavering support. Your belief in me and your constant encouragement have been a driving force behind all my efforts. I dedicate this work to you all.

# Abstract

---

The partial oxidation of methane over copper loaded zeolites represents a rapidly evolving field of research due to the growing understanding of the complex challenges associated with optimising and implementing an industrially-viable process. However, there is a paucity of literature regarding the dynamics of the various species involved in this reaction within Cu-loaded zeolite catalysts. This study investigates such dynamics, focusing on methane, methanol, water and copper within zeolites mordenite, SSZ-13 and ZSM-5.

Quasielastic neutron scattering enabled insights into the dynamics of water, methane and methanol within the Cu-doped zeolites. At low temperatures, water was found to be immobile; however, as the temperature was increased, rotational and translational dynamics were observed, particularly at 300 K. Methanol adsorbed onto the three zeolites displayed non-Arrhenius behaviour, with varying jump lengths, residence times and diffusion constants. These results have implicated multiple, concurrent processes taking place, such as clustering around cationic sites and methoxylation, influenced by the presence of copper. Probing the dynamics of methane resulted in no observable motions, likely due to challenges in methane adsorption or inherently low uptake under the experimental conditions used. Neutron diffraction complemented the findings by revealing how the zeolitic framework responds to the adsorption of water and methane. The former induced significant structural changes characterised by anisotropic expansion and contraction of the zeolite framework; whilst the latter resulted in minimal observable changes.

Muon spectroscopy is presented as a novel approach for the study of metal ion dynamics within zeolite hosts. Transverse and longitudinal field measurements showed significant differences in muon relaxation rates between the pure and Cu-doped zeolites, suggesting dynamic processes associated with the copper ions. The formation of muonium and its temperature-dependent interaction with Cu(II) species highlighted the electronic and magnetic influences of copper ions; and temperature-dependent longitudinal field measurements have indicated processes involving copper dynamics or the redox behaviour thereof.

The integration of neutron and muon techniques presents a comprehensive approach to understanding the behaviour of various species within microporous materials, paving the way for enhanced methane-to-methanol conversion processes and broader applications in catalysis.

# Publications

---

The work carried out during this doctoral program has been published in the following papers:

Skukauskas, V.; De Souza, N.; Silverwood, I. P.; Gibson, E. K. Probing the dynamics of methanol in copper-loaded zeolites via quasi-elastic and inelastic neutron scattering. *Front. Chem. Sci. Eng.* 2024, <https://doi.org/10.1007/s11705-024-2506-1>.

Skukauskas, V.; Silverwood, I. P.; Gibson, E. K. Dynamics of Water within Cu-Loaded Zeolites: A Quasielastic Neutron Scattering Study. *Catal. Commun.* 2022, *165*, 106429. <https://doi.org/10.1016/j.catcom.2022.106429>.

Skukauskas, V.; Johnson Humphrey, E. L. B.; Hitchcock, I.; York, A.; Kelleher, J.; Gibson, E. K.; Nelson, D. J.; Silverwood, I. P. Operando Neutron Scattering: Following Reactions in Real Time Using Neutrons. *Top. Catal.* 2021, *64* (9–12), 693–698. <https://doi.org/10.1007/s11244-021-01436-x>.

Additional work carried out in the course of this project has contributed to the following publications:

Panchal, M.; Callison, J.; Skukauskas, V.; Gianolio, D.; Cibin, G.; York, A. P. E.; Schuster, M. E.; Hyde, T. I.; Collier, P.; Catlow, C. R. A.; Gibson, E. K. Operando XAFS Investigation on the Effect of Ash Deposition on Three-Way Catalyst Used in Gasoline Particulate Filters and the Effect of the Manufacturing Process on the Catalytic Activity. *J. Phys. Condens. Matter* **2021**, *33* (28). <https://doi.org/10.1088/1361-648X/abfe16>.

Inns, D. R.; Mayer, A. J.; Skukauskas, V.; Davies, T. E.; Callison, J.; Kondrat, S. A. Evaluating the Activity and Stability of Perovskite LaMO<sub>3</sub>-Based Pt Catalysts in the Aqueous Phase Reforming of Glycerol. *Top. Catal.* **2021**, *64* (17–20), 992–1009. <https://doi.org/10.1007/s11244-021-01449-6>.

# Contents

---

Chapter 1.....	11
1.1    Zeolites .....	14
1.2    Partial Oxidation of Methane.....	16
1.3    Nature of the Active Sites. ....	19
1.4    Number & Distribution of Active Sites .....	20
1.5    Reaction Mechanism.....	22
1.6    Reactivity & Yield.....	23
1.7    Project Aims.....	25
1.8    Bibliography.....	26
Chapter 2.....	36
2.1    Neutron Scattering .....	36
2.1.1    Elementary Principles of Scattering .....	39
2.1.2    Neutron Production & Transportation.....	43
2.1.3    Inelastic Neutron Scattering (INS) Spectroscopy .....	45
2.1.4    Quasielastic Neutron Scattering (QENS).....	47
2.2    Muon Spectroscopy.....	55
2.2.1    Muon Properties & Production.....	56
2.2.2    Muon Implantation.....	58
2.2.3    Muon Experimentation .....	59
2.2.4    Muon Spin Relaxation Functions.....	60
2.2.5    Muon Sources & Instrumentation .....	61
2.3    Materials & Characterisation.....	64
2.3.1    Copper loading .....	65
2.3.2    Brunauer-Emmett-Teller (BET) Surface Area Analysis <sup>25</sup> .....	65
2.3.3    Diffraction <sup>26</sup> .....	67
2.3.4    Diffuse Reflectance Infrared Fourier-transform Spectroscopy (DRIFTS) <sup>27</sup> .....	68
2.3.5    Solid State Nuclear Magnetic Resonance (ssNMR) <sup>28</sup> .....	69
2.3.6    Magnetisation Measurements <sup>29</sup> .....	71
2.3.7    Thermogravimetric Analysis (TGA) <sup>30</sup> .....	72
2.3.8    X-Ray Absorption Near Edge Fine Structure (XANES) <sup>31</sup> .....	72
2.3.9    X-Ray Fluorescence (XRF) <sup>32</sup> .....	73

2.4	Activity Testing	74
2.4.1	Reactor Setup	74
2.4.2	Conditions	75
2.4.3	Mass Spectrometry <sup>33</sup>	75
2.5	Bibliography	76
Chapter 3		80
3.1	Material Preparation	80
3.2	Activity	81
3.2.1	Hidden Catlab Microreactor	81
3.2.2	Multi-capillary Reactor	82
3.2.3	DRIFTS	82
3.2.4	Custom Setup	85
3.3	Copper Speciation	89
3.3.1	Cu-self reduction	89
3.3.2	XANES	91
3.4	Structural Changes	95
3.4.1	Surface Area	95
3.4.2	Dealumination	96
3.5	Bibliography	99
Chapter 4		101
4.1	Dynamics of Water	102
4.1.1	Motivation	102
4.1.2	Experimental	102
4.1.3	Results & Discussion	104
4.1.4	Conclusions	109
4.2	Dynamics of Methane	110
4.2.1	Motivation	110
4.2.2	Experimental	110
4.2.3	Results & Discussion	111
4.2.4	Conclusions	113
4.3	Dynamics of Methanol	114
4.3.1	Motivation	114
4.3.2	Experimental	114
4.3.3	Results & Discussion	116

4.3.4	Conclusions .....	120
4.4	Neutron Diffraction .....	120
4.4.1	Experimental .....	121
4.4.2	Results & Discussion.....	121
4.4.3	Conclusions .....	124
4.5	Summary .....	125
4.6	Bibliography .....	125
Chapter 5	.....	131
5.1	Introduction .....	131
5.2	Experimental.....	131
5.2.1	Zeolite Preparation.....	131
5.2.2	Magnetisation Measurements.....	132
5.2.3	Muon Spin Spectroscopy .....	132
5.3	Results & Discussion .....	133
5.3.1	Transverse Field (TF) $\mu$ SR .....	134
5.3.2	Longitudinal Field (LF) $\mu$ SR .....	136
5.3.3	Temperature Dependence in ZF and LF .....	139
5.3.4	Magnetisation Data.....	142
5.4	Conclusions .....	144
5.5	Bibliography .....	144
Chapter 6	.....	147
6.1	Conclusions .....	147
6.2	Future Work.....	152

# List of Figures

---

<b>Figure 1.1</b> Concept of methane activation over reactive metal-oxygen species. .....	<b>14</b>
<b>Figure 1.2</b> Framework structures of zeolites Mordenite, SSZ-13 and ZSM-5, respectively.....	<b>15</b>
<b>Figure 1.3</b> Schemes for the partial oxidation of methane over Cu-zeolites....	<b>16</b>
<b>Figure 1.4</b> Some of the proposed active sites in Cu-zeolites and MMOs.....	<b>19</b>
<b>Figure 1.5</b> Two proposed reaction pathways in the MTM conversion over Cu-Zeolites.....	<b>22</b>
<b>Figure 2.1.1</b> Schematic representation of the principal interactions between condensed matter and electrons, neutrons and X-rays.....	<b>37</b>
<b>Figure 2.1.2</b> Schematic illustration of the scattering process.....	<b>39</b>
<b>Figure 2.1.3</b> Wavevector diagrams for elastic and inelastic scattering through an angle of $2\theta$ . .....	<b>40</b>
<b>Figure 2.1.4</b> Schematic of the OPAL fission reactor at ANSTO.....	<b>43</b>
<b>Figure 2.1.5</b> Schematic of the ISIS Neutron & Muon Source in Harwell, UK.	<b>44</b>
<b>Figure 2.1.6</b> Q-dependencies of $\Gamma$ according to different diffusion models. ..	<b>49</b>
<b>Figure 2.1.7</b> Schematic of the IRIS Spectrometer at the ISIS Neutron & Muon Source .....	<b>53</b>
<b>Figure 2.1.8</b> Schematic of the EMU Spectrometer at ANSTO.....	<b>54</b>
<b>Figure 2.2.1</b> Positrons are preferentially emitted along the muon spin direction, indicated by the length of each grey arrow.....	<b>57</b>
<b>Figure 2.2.2</b> Thermalisation of surface muons post-implantation.....	<b>58</b>
<b>Figure 2.2.3</b> Precession of the muon spin. ....	<b>60</b>
<b>Figure 2.2.4</b> The EMU Spectrometer at the ISIS Neutron & Muon Source.....	<b>63</b>
<b>Figure 2.2.5</b> Schematic of the GPS Spectrometer at the Paul Scherrer Institut, Villigen, Switzerland.....	<b>64</b>
<b>Figure 3.1.1</b> PXRD patterns of protonic and Cu-loaded zeolites. ....	<b>80</b>
<b>Figure 3.2.3</b> DRIFTS spectra obtained from CuMOR (A), CuSSZ13 (B) and CuZSM5 (C) during various stages of the methane-to-methanol conversion reaction.....	<b>83</b>
<b>Figure 3.2.4</b> Exemplar calibration curve used to quantify the methanol produced after reaction with Cu-SSZ13. ....	<b>86</b>
<b>Figure 3.2.5</b> Methanol response during the extraction stage of the first reaction cycle for each Cu-loaded zeolite.....	<b>87</b>

<b>Figure 3.2.6</b> MeOH production rates with (green) and without (blue) high-temperature oxygen activation. ....	<b>88</b>
<b>Figure 3.3.1</b> Desorption of CO from Cu-MOR (A), Cu-ZSM-5 (B) and Cu-SSZ-13 (C). ....	<b>90</b>
<b>Figure 3.3.2</b> XANES spectra of the samples after activation (A); reaction (B); and extraction (C) alongside the Cu(I) and Cu(II) reference spectra. ....	<b>93</b>
<b>Figure 3.3.3</b> Data and linear combination fits to CuMOR (top), CuSSZ-13 (middle), and CuZSM-5 (bottom) collected after reaction with methane. ....	<b>94</b>
<b>Figure 3.4.1</b> Adsorption and desorption isotherms for nitrogen on H-mordenite. ....	<b>95</b>
<b>Figure 3.4.2</b> <sup>27</sup> Al MAS-NMR spectra of the protonated and Cu-doped zeolites. (A) refers to activated sample; (B) sample after one reaction cycle; and (C) sample after five reaction cycles. ....	<b>98</b>
<b>Figure 4.1.1</b> PXRD patterns of protonic and Cu-loaded zeolites. ....	<b>103</b>
<b>Figure 4.1.2</b> Data obtained from Cu-ZSM-5 at 100 K and the fit applied. ....	<b>104</b>
<b>Figure 4.1.3</b> Data obtained from CuMOR at 200 K and the fits applied. ....	<b>105</b>
<b>Figure 4.1.4</b> Lorentzian linewidths from fits to spectra measured at 200 K. ....	<b>101</b>
<b>Figure 4.1.5</b> Data obtained from Cu-SSZ-13 at 300 K and the fits applied. ...	<b>106</b>
<b>Figure 4.1.6</b> Lorentzian linewidths from fits to spectra measured at 300 K. ....	<b>107</b>
<b>Figure 4.1.7</b> Linewidths from spectra obtained at 300 K and fitted using a single Lorentzian and a flat background. ....	<b>108</b>
<b>Figure 4.2.1</b> Spectra obtained from the Cu-loaded and methane-dosed mordenite (A), SSZ-13 (B) and ZSM-5 (C) at 300 K and the fits applied. ....	<b>112</b>
<b>Figure 4.3.1</b> Fits applied to the data from CuMOR (a, d, g); CuSSZ13 (b, e, h); and CuZSM5 (c, f, i) at 375 K for Q values of 0.4 (a,b,c), 1.0 (d, e, f) and 1.8 Å <sup>-1</sup> (g, h, i). ....	<b>116</b>
<b>Figure 4.3.2</b> Lorentzian linewidths of the quasielastic component from the QENS spectra and the Singwi & Sjölander jump diffusion model applied. A, B, C and D correspond to data obtained at 300, 325, 350 and 375 K respectively. ....	<b>118</b>
<b>Figure 4.3.3</b> INS Spectra of Methanol adsorbed on the three zeolites at 350 K. ....	<b>119</b>
<b>Figure 4.4.1</b> Diffraction measurement from SSZ-13 catalyst as a function of time. Lines at 133 and 921 min show the termination of water dosing and the onset of heating respectively. ....	<b>1228</b>

<b>Figure 4.4.2</b> Neutron diffraction patterns obtained from Cu-MOR (A), Cu-SSZ-13 (B) and Cu-ZSM-5 (C) after activation and dosing with water and methane. ....	<b>123</b>
<b>Figure 5.1</b> Relaxation rates ( $\lambda$ ) and the initial asymmetries (%) obtained from the three zeolite samples as a function of temperature, measured in 100 G TF. ....	<b>134</b>
<b>Figure 5.2</b> Asymmetry as a function of longitudinal field (the datasets have been offset for clarity). B: the muon spin relaxation rate as a function of longitudinal field. ....	<b>136</b>
<b>Figure 5.3</b> Muon spin relaxation rates at zero-field (A) and longitudinal fields of 50 G (B), 500 G (C) and 2000 G (D) as a function of temperature for the Cu-DSSZ13, Cu-HSSZ13 and the DSSZ13. ....	<b>143</b>
<b>Figure 5.4</b> Data showing the magnetisation of both the deuterated Cu-SSZ13 and the deuterated SSZ13. ....	<b>143</b>

# Chapter 1

---

## Zeolites and the Partial Oxidation of Methane

The world's energy consumption has been on a steady rise over the last several decades, driven by a growing global population as well as industrialisation and urbanisation of developing countries. Indeed, a survey by the U.S. Department of Energy reported that global energy consumption is projected to increase by a staggering 44 % between 2006 and 2030.<sup>1</sup> However, since the majority of the world's energy comes from fossil fuels (coal, natural gas, petroleum), a rise in consumption is concomitantly accompanied by the increase in carbon dioxide (CO<sub>2</sub>), methane (CH<sub>4</sub>) and nitrous oxide (NO) emissions. These greenhouse gases (GHGs) contribute to trapping of heat in the lower atmosphere and the depletion of ozone, resulting in global warming, and thus climate change, which adversely affect the world's ecosystems.<sup>2</sup>

A significant portion of GHG emissions is attributed to methane, the simplest alkane which accounts for 70 – 90 % of natural gas and is the building block of a majority of organic compounds on earth. Its high calorific value enables methane to fuel households and chemical industries alike; from heating and cooking to gas-turbine electricity generation.<sup>3</sup> Its sources are copious too: methane is emitted naturally from wetlands, oceans and termites which account for around 40 % of the global total; and anthropogenically from fermentation, oil and gas, agriculture and landfill, amongst others, accounting for the remaining 60 %. This abundance of methane comes with a caveat as it is such a strong absorber and emitter of infrared (IR) radiation – which results in heat-trapping and subsequent formation of a thermal layer in the atmosphere – that it has a potential around 25 times greater than CO<sub>2</sub> at inducing climate change.<sup>2</sup> Furthermore, as the global methane budget consists of emissions from various sources, it is delicately balanced by several sinks such as destruction by moist soils; reaction with hydroxyl radicals in the troposphere; and reaction with chloride radicals in the stratosphere. As such, even a slight imbalance between the sources and sinks of methane can lead to alterations in its atmospheric levels, thus contributing to climate change.<sup>4</sup>

The deleterious effects of GHG emissions have propagated the global transition from petroleum-based energy economies to renewable energy societies. This transformation is, however, a gradual process with natural gas a key energy resource as it is the most copious form of fossil carbon and its combustion yields fewer GHG emissions than its coal or petroleum counterparts.<sup>5,6</sup> Alas, the utilisation of natural gas is thwarted due to its

reserves oft-situated in remote locations, making its transportation in both gaseous and liquefied forms logistically problematic.<sup>7</sup> This impracticality, coupled with methane's warming potential often renders flaring as the solitary option; hence, in 2012, a total of 143 billion cubic meters, or around \$20 billion in terms of market value, of natural gas were lost to flaring.<sup>8</sup>

It is therefore unsurprising that a process to valorise methane via its conversion to a more easily transportable and useful liquid fuel or chemical is highly sought after.<sup>7</sup> Methanol is the obvious choice of product in the pursuit of a direct and selective route of methane conversion as it is a precursor used in the synthesis of various other chemicals including formaldehyde, gasoline and olefins.<sup>9</sup> However, methane contains strong C–H bonds ( $\sim 440 \text{ kJ mol}^{-1}$ ), low polarity, low electron and proton affinity and a high ionisation energy; these attributes collectively make methane a highly stable and difficult-to-activate molecule. Oxidation permits both kinetic and thermodynamic activation, albeit the required reaction conditions lead to complete oxidation of methane to carbon dioxide and water rather than the more desirable methanol, which contains weaker C–H bonds ( $\sim 47 \text{ kJ mol}^{-1}$ ).<sup>10</sup>

The primary and, currently, the only economically viable method of methane-to-methanol conversion proceeds indirectly via the generation of syngas (a mixture of carbon monoxide and hydrogen) which is produced by reacting methane with steam or carbon dioxide. This process is typically carried out at high temperatures ( $\sim 1173 \text{ K}$ ) and pressures ( $>30 \text{ bar}$ ) in the presence of a nickel, cobalt, or iron-based catalyst. The syngas is then reacted with steam (at a lower  $\sim 673 \text{ K}$ ) in the presence of a copper-based catalyst (typically a mixture of copper, zinc, and aluminium oxides) to procure methanol. The catalysts used in the methanol synthesis process have different characteristics, depending on their composition and the method of preparation. For instance, catalysts containing a high percentage of copper have a higher activity for methanol production, while those containing a high percentage of zinc have a higher selectivity for methanol. Additionally, the catalyst's preparation method can affect its performance, with catalysts prepared using the precipitation method having a higher selectivity towards methanol than those prepared using the impregnation method.<sup>5</sup>

Such routes which are indirect and multi-stage operations of methane conversion are large-scale, energy- and cost-intensive operations; alternative small-scale, low-cost, direct procedures for methane-to-methanol conversion have thus become the subjects of a proliferating body of research.<sup>5,11</sup>

Interestingly, nature – as is its wont – has already resolved this problem to a level chemists can only aspire to: methane monooxygenase (MMO) proteins, found in methanotrophic bacteria, such as *Methylococcus capsulatus*, are able to readily convert methane to methanol with exceptional selectivity at ambient conditions.<sup>12</sup> MMO's use nicotinamide adenine dinucleotide (NADH) as a reducing agent in order to activate oxygen and, subsequently, partially oxidise methane to methanol on iron (soluble MMO) and copper (particulate MMO) active centres.<sup>13</sup>

The electrophilic metal-oxygen species adept of activating the C–H bond within methane are generated by these metal ions.<sup>14</sup> Accordingly, most configurations for the partial oxidation of methane have focussed on the formation and reactivity of iron– and copper–oxygen species, analogous to the ones found in biological systems.

The microporous structure of zeolites enables stabilisation of metal–oxygen complexes, akin to those found in MMOs, after ion-exchange and successive activation.<sup>15</sup> Numerous ion-exchanged zeolites (Fe, Co, Cu, Zn) have been subjected to investigation for their activity towards the methane-to-methanol conversion using various oxidants ( $O_2$ ,  $H_2O$ ,  $H_2O_2$ ,  $N_2O$ ). Cu-containing zeolites are the foremost candidates in the pursuit of an optimal procedure and industrial appropriation due to the formation of active sites occurring under oxygen activation and the desorption of methanol facilitated by water, eliminating the use of toxic chemicals.<sup>16,17</sup>

## 1.1 Zeolites

Zeolites are porous, crystalline aluminosilicates composed of  $SiO_4$  tetrahedra which can form a cornucopia of three-dimensional structures.<sup>18</sup> Formation of these structures involves the use of aluminosilicate hydrogel systems under hydrothermal conditions, with both the reactant and reaction-medium roles performed by water. Crystal growth is facilitated by the dissolution and transportation of materials from the polymerised aluminosilicate gel using alkaline aqueous solutions; consequently leading to supersaturation and

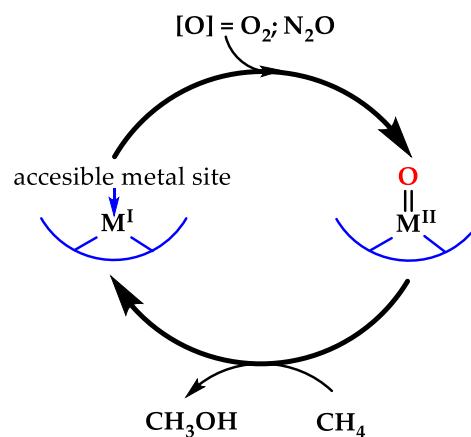


**Fig 1.1. Concept of methane activation over reactive metal-oxygen species.**

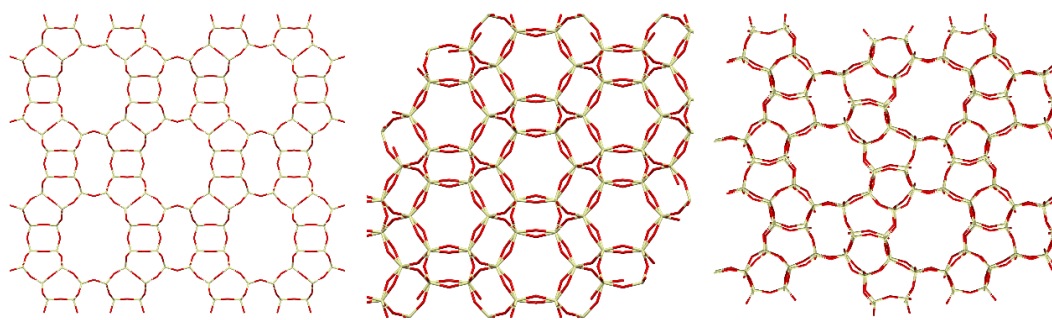


**Fig 1. 2. Framework structures of zeolites Mordenite, SSZ-13 and ZSM-5, respectively.**

nucleation of certain systematic zones.<sup>18,19</sup> Nucleation of the zeolite can be controlled since the resultant crystal size will depend on the number of nuclei available in the system; once the supply of nuclei is exhausted, growth terminates.<sup>20</sup> Factors critical to the zeolite formation include purity and mixing of the reactants; composition and crystallisation temperature of the gel; and the time afforded to age the precursor gel.<sup>21</sup> A variety of crystallisation temperatures have been reported, most commonly in the range of 80 – 180°C.<sup>22</sup> Time is a crucial and highly variable parameter. Not least to ensure procurement of a highly-crystalline material (with reports of crystallisation occurring over a few minutes or up to several weeks, depending on the type of zeolite); but to also prevent a phase-transformation of the product, as zeolites are metastable phases capable of transforming into more stable and denser crystals due to overexposure to the mother liquor.<sup>21</sup>

Zeolites' composition can be generalised as:  $(M^{n+})_{2/n} O : Al_2O_3 \cdot xSiO_2 : yH_2O$  where M and n denote a metal cation and its charge, respectively; whilst x and y are integers dependant on the type of zeolite. As per Löwenstein's rule, Al–O–Al linkages are forbidden, thus the framework Si/Al ratio must always be  $\geq 1$ .<sup>21</sup>

Indeed, natural zeolites have Si/Al ratios in the range of 1 – 4 and use alkali metal–water clusters as a template for synthesis. Synthetic zeolites can be enriched with silica to  $Si/Al = \infty$ ; an approach pioneered by Barrer and Denny, who introduced tetraalkylammonium ions into a zeolite structure.<sup>21,22</sup> Moreover, utilisation of organic templates extended the capability of zeolite modification by enabling transition metals to be introduced into the structure.<sup>23</sup> Zeolite framework type is determined by the symmetrically operated arrangement of polyhedral secondary building units (SBUs) of zeolites; pore size is greatly dependent on the number of tetrahedrally coordinated atoms (T-atoms, namely Si and Al) forming the membered ring (n-MR) channel. Hence, the categorisation of zeolites into: small-pore (8-MR,

diameter  $\sim 4\text{\AA}$ ); medium-pore (10-MR, diameter  $\sim 5.5\text{\AA}$ ); large-pore (12-MR, diameter  $\sim 7.5\text{\AA}$ ); and extra-large-pore ( $>14\text{-MR}$ , diameter  $> 8\text{\AA}$ ).<sup>21</sup>

Properties of zeolites are extensively modified by introducing charge-balancing cations. A negative charge is introduced into the framework via replacement of Si by Al; ergo the positive cations present in the channels compensate for this charge. Zeolites can also act as solid acids, after exchange of alkali cations with protons ( $\text{H}^+$ ) – a highly exploited property in the field of heterogenous catalysis. Modification of zeolites thus enables their application to be extended to various issues including ion capture (such as  $\text{NH}_4^+$ ) for environmental purposes or purification of water for its' diverse uses.<sup>21</sup>

The variability in geometry, connectivity and dimensionality of the pores, gives rise to extraordinary shape selectivity (differences below  $1\text{ \AA}$  can be distinguished) in zeolites.<sup>24</sup> Both the volume and the surface area (up to  $0.35\text{ cm}^3\text{ g}^{-1}$  and  $850\text{ m}^2\text{ g}^{-1}$ , respectively) are predetermined by this pore-system. Chemical composition affects several other characteristics including chemical and thermal stability; hydrophilic/hydrophobic interactions; and the distribution, number and strength of Brønsted and Lewis acid sites. Combining these properties of shape selectivity, dipolar interactions (between zeolite and guest-species), stability (both chemical and mechanical) and acid/base functionality, coupled with the environmentally friendly nature of the materials, renders zeolites exceptional heterogenous catalysts in both small- and large-scale processes.<sup>21,25,26</sup>

## 1.2 Partial Oxidation of Methane

For copper-zeolite systems, an oxidant must be used to activate the copper and thus create the active sites. Both the activation of the C–H bond in methane (at a relatively low  $450\text{ K}$ ) and stabilisation of the methoxy species thus derived are afforded by these active sites. Due to these properties, two regimes for converting methane to methanol have emerged: a stoichiometric – multi-step

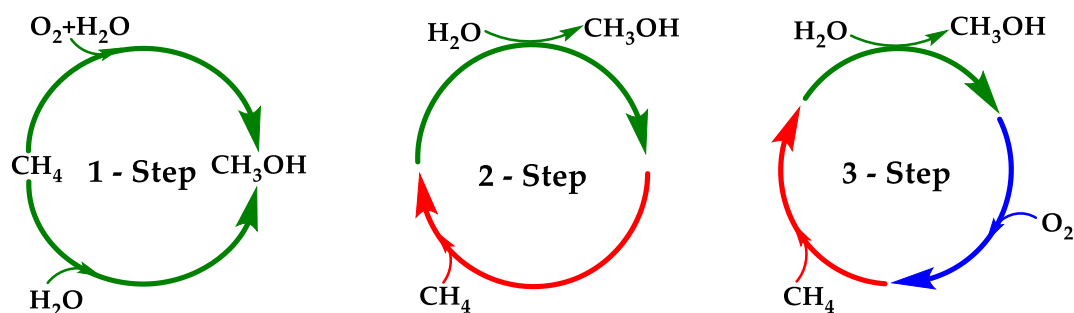


Fig. 1.3. Schemes for the partial oxidation of methane over Cu-zeolites.

– operation and a catalytic system incorporating continuous flow of oxidant.<sup>10,27</sup>

The primary scheme for the partial oxidation of methane is a stepwise process involving O<sub>2</sub> activation, CH<sub>4</sub> reaction and CH<sub>3</sub>OH extraction. Activation of the Cu-zeolite requires temperatures of ~450 °C under oxygen atmosphere followed by inert flow to remove any remnant O<sub>2</sub> (an oxygen free reaction atmosphere is believed to prevent over oxidation of methanol) after cooling. Methane is then introduced into the system at ~200 °C to initiate the reaction. Finally, methanol can be extracted from the zeolite framework through the hydrolysis of a Brønsted methoxy group bonded to a framework oxygen; or using water as a solvent to replace the methyl radical adsorbed to the framework oxygen, which releases methanol.<sup>10</sup> Spontaneous desorption of methanol from the zeolite pores is hard to achieve, however it is possible when using water or, theoretically, low water vapor as previously described by Kulkarni *et al.*<sup>28</sup> Permutations of this operation are also documented and include use of different oxidants (NO, H<sub>2</sub>O<sub>2</sub>)<sup>10</sup> and isothermal cycling.<sup>29</sup> Furthermore, an “anaerobic” approach has also been reported by Sushkevich *et al.*<sup>17</sup> whereby water was used as the source of oxygen for methane partial-oxidation over Cu-mordenite.

The continuous flow regime achieves direct methane partial oxidation using a mixture of water, oxygen and methane after an initial high-temperature activation. Using this procedure, methanol production rate of 1.8 μmol g<sup>-1</sup><sub>cat</sub> h<sup>-1</sup> was achieved; about half of the production rate compared to the three-step process.<sup>30</sup> Thus, although the catalytic system is able to selectively produce methanol, it is at the expense of the conversion rate – below 1% – which serves as an indication of the challenges in implementing such a system industrially.<sup>13,30</sup>

It is somewhat unsurprising, therefore, that within the gamut of methane partial oxidation strategies – especially in terms of active sites and reaction mechanisms – the focus has been on the multi-step, high-temperature, procedure; hence, the vast majority of information regarding copper-zeolites’ active sites and reaction mechanisms come from within this paradigm.

Copper-loaded zeolites with framework types CHA, MOR and MFI are currently the best performers in the stepwise methane-to-methanol conversion, in terms of methanol procured per mass of catalyst.<sup>27</sup> It’s important to note that zeolites’ performance is highly dependent on the reaction conditions: the former two frameworks have recently been outperformed by Cu-MAZ, in terms of methanol yield, however its stability over multiple reaction cycles is yet to be demonstrated.<sup>31,32</sup> Furthermore,

Zeolite Y, is relatively inactive for the methane-to-methanol conversion under the aerobic high-temperature regime, however the activity is appreciable under high pressure and isothermal conditions.<sup>33</sup> Likewise, FAU framework is inactive using a typical reaction temperature (473 K) of the multi-step operation, but at an increased reaction temperature (633 K) it has been shown to produce higher methanol yields than Cu-CHA or Cu-MOR.<sup>34</sup> These examples allude to the importance of framework in stabilising the active sites and affecting the activity thereof.

**Table 1.1. Summary of the best performing copper zeolites in the methane-to-methanol conversion.**

Copper Zeolite		Temperature (K)		Methanol yield
Framework	Cu (wt%)	Activation	Reaction	$\mu\text{mol g}_{\text{cat}}^{-1}$
MOR <sup>34</sup>	2.3	773	473	169
CHA <sup>35</sup>	3.9	773	473	125
MFI <sup>36</sup>	3.3	723	473	89
MAZ <sup>37</sup>	6.0	723	473	86
AFX <sup>38</sup>	5.0	723	473	39

Framework Si/Al ratio has been shown to affect the nature of the copper-oxo species formed: increasing aluminium content leading to higher-nuclearity copper-species with high activity under both aerobic and anaerobic activation; whereas monomeric species yield methanol after aerobic activation only.<sup>37</sup> This increase in activity and aluminium content, however, does not scale linearly; Vanelderen *et al.*<sup>38</sup> deduced that best performing materials had Si/Al ratios 12–30 indicating that an optimum number and distribution of aluminium in the framework propagates the active Cu-oxo species formation. Methanol procured per copper atom, on the other hand, does scale with increasing Si/Al ratio; several authors<sup>37,39–41</sup> have thus proposed that Si/Al ratios may correspond to the fractions of active/inactive copper species present.

The effects of framework on copper-zeolite systems' activity towards methane-to-methanol conversion clearly relate to the nature and quantity of the active species. However, it has also been shown that zeolitic-framework is not a necessity for the methane-to-methanol conversion: alumina<sup>42</sup> and silica<sup>43</sup> hosts have both been proven to be active for this conversion; alas, currently yielding considerably lower amounts of methanol than the Cu-zeolite materials.

### 1.3 Nature of the Active Sites

A topic of controversy in this investigation is the exact structure of the copper-oxo active species formed inside the zeolite framework. A variety of species have been proposed including monocopper;<sup>44,45</sup> dicopper (mono( $\mu$ -oxo)dicopper and bis( $\mu$ -oxo)dicopper);<sup>46-48</sup> tricopper (tris( $\mu$ -oxo)tricopper);<sup>49,50</sup> and CuO clusters.<sup>51</sup> Bis( $\mu$ -oxo)dicopper, ( $[\text{Cu}_2(\mu\text{O})]^{2+}$ ) sites were the first reported, primarily due to an observation of a signal at  $22,700\text{ cm}^{-1}$  using UV/Vis spectroscopy which was also documented in the biological study of metallo-enzymes.<sup>52,53</sup> Further investigations, combining Raman and UV/Vis spectroscopy, denoted mono( $\mu$ -oxo)dicopper as the active species.<sup>47</sup> Tricopper (tris( $\mu$ -oxo)tricopper,  $[\text{Cu}_3(\mu\text{O})_3]^{2+}$ ) has been proposed after DFT calculations on Cu-MOR indicated that a higher nuclearity renders them more stable than dicopper species;<sup>54</sup> with EXAFS analysis in agreement.<sup>49</sup> Indeed, DFT calculations carried out by Newton *et al.*<sup>27</sup> suggest that, theoretically at least, given the increase in stability with an increase in nuclearity, tetra- and pentamers are both viable and more stable than their di- or tri-copper counterparts. Both dimeric and trimeric sites have been proposed in metallo-enzymes; albeit, as is the case for copper-zeolites, no consensus about the active site exists.<sup>55-58</sup> Notwithstanding, other species have also been proposed: periodic DFT and thermodynamic analysis by Zhao *et al.*<sup>59</sup> concluded that monocopper ( $[\text{CuOH}]^+$ ) was responsible for the activity of Cu-SSZ13; and sub-nanometre CuO clusters<sup>48,51</sup> are also documented.

The variety of motifs proposed indicate an absence of a single universal active site but, rather, a coexistence of multiple structures within the same zeolitic host. This is well illustrated by the fact that methane-to-methanol conversion has been demonstrated in both high-temperature stepwise<sup>46</sup> and low-temperature isothermal regimes.<sup>29</sup> The latter, employing an activation temperature of 473 K (and not fully dehydrating the catalyst), renders the formation of “typical” copper-oxo species – which require an activation temperature of 553 K – improbable.<sup>33,51</sup> Despite the successful application of the isothermal regime, however, structures responsible for the low-temperature conversion of methane remain unquantized – which reiterates the

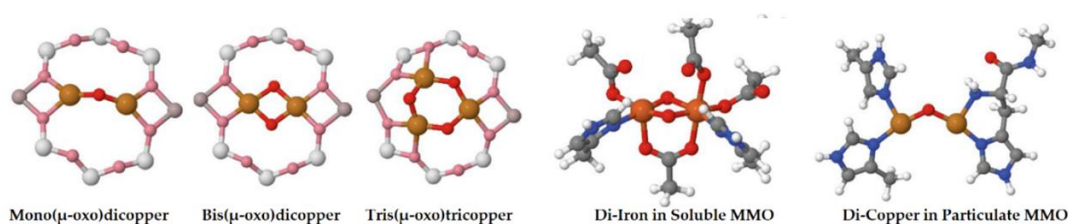


**Fig. 1.4. Some of the proposed active sites in Cu-zeolites and MMOs. Reproduced from Ref. 60.**

fact that the majority of attention has been focussed on the stoichiometric regime.<sup>27,60</sup>

It is paramount to ensure that assertions about the active sites derived from spectroscopic studies, such as UV/Vis and IR, should be coupled with complementary techniques to reinforce the findings, as deducing the nature of the active sites is a multi-faceted challenge and generalisations may not apply across systems, even where they may appear identical. For example, several bands have been assigned to a number of copper-oxo species using UV/Vis, but only the mono( $\mu$ -oxo)dicopper site has been confirmed by resonant Raman spectroscopy, DFT calculations and a number of other independent works; giving rise to the best descriptor of the active site to date.<sup>61–63</sup> Bands ascribed to isolated copper (II) cations and tricopper species at 12,000–14,000 and 31,000  $\text{cm}^{-1}$ , respectively, remain speculative.<sup>27</sup> Moreover, a number of motifs have been derived via the application of X-ray absorption spectroscopy: Grundner *et al.*<sup>49</sup> asserted the trimeric copper species to be the active site in CuMOR; whilst Pappas *et al.*<sup>39</sup> demonstrated an “unambiguous” determination of dimeric copper present within the same framework type. These examples illustrate that multiple sites are likely to coexist, and that multiple techniques must be combined in order to delineate the structures responsible for the conversion.

## **1.4 Number & Distribution of Active Sites**

Having discussed the nature of the active sites proposed thus far, it is important to address questions still unanswered: how many motifs are present?; how many are active for the partial oxidation of methane?; and what is their distribution?

Deka *et al.*<sup>64</sup> addressed some of these questions by combining in situ X-ray Diffraction (XRD) with EXAFS analysis enabling the identification of Cu(II) ions in the 6 membered rings (MR) of the chabazite (SSZ13) host under reaction conditions; alas, the authors could only account for 25% of the total copper in the sample. Subsequently, Andersen *et al.*<sup>65</sup> introduced the (computational) maximum entropy method and Ipek *et al.*<sup>66</sup> built on this by applying Raman spectroscopy. These combined efforts enabled all of the copper present to be accounted for: single Cu occupancy within the 6-MR and majority of the copper residing at two distinct sites within the 8-MR. Furthermore, these studies have also revealed that most of the copper in the sample was inactive, yielding only 0.03–0.05 methanol per copper atom. Electron paramagnetic resonance (EPR) has also been utilised to identify non-

active Cu(II) monomers in copper-loaded chabazite,<sup>35</sup> mordenite<sup>67</sup> and ZSM-5.<sup>68</sup> More recently, Godiksen *et al.*<sup>69</sup> used operando EPR and showcased the technique's discriminatory power: two spectroscopically distinct Cu(II) species were identified in the 6 MR rings of chabazite. Lercher *et al.*<sup>45</sup> have reported overcoming the issue of inactive copper formation by selectively modifying H-MOR with Cu; their efforts gave rise to uniform, trimeric copper species akin to enzymatic systems and enabled full utilisation of extra-framework complexes.

A different approach by Pappas *et al.*<sup>39</sup> employed a combination of high energy resolution fluorescence detection (HERFD) XANES and multivariate curve resolution (MCR) analysis (HERFD greatly enhances the energy resolution of XANES at the expense of detectible X-Ray flux) to extract information about the formation and interconversion of five discreet copper species under both oxygen and inert (He) activation. Anaerobic conditions were found to significantly promote Cu(I) formation through auto-reduction; whereas aerobic conditions yielded transiently observable auto-reduced Cu(I) at low temperatures only. Moreover, after correlating the fractions of active sites present – and their nuclearity – to the methanol produced, only one reactive site was deduced and found to comprise of two Cu atoms; the proposed species were: mono( $\mu$ -oxo)dicopper or *trans*-( $\mu$ -1,2, peroxo)dicopper.

To add to the complexity of the matter, it has also been demonstrated that mobilised copper ions are able to form dynamic, multinuclear sites by migrating through the zeolite windows to form ion pairs and participate in Cu(I)–Cu(II) redox reaction during the selective catalytic reduction of NO<sub>x</sub>.<sup>46</sup> Such mobilisation of copper ions and formation of mobile active sites has also been reported upon introduction of ammonia, which liberates the copper from the zeolitic framework.<sup>70</sup> Furthermore, highly stable dicopper dihydroxo species have been shown to form upon interaction with water;<sup>17</sup> indeed, as in the anaerobic<sup>71</sup> methane partial oxidation, water may also take part in the reaction mechanism. Furthermore, Vilella *et al.*<sup>72</sup> deduced that mono- and dicopper sites have similar binding energies towards the zeolitic lattice, illustrating yet another obstacle in differentiating the species.

Based on the vast evidence available, therefore, a multiplicity of copper centres is to be expected – only some of which are active towards methane partial oxidation – and variation in this multiplicity will differ depending on zeolite topology, environmental conditions and synthetic methods used.

## 1.5 Reaction Mechanism

The mechanism of C–H bond activation proceeds via one of four routes: electrophilic activation;  $\sigma$ -bond metathesis; oxidative addition; and oxidation with reactive species such as the copper active sites in zeolites.<sup>15</sup> During electrophilic activation, the C–H bonding orbital donates electrons into a vacant metal d orbital which polarises and weakens the C–H bond, enabling the deprotonation of methane. The  $\sigma$ -bond metathesis involves binding of methane to the M–X fragment which plays a similar role in activating the C–H bond. The oxidative addition pathway involves a low-valent metal reductively cleaving the C–H bond in methane by donating two electrons into the  $\sigma^*$  antibonding orbital. Lastly, the strategy employed by nature and metal-zeolites alike involves reactive metal-oxygen species which are highly electrophilic, and which contain low-lying unoccupied molecular orbitals localised on a metal-oxygen fragment; these behave as acceptor orbitals in the hydrogen abstraction from methane. A variety of copper species – some of which are active for methane-to-methanol conversion – have been proposed and observed. Although a consensus, in terms of the exact motif responsible for the reaction, has not been reached, there is a growing support in the scientific community that the reaction mechanism involves pairs or dimers of copper and proceeds via a two-electron process as a result of Cu(II) to Cu(I) reduction. The mechanism thus requires two Cu atoms for every CH<sub>3</sub>OH produced;<sup>40</sup> and the breaking of the C–H bond in methane is deemed the rate-limiting step in the reaction.<sup>47</sup> Sushkevich *et al.*<sup>17</sup> expanded on this during anaerobic partial-oxidation of methane where H<sub>2</sub><sup>18</sup>O was used to follow the reaction process using XAS. Combining their experimental findings and DFT calculations, the authors concluded that introducing water relaxes the system allowing surface methoxy and Brønsted acid sites to interact and produce Cu(I)–OH<sub>2</sub>–Cu(I) and methanol; adding that water subsequently re-oxidises Cu(I) to Cu(II) during methanol desorption, releasing hydrogen – a valuable product. The process was subsequently rendered thermodynamically and kinetically feasible after deducing the activation energy of 102 kJ mol<sup>-1</sup> which

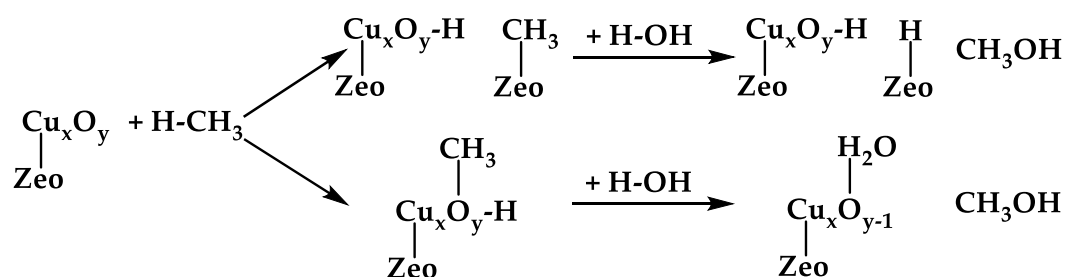


**Fig. 1.5.** Two proposed reaction pathways in the MTM conversion over Cu-Zeolites.

is comparable to the methane activation barrier. Furthermore, use of water in methane-to-methanol conversion over Cu-mordenite with high Si/Al ratio of 46 has been shown to produce Cu-monomers which are more selective in the aerobic regime than the dimers and trimers in low-Si/Al ratio mordenite; also ascribing such results to the stabilising effect of water.<sup>27</sup>

Another mechanism proposed for copper dimers and – primarily – trimers has been reported to operate over the Cu(III) and Cu(II) redox reaction. In this mechanism, Cu(I) has higher selectivity towards overoxidation products (CO, CO<sub>2</sub> and/or formates).<sup>73</sup> This route is a much more recent proposition, derived from theoretical studies, which suggests that Cu–O• oxyl radical complexes, which are a source of electrons required for the reaction, are formed at the active site.<sup>45</sup> Evidence compatible with this route was provided by Grundner *et al.*<sup>49</sup> who achieved high methanol selectivity and yield with comparably low amount of Cu(I); and Alayon *et al.*<sup>74</sup> who observed increased yield of Cu(I), high selectivity to complete oxidation products and, by extension, decreased methanol yields.

Despite both redox and oxyl-radical approaches having experimental and theoretical backing, the former is at the forefront due to a number of successful quantifications using X-ray absorption<sup>29,39,75</sup> correlating Cu(I) with methanol production. The mechanism involving oxyl-radicals, however, cannot be ruled out. This is not only due to the available evidence, but also because there is still relatively little known about all the possible mechanisms involved. This was recently demonstrated by Román-Leshkov *et al.*<sup>76</sup> who, after tandem oxidation and carbonylation, were able to produce acetic acid from methane. This transformation is the result of cooperative catalytic effects between (carbonylation-active) acid sites and (redox-active) copper centres. This phenomenon is important as the only acid sites active for carbonylation in mordenite are located within the 8-MR side-pockets; the implication is that of a previously unknown step in methanol migration between sites, similar to that observed in iron-based catalysts.<sup>77,78</sup> Thus, disparate proposals of active sites and reaction mechanisms should be considered complementary, not contradictory, as each endeavour – however small – adds valuable information about the nature and mechanics of these systems.

## 1.6 Reactivity & Yield

Continuing to improve synthetic catalysts requires an understanding of some key properties including the active site structure and environment; the optimisation of CH<sub>4</sub> oxidation functionality in the zeolite; and the required

reaction conditions. Various environments which stabilise reacting species across each step of the reaction pathway are afforded by diverse zeolite topologies such as different pore sizes and varying local confinement effects.<sup>13</sup> The structural environment found within Cu–MOR (8–MR) side pocket was found to be akin to that found within MMOs; consequently, it was suggested that this structure aids in stabilising the catalytically active trinuclear copper-oxo cluster.<sup>10,49</sup> Mahyuddin *et al.*<sup>54</sup> correlated an alteration in  $[\text{Cu}_2(\mu\text{-O})]^{2+}$ -zeolite species' electron acceptor orbital with the Cu–O–Cu bond angle which is set out by the zeolite topology and the crystallographic location of the active site; a subsequent decrease in the activation energy of a C–H bond cleavage was observed. Further correlation between  $\text{H}^+$  and  $-\text{OCH}_3$  moieties, upon C–H activation, was demonstrated by Sushkevich and co-workers;<sup>17</sup> and a mechanistic relevance of protons in methane partial oxidation was shown by Kalamaras *et al.*,<sup>79</sup> who reported a systematic increase in yields of methanol, ascertained as a function of increasing Brønsted acidity.

Recently, both Mordenite (MOR) and ZSM-5 (MFI) have been outperformed, in both reactivity and selectivity, by small-pore zeolites such as SSZ13 (CHA), SSZ19 (AFX), SSZ39 (AEI) and SAPO-34 (CHA).<sup>66,80–82</sup> Almost twice as much  $\text{CH}_3\text{OH}$  per copper atom was produced by the small pore zeolites compared to the medium (ZSM-5) and large (MOR) pore ones. These findings were supported by density functional theory (DFT) calculations which stipulated that  $[\text{Cu}_2(\mu\text{-O})_2]^{2+}$  formed within small-pore zeolites can perform the C–H bond dissociation at lower activation energies than those formed in medium- and large-pore zeolites.

A study of 12 different copper-exchanged zeolite structures (MOR, EON, MAZ, MEI, BPH, FAU, LTL, MFI, HEU, FER, SZR, and CHA) by Park *et al.*<sup>32</sup> compared the zeolite structures and their precursor type, activation temperatures under  $\text{O}_2$  flow, and methanol yield as a function of copper content. Cu–omega (MAZ) provided the highest methanol yield of  $86 \mu\text{mol g}_{\text{cat}}^{-1}$  — this result was explained by the densely distributed copper-oxo active species in the three-dimensional 8-MR channels, however its stability over multiple reaction cycles is yet to be demonstrated.

Despite the available evidence suggesting the coexistence of multiple active motifs within the zeolitic host, some dominant factors affecting methanol yields were documented by Dyballa *et al.*<sup>83</sup> These include high dispersion of copper-oxo active species; large amount of Cu exchanged in small-pore zeolites; adequately high activation temperature; and the use of the protonic zeolite precursor. Indeed, the authors reported that liquid-phase ion exchange of  $\text{H}^+$ -zeolite results in substantially higher methanol yields than the other cation precursors, and suggested the optimum stoichiometry between atoms

in Cu-MOR as: Si/Al = 7 and Cu/Al = 0.18, which reproducibly yields ~169  $\mu\text{mol g}_{\text{cat}}^{-1}$  methanol.

## 1.7 Project Aims

It is clear that the partial oxidation of methane over Cu-loaded zeolites is an incredibly active area of research, with continuous developments in our understanding of the challenges involved in bringing about an optimised process. Nonetheless, there remains a paucity of literature documenting the dynamics of various species involved in this reaction within the Cu-loaded zeolite catalysts. The primary aim of this project, therefore, is to investigate the dynamics of key species – methane, methanol, water and copper – within some of the foremost candidates in effecting this conversion; namely, Cu-loaded mordenite, SSZ-13 and ZSM-5 zeolites. By focussing on the behaviour of these species within the zeolites' framework, the project seeks to gain insights into how these dynamics may influence catalytic activity. This understanding is crucial for improving the efficacy of these materials in the methane-to-methanol conversion process.

Another important objective is the development and optimisation of reliable experimental methodologies to study the partial oxidation of methane over Cu-loaded zeolites. This includes the refinement of reactor setups and control systems in order to obtain accurate and reproducible data. Exploration of copper speciation within the different zeolitic frameworks is another key aspect of the investigation, aiming to delineate the impacts thereof on the catalytic activity of these materials. These include the study of the oxidation states of copper at different stages of the reaction, as well as exploring the phenomenon of Cu autoreduction. In addition, this project will seek to explore the role of water in the methane-to-methanol conversion, particularly its function as a soft oxidant and its impact on copper speciation and methanol production. Studying the structural integrity and adaptability of zeolites during the catalytic process is another important aspect of the project. Understanding how structural changes in the zeolite framework influence the activity and stability of the catalyst will be crucial for optimising its design.

The project also aims to utilise muon spin spectroscopy ( $\mu\text{SR}$ ) to investigate the dynamic behaviour of copper within the zeolitic frameworks. This novel approach aims to provide a unique perspective on the interactions between copper ions and the zeolite structure, offering insights into the mobility and

redox behaviour of the Cu species that are critical for these materials' catalytic performance.

Finally, the project seeks to integrate various multi-scale characterisation techniques, such as X-ray absorption, infrared spectroscopy and neutron scattering, to build an understanding of the relationship between zeolite structure, copper speciation and the catalytic activity. By combining these approaches, the research aims to provide a comprehensive view of the factors that influence catalytic performance, informing the design of more effective catalysts for methane-to-methanol conversion and potentially other reactions involving similar materials.

## 1.8 Bibliography

- (1) Achmad, F.; Kamarudin, S. K.; Daud, W. R. W.; Majlan, E. H. Passive Direct Methanol Fuel Cells for Portable Electronic Devices. *Appl Energy* 2011, 88 (5). <https://doi.org/10.1016/j.apenergy.2010.11.012>.
- (2) Zakaria, Z.; Kamarudin, S. K. Direct Conversion Technologies of Methane to Methanol: An Overview. *Renewable and Sustainable Energy Reviews* 2016, 65, 250–261. <https://doi.org/10.1016/J.RSER.2016.05.082>.
- (3) Yin, J.; Su, S.; Yu, X. X.; Weng, Y. Thermodynamic Characteristics of a Low Concentration Methane Catalytic Combustion Gas Turbine. *Appl Energy* 2010, 87 (6). <https://doi.org/10.1016/j.apenergy.2009.12.011>.
- (4) Reddy, P. V. L.; Kim, K. H.; Song, H. Emerging Green Chemical Technologies for the Conversion of CH<sub>4</sub> to Value Added Products. *Renewable and Sustainable Energy Reviews*. 2013. <https://doi.org/10.1016/j.rser.2013.03.035>.
- (5) Da Silva, M. J. Synthesis of Methanol from Methane: Challenges and Advances on the Multi-Step (Syngas) and One-Step Routes (DMTM). *Fuel Processing Technology*. 2016. <https://doi.org/10.1016/j.fuproc.2016.01.023>.
- (6) Jocz, J. N.; Medford, A. J.; Sievers, C. Thermodynamic Limitations of the Catalyst Design Space for Methanol Production from Methane. *ChemCatChem* 2019, 11 (1). <https://doi.org/10.1002/cctc.201801438>.
- (7) McFarland, E. Unconventional Chemistry for Unconventional Natural Gas. *Science*. 2012. <https://doi.org/10.1126/science.1226840>.

- (8) Ravi, M.; Ranocchiari, M.; van Bokhoven, J. A. The Direct Catalytic Oxidation of Methane to Methanol—A Critical Assessment. *Angewandte Chemie - International Edition*. 2017. <https://doi.org/10.1002/anie.201702550>.
- (9) Yarulina, I.; Chowdhury, A. D.; Meirer, F.; Weckhuysen, B. M.; Gascon, J. Recent Trends and Fundamental Insights in the Methanol-to-Hydrocarbons Process. *Nature Catalysis*. 2018. <https://doi.org/10.1038/s41929-018-0078-5>.
- (10) Park, M. B.; Park, E. D.; Ahn, W. S. Recent Progress in Direct Conversion of Methane to Methanol over Copper-Exchanged Zeolites. *Frontiers in Chemistry*. 2019. <https://doi.org/10.3389/fchem.2019.00514>.
- (11) Periana, R. A.; Taube, D. J.; Gamble, S.; Taube, H.; Satoh, T.; Fujii, H. Platinum Catalysts for the High-Yield Oxidation of Methane to a Methanol Derivative. *Science (1979)* 1998, 280 (5363). <https://doi.org/10.1126/science.280.5363.560>.
- (12) Colby, J.; Stirling, D. I.; Dalton, H. The Soluble Methane Mono Oxygenase of *Methylococcus Capsulatus* (Bath). Its Ability to Oxygenate n Alkanes, n Alkenes, Ethers, and Alicyclic, Aromatic and Heterocyclic Compounds. *Biochemical Journal* 1977, 165 (2). <https://doi.org/10.1042/bj1650395>.
- (13) Dinh, K. T.; Sullivan, M. M.; Serna, P.; Meyer, R. J.; Dincă, M.; Román-Leshkov, Y. Viewpoint on the Partial Oxidation of Methane to Methanol Using Cu- and Fe-Exchanged Zeolites. *ACS Catal* 2018, 8 (9). <https://doi.org/10.1021/acscatal.8b01180>.
- (14) Snyder, B. E. R.; Vanelderen, P.; Bols, M. L.; Hallaert, S. D.; Böttger, L. H.; Ungur, L.; Pierloot, K.; Schoonheydt, R. A.; Sels, B. F.; Solomon, E. I. The Active Site of Low-Temperature Methane Hydroxylation in Iron-Containing Zeolites. *Nature* 2016, 536 (7616). <https://doi.org/10.1038/nature19059>.
- (15) Snyder, B. E. R.; Bols, M. L.; Schoonheydt, R. A.; Sels, B. F.; Solomon, E. I. Iron and Copper Active Sites in Zeolites and Their Correlation to Metalloenzymes. *Chemical Reviews*. 2018. <https://doi.org/10.1021/acs.chemrev.7b00344>.
- (16) Lee, S. H.; Kang, J. K.; Park, E. D. Continuous Methanol Synthesis Directly from Methane and Steam over Cu(II)-Exchanged Mordenite. *Korean Journal of Chemical Engineering* 2018, 35 (11). <https://doi.org/10.1007/s11814-018-0150-5>.

- (17) Sushkevich, V. L.; Palagin, D.; Ranocchiari, M.; Van Bokhoven, J. A. Selective Anaerobic Oxidation of Methane Enables Direct Synthesis of Methanol. *Science* (1979) 2017, 356 (6337).  
<https://doi.org/10.1126/science.aam9035>.
- (18) Townsend, R. P. R. M. Barrer Hydrothermal Chemistry of Zeolites. London and New York (Academic Press). *Mineral Mag* 1983, 47 (344).  
<https://doi.org/10.1180/minmag.1983.047.344.29>.
- (19) D. W. Breck. Zeolite Molecular Sieves: Structure, Chemistry, and Use John Wiley and Sons, New York, London, Sydney, and Toronto. *J Chromatogr Sci* 1975, 13 (4), 18A-18A.  
<https://doi.org/10.1093/chromsci/13.4.18a-c>.
- (20) Tosheva, L.; Valtchev, V. P. Nanozeolites: Synthesis, Crystallization Mechanism, and Applications. *Chemistry of Materials*. 2005.  
<https://doi.org/10.1021/cm047908z>.
- (21) Blay V, Bobadilla L, C. G. A. *Zeolites and Metal-Organic Frameworks*; 2018. <https://doi.org/10.5117/9789462985568>.
- (22) Barrer, R. M.; Denny, P. J. 202. Hydrothermal Chemistry of the Silicates. Part X. A Partial Study of the Field CaO-Al<sub>2</sub>O<sub>3</sub>-SiO<sub>2</sub>-H<sub>2</sub>O. *Journal of the Chemical Society* 1961.  
<https://doi.org/10.1039/JR9610000983>.
- (23) Bellussi, G.; Carati, A.; Clerici, M. G.; Esposito, A. Double Substitution in Silicalite by Direct Synthesis: A New Route to Crystalline Porous Bifunctional Catalysts. *Stud Surf Sci Catal* 1991, 63 (C).  
[https://doi.org/10.1016/S0167-2991\(08\)64604-2](https://doi.org/10.1016/S0167-2991(08)64604-2).
- (24) Stewart, A. An Introduction to Zeolite Molecular Sieves by Alan Dyer. Wiley, Chichester, 1988. ISBN 0471 91981 0. *Surface and Interface Analysis* 1989, 14 (4). <https://doi.org/10.1002/sia.740140410>.
- (25) Fajula, F.; Galarneau, A.; Renzo, F. Di. Advanced Porous Materials: New Developments and Emerging Trends. In *Microporous and Mesoporous Materials*; 2005; Vol. 82.  
<https://doi.org/10.1016/j.micromeso.2005.01.036>.
- (26) Sherman, J. D. Synthetic Zeolites and Other Microporous Oxide Molecular Sieves. *Proc Natl Acad Sci U S A* 1999, 96 (7).  
<https://doi.org/10.1073/pnas.96.7.3471>.
- (27) Newton, M. A.; Knorpp, A. J.; Sushkevich, V. L.; Palagin, D.; Van Bokhoven, J. A. Active Sites and Mechanisms in the Direct Conversion of Methane to Methanol Using Cu in Zeolitic Hosts: A Critical

Examination. *Chemical Society Reviews*. 2020.

<https://doi.org/10.1039/c7cs00709d>.

- (28) Kulkarni, A. R.; Zhao, Z. J.; Siahrostami, S.; Nørskov, J. K.; Studt, F. Cation-Exchanged Zeolites for the Selective Oxidation of Methane to Methanol. *Catalysis Science and Technology*. 2018. <https://doi.org/10.1039/c7cy01229b>.
- (29) Knorpp, A. J.; Newton, M. A.; Mizuno, S. C. M.; Zhu, J.; Mebrate, H.; Pinar, A. B.; Van Bokhoven, J. A. Comparative Performance of Cu-Zeolites in the Isothermal Conversion of Methane to Methanol. *Chemical Communications* 2019, 55 (78). <https://doi.org/10.1039/c9cc05659a>.
- (30) Narsimhan, K.; Iyoki, K.; Dinh, K.; Román-Leshkov, Y. Catalytic Oxidation of Methane into Methanol over Copper-Exchanged Zeolites with Oxygen at Low Temperature. *ACS Cent Sci* 2016, 2 (6). <https://doi.org/10.1021/acscentsci.6b00139>.
- (31) Knorpp, A. J.; Pinar, A. B.; Newton, M. A.; Sushkevich, V. L.; van Bokhoven, J. A. Copper-Exchanged Omega (MAZ) Zeolite: Copper-Concentration Dependent Active Sites and Its Unprecedented Methane to Methanol Conversion. *ChemCatChem* 2018, 10 (24). <https://doi.org/10.1002/cctc.201801809>.
- (32) Park, M. B.; Ahn, S. H.; Mansouri, A.; Ranocchiari, M.; van Bokhoven, J. A. Comparative Study of Diverse Copper Zeolites for the Conversion of Methane into Methanol. *ChemCatChem* 2017, 9 (19). <https://doi.org/10.1002/cctc.201700768>.
- (33) Tomkins, P.; Mansouri, A.; Bozbag, S. E.; Krumeich, F.; Park, M. B.; Alayon, E. M. C.; Ranocchiari, M.; Vanbokhoven, J. A. Isothermal Cyclic Conversion of Methane into Methanol over Copper-Exchanged Zeolite at Low Temperature. *Angewandte Chemie - International Edition* 2016, 55 (18). <https://doi.org/10.1002/anie.201511065>.
- (34) Pappas, D. K.; Martini, A.; Dyballa, M.; Kvande, K.; Teketel, S.; Lomachenko, K. A.; Baran, R.; Glatzel, P.; Arstad, B.; Berlier, G.; Lamberti, C.; Bordiga, S.; Olsbye, U.; Svelle, S.; Beato, P.; Borfecchia, E. The Nuclearity of the Active Site for Methane to Methanol Conversion in Cu-Mordenite: A Quantitative Assessment. *J Am Chem Soc* 2018, 140 (45). <https://doi.org/10.1021/jacs.8b08071>.
- (35) Pappas, D. K.; Borfecchia, E.; Dyballa, M.; Pankin, I. A.; Lomachenko, K. A.; Martini, A.; Signorile, M.; Teketel, S.; Arstad, B.; Berlier, G.; Lamberti, C.; Bordiga, S.; Olsbye, U.; Lillerud, K. P.; Svelle, S.; Beato, P.

- Methane to Methanol: Structure-Activity Relationships for Cu-CHA. *J Am Chem Soc* 2017, 139 (42). <https://doi.org/10.1021/jacs.7b06472>.
- (36) Markovits, M. A. C.; Jentys, A.; Tromp, M.; Sanchez-Sanchez, M.; Lercher, J. A. Effect of Location and Distribution of Al Sites in ZSM-5 on the Formation of Cu-Oxo Clusters Active for Direct Conversion of Methane to Methanol. *Top Catal* 2016, 59 (17–18). <https://doi.org/10.1007/s11244-016-0676-x>.
- (37) Park, M. B.; Ahn, S. H.; Mansouri, A.; Ranocchiari, M.; van Bokhoven, J. A. Comparative Study of Diverse Copper Zeolites for the Conversion of Methane into Methanol. *ChemCatChem* 2017, 9 (19). <https://doi.org/10.1002/cctc.201700768>.
- (38) Wulfers, M. J.; Teketel, S.; Ipek, B.; Lobo, R. F. Conversion of Methane to Methanol on Copper-Containing Small-Pore Zeolites and Zeotypes. *Chemical Communications* 2015, 51 (21). <https://doi.org/10.1039/c4cc09645b>.
- (39) Sushkevich, V. L.; Van Bokhoven, J. A. Methane-to-Methanol: Activity Descriptors in Copper-Exchanged Zeolites for the Rational Design of Materials. *ACS Catal* 2019, 9 (7). <https://doi.org/10.1021/acscatal.9b01534>.
- (40) Sushkevich, V. L.; Van Bokhoven, J. A. Effect of Brønsted Acid Sites on the Direct Conversion of Methane into Methanol over Copper-Exchanged Mordenite. *Catal Sci Technol* 2018, 8 (16). <https://doi.org/10.1039/c8cy01055b>.
- (41) Vanelderen, P.; Hadt, R. G.; Smeets, P. J.; Solomon, E. I.; Schoonheydt, R. A.; Sels, B. F. Cu-ZSM-5: A Biomimetic Inorganic Model for Methane Oxidation. *J Catal* 2011, 284 (2). <https://doi.org/10.1016/j.jcat.2011.10.009>.
- (42) Pappas, D. K.; Martini, A.; Dyballa, M.; Kvande, K.; Teketel, S.; Lomachenko, K. A.; Baran, R.; Glatzel, P.; Arstad, B.; Berlier, G.; Lamberti, C.; Bordiga, S.; Olsbye, U.; Svelle, S.; Beato, P.; Borfecchia, E. The Nuclearity of the Active Site for Methane to Methanol Conversion in Cu-Mordenite: A Quantitative Assessment. *J Am Chem Soc* 2018, 140 (45). <https://doi.org/10.1021/jacs.8b08071>.
- (43) Newton, M. A.; Knorpp, A. J.; Pinar, A. B.; Sushkevich, V. L.; Palagin, D.; Van Bokhoven, J. A. On the Mechanism Underlying the Direct Conversion of Methane to Methanol by Copper Hosted in Zeolites; Braiding Cu K-Edge XANES and Reactivity Studies. *J Am Chem Soc* 2018, 140 (32). <https://doi.org/10.1021/jacs.8b05139>.

- (44) Sushkevich, V. L.; Palagin, D.; van Bokhoven, J. A. The Effect of the Active-Site Structure on the Activity of Copper Mordenite in the Aerobic and Anaerobic Conversion of Methane into Methanol. *Angewandte Chemie - International Edition* 2018, 57 (29). <https://doi.org/10.1002/anie.201802922>.
- (45) Meyet, J.; Searles, K.; Newton, M. A.; Wörle, M.; van Bavel, A. P.; Horton, A. D.; van Bokhoven, J. A.; Copéret, C. Monomeric Copper(II) Sites Supported on Alumina Selectively Convert Methane to Methanol. *Angewandte Chemie - International Edition* 2019, 58 (29). <https://doi.org/10.1002/anie.201903802>.
- (46) Bozbag, S. E.; Sot, P.; Nachtegaal, M.; Ranocchiari, M.; Van Bokhoven, J. A.; Mesters, C. Direct Stepwise Oxidation of Methane to Methanol over Cu-SiO<sub>2</sub>. *ACS Catal* 2018, 8 (7). <https://doi.org/10.1021/acscatal.8b01021>.
- (47) Grundner, S.; Luo, W.; Sanchez-Sanchez, M.; Lercher, J. A. Synthesis of Single-Site Copper Catalysts for Methane Partial Oxidation. *Chemical Communications* 2016, 52 (12). <https://doi.org/10.1039/c5cc08371k>.
- (48) Li, G.; Vassilev, P.; Sanchez-Sanchez, M.; Lercher, J. A.; Hensen, E. J. M.; Pidko, E. A. Stability and Reactivity of Copper Oxo-Clusters in ZSM-5 Zeolite for Selective Methane Oxidation to Methanol. *J Catal* 2016, 338. <https://doi.org/10.1016/j.jcat.2016.03.014>.
- (49) Groothaert, M. H.; Smeets, P. J.; Sels, B. F.; Jacobs, P. A.; Schoonheydt, R. A. Selective Oxidation of Methane by the Bis( $\mu$ -Oxo)Dicopper Core Stabilized on ZSM-5 and Mordenite Zeolites. *J Am Chem Soc* 2005, 127 (5). <https://doi.org/10.1021/ja047158u>.
- (50) Woertink, J. S.; Smeets, P. J.; Groothaert, M. H.; Vance, M. A.; Sels, B. F.; Schoonheydt, R. A.; Solomon, E. I. A [Cu<sub>2</sub>O]<sub>2</sub><sup>+</sup> Core in Cu-ZSM-5, the Active Site in the Oxidation of Methane to Methanol. *Proc Natl Acad Sci U S A* 2009, 106 (45). <https://doi.org/10.1073/pnas.0910461106>.
- (51) Tsai, M. L.; Hadt, R. G.; Vanelderen, P.; Sels, B. F.; Schoonheydt, R. A.; Solomon, E. I. 2+ Active Site Formation in Cu-ZSM-5: Geometric and Electronic Structure Requirements for N<sub>2</sub>O Activation. *J Am Chem Soc* 2014, 136 (9). <https://doi.org/10.1021/ja4113808>.
- (52) Grundner, S.; Markovits, M. A. C.; Li, G.; Tromp, M.; Pidko, E. A.; Hensen, E. J. M.; Jentys, A.; Sanchez-Sanchez, M.; Lercher, J. A. Single-Site Trinuclear Copper Oxygen Clusters in Mordenite for Selective Conversion of Methane to Methanol. *Nat Commun* 2015, 6. <https://doi.org/10.1038/ncomms8546>.

- (53) Markovits, M. A. C.; Jentys, A.; Tromp, M.; Sanchez-Sanchez, M.; Lercher, J. A. Effect of Location and Distribution of Al Sites in ZSM-5 on the Formation of Cu-Oxo Clusters Active for Direct Conversion of Methane to Methanol. *Top Catal* 2016, 59 (17–18). <https://doi.org/10.1007/s11244-016-0676-x>.
- (54) Tomkins, P.; Ranocchiari, M.; Van Bokhoven, J. A. Direct Conversion of Methane to Methanol under Mild Conditions over Cu-Zeolites and Beyond. *Acc Chem Res* 2017, 50 (2). <https://doi.org/10.1021/acs.accounts.6b00534>.
- (55) Solomon, E. I.; Heppner, D. E.; Johnston, E. M.; Ginsbach, J. W.; Cirera, J.; Qayyum, M.; Kieber-Emmons, M. T.; Kjaergaard, C. H.; Hadt, R. G.; Tian, L. Copper Active Sites in Biology. *Chemical Reviews*. 2014. <https://doi.org/10.1021/cr400327t>.
- (56) Fujisawa, K.; Tanaka, M.; Moro-oka, Y.; Kitajima, N. A Monomeric Side-On Superoxocopper(II) Complex: Cu(O<sub>2</sub>)(HB(3-TBu-5-IPr)<sub>3</sub>). *J Am Chem Soc* 1994, 116 (26). <https://doi.org/10.1021/ja00105a069>.
- (57) Mahyuddin, M. H.; Tanaka, T.; Shiota, Y.; Staykov, A.; Yoshizawa, K. Methane Partial Oxidation over [Cu<sub>2</sub>(μ-O)]<sup>2+</sup> and [Cu<sub>3</sub>(μ-O)<sub>3</sub>]<sup>2+</sup> Active Species in Large-Pore Zeolites. *ACS Catal* 2018, 8 (2). <https://doi.org/10.1021/acscatal.7b03389>.
- (58) Ross, M. O.; MacMillan, F.; Wang, J.; Nisthal, A.; Lawton, T. J.; Olafson, B. D.; Mayo, S. L.; Rosenzweig, A. C.; Hoffman, B. M. Particulate Methane Monooxygenase Contains Only Mononuclear Copper Centers. *Science (1979)* 2019, 364 (6440). <https://doi.org/10.1126/science.aav2572>.
- (59) Balasubramanian, R.; Smith, S. M.; Rawat, S.; Yatsunyk, L. A.; Stemmler, T. L.; Rosenzweig, A. C. Oxidation of Methane by a Biological Dicopper Centre. *Nature* 2010, 465 (7294). <https://doi.org/10.1038/nature08992>.
- (60) Ross, M. O.; Rosenzweig, A. C. A Tale of Two Methane Monooxygenases. *Journal of Biological Inorganic Chemistry*. 2017. <https://doi.org/10.1007/s00775-016-1419-y>.
- (61) Chan, S. I.; Wang, V. C. C.; Lai, J. C. H.; Yu, S. S. F.; Chen, P. P. Y.; Chen, K. H. C.; Chen, C. L.; Chan, M. K. Redox Potentiometry Studies of Particulate Methane Monooxygenase: Support for a Trinuclear Copper Cluster Active Site. *Angewandte Chemie - International Edition* 2007, 46 (12). <https://doi.org/10.1002/anie.200604647>.

- (62) Zhao, Z. J.; Kulkarni, A.; Vilella, L.; Nørskov, J. K.; Studt, F. Theoretical Insights into the Selective Oxidation of Methane to Methanol in Copper-Exchanged Mordenite. *ACS Catal* 2016, 6 (6). <https://doi.org/10.1021/acscatal.6b00440>.
- (63) Ravi, M.; Sushkevich, V. L.; Knorpp, A. J.; Newton, M. A.; Palagin, D.; Pinar, A. B.; Ranocchiari, M.; van Bokhoven, J. A. Misconceptions and Challenges in Methane-to-Methanol over Transition-Metal-Exchanged Zeolites. *Nature Catalysis*. 2019. <https://doi.org/10.1038/s41929-019-0273-z>.
- (64) Vanelderen, P.; Snyder, B. E. R.; Tsai, M. L.; Hadt, R. G.; Vancauwenbergh, J.; Coussens, O.; Schoonheydt, R. A.; Sels, B. F.; Solomon, E. I. Spectroscopic Definition of the Copper Active Sites in Mordenite: Selective Methane Oxidation. *J Am Chem Soc* 2015, 137 (19). <https://doi.org/10.1021/jacs.5b02817>.
- (65) Smeets, P. J.; Woertink, J. S.; Sels, B. F.; Solomon, E. I.; Schoonheydt, R. A. Transition-Metal Ions in Zeolites: Coordination and Activation of Oxygen. *Inorg Chem* 2010, 49 (8). <https://doi.org/10.1021/ic901814f>.
- (66) Kim, Y.; Kim, T. Y.; Lee, H.; Yi, J. Distinct Activation of Cu-MOR for Direct Oxidation of Methane to Methanol. *Chemical Communications* 2017, 53 (29). <https://doi.org/10.1039/c7cc00467b>.
- (67) Deka, U.; Juhin, A.; Eilertsen, E. A.; Emerich, H.; Green, M. A.; Korhonen, S. T.; Weckhuysen, B. M.; Beale, A. M. Confirmation of Isolated Cu<sup>2+</sup> Ions in SSZ-13 Zeolite as Active Sites in NH<sub>3</sub>-Selective Catalytic Reduction. *Journal of Physical Chemistry C* 2012, 116 (7). <https://doi.org/10.1021/jp212450d>.
- (68) Andersen, C. W.; Bremholm, M.; Vennestrøm, P. N. R.; Blichfeld, A. B.; Lundegaard, L. F.; Iversen, B. B. Location of Cu<sup>2+</sup> in CHA Zeolite Investigated by X-Ray Diffraction Using the Rietveld/Maximum Entropy Method. *IUCrJ* 2014, 1. <https://doi.org/10.1107/S2052252514020181>.
- (69) Ipek, B.; Wulfers, M. J.; Kim, H.; Göttl, F.; Hermans, I.; Smith, J. P.; Booksh, K. S.; Brown, C. M.; Lobo, R. F. Formation of [Cu<sub>2</sub>O<sub>2</sub>]<sup>2+</sup> and [Cu<sub>2</sub>O]<sup>2+</sup> toward C-H Bond Activation in Cu-SSZ-13 and Cu-SSZ-39. *ACS Catal* 2017, 7 (7). <https://doi.org/10.1021/acscatal.6b03005>.
- (70) Godiksen, A.; Stappen, F. N.; Vennestrøm, P. N. R.; Giordanino, F.; Rasmussen, S. B.; Lundegaard, L. F.; Mossin, S. Coordination Environment of Copper Sites in Cu-CHA Zeolite Investigated by

- Electron Paramagnetic Resonance. *Journal of Physical Chemistry C* 2014, 118 (40). <https://doi.org/10.1021/jp5065616>.
- (71) Vanelderen, P.; Vancauwenbergh, J.; Tsai, M. L.; Hadt, R. G.; Solomon, E. I.; Schoonheydt, R. A.; Sels, B. F. Spectroscopy and Redox Chemistry of Copper in Mordenite. *ChemPhysChem* 2014, 15 (1). <https://doi.org/10.1002/cphc.201300730>.
- (72) Groothaert, M. H.; Pierloot, K.; Delabie, A.; Schoonheydt, R. A. Identification of Cu(II) Coordination Structures in Cu-ZSM-5, Based on a DFT/Ab Initio Assignment of the EPR Spectra. *Physical Chemistry Chemical Physics* 2003, 5 (10). <https://doi.org/10.1039/b301120h>.
- (73) Godiksen, A.; Isaksen, O. L.; Rasmussen, S. B.; Vennestrøm, P. N. R.; Mossin, S. Site-Specific Reactivity of Copper Chabazite Zeolites with Nitric Oxide, Ammonia, and Oxygen. *ChemCatChem* 2018, 10 (2). <https://doi.org/10.1002/cctc.201701357>.
- (74) Paolucci, C.; Parekh, A. A.; Khurana, I.; Di Iorio, J. R.; Li, H.; Albarracin Caballero, J. D.; Shih, A. J.; Anggara, T.; Delgass, W. N.; Miller, J. T.; Ribeiro, F. H.; Gounder, R.; Schneider, W. F. Catalysis in a Cage: Condition-Dependent Speciation and Dynamics of Exchanged Cu Cations in Ssz-13 Zeolites. *J Am Chem Soc* 2016, 138 (18). <https://doi.org/10.1021/jacs.6b02651>.
- (75) Palagin, D.; Sushkevich, V. L.; Van Bokhoven, J. A. Water Molecules Facilitate Hydrogen Release in Anaerobic Oxidation of Methane to Methanol over Cu/Mordenite. *ACS Catal* 2019, 9 (11). <https://doi.org/10.1021/acscatal.9b02702>.
- (76) Vilella, L.; Studt, F. The Stability of Copper Oxo Species in Zeolite Frameworks. *Eur J Inorg Chem* 2016, 2016 (10). <https://doi.org/10.1002/ejic.201501270>.
- (77) Chan, S. I.; Yu, S. S. F. Controlled Oxidation of Hydrocarbons by the Membrane-Bound Methane Monooxygenase: The Case for a Tricopper Cluster. *Acc Chem Res* 2008, 41 (8). <https://doi.org/10.1021/ar700277n>.
- (78) Mae Alayon, E.; Nachtegaal, M.; Ranocchiari, M.; Van Bokhoven, J. A. Catalytic Conversion of Methane to Methanol over Cu-Mordenite. *Chemical Communications* 2012, 48 (3). <https://doi.org/10.1039/c1cc15840f>.
- (79) Knorpp, A. J.; Newton, M. A.; Pinar, A. B.; Van Bokhoven, J. A. Conversion of Methane to Methanol on Copper Mordenite: Redox Mechanism of Isothermal and High-Temperature-Activation

- Procedures. *Ind Eng Chem Res* 2018, 57 (36).  
<https://doi.org/10.1021/acs.iecr.8b01183>.
- (80) Narsimhan, K.; Michaelis, V. K.; Mathies, G.; Gunther, W. R.; Griffin, R. G.; Román-Leshkov, Y. Methane to Acetic Acid over Cu-Exchanged Zeolites: Mechanistic Insights from a Site-Specific Carbonylation Reaction. *J Am Chem Soc* 2015, 137 (5).  
<https://doi.org/10.1021/ja5106927>.
- (81) Starokon, E. V.; Parfenov, M. V.; Arzumanov, S. S.; Pirutko, L. V.; Stepanov, A. G.; Panov, G. I. Oxidation of Methane to Methanol on the Surface of FeZSM-5 Zeolite. *J Catal* 2013, 300.  
<https://doi.org/10.1016/j.jcat.2012.12.030>.
- (82) Parfenov, M. V.; Starokon, E. V.; Pirutko, L. V.; Panov, G. I. Quasicatalytic and Catalytic Oxidation of Methane to Methanol by Nitrous Oxide over FeZSM-5 Zeolite. *J Catal* 2014, 318.  
<https://doi.org/10.1016/j.jcat.2014.07.009>.
- (83) Kalamaras, C.; Palomas, D.; Bos, R.; Horton, A.; Crimmin, M.; Hellgardt, K. Selective Oxidation of Methane to Methanol over Cu- And Fe-Exchanged Zeolites: The Effect of Si/Al Molar Ratio. *Catal Letters* 2016, 146 (2). <https://doi.org/10.1007/s10562-015-1664-7>.
- (84) Pappas, D. K.; Borfecchia, E.; Dyballa, M.; Pankin, I. A.; Lomachenko, K. A.; Martini, A.; Signorile, M.; Teketel, S.; Arstad, B.; Berlier, G.; Lamberti, C.; Bordiga, S.; Olsbye, U.; Lillerud, K. P.; Svelle, S.; Beato, P. Methane to Methanol: Structure-Activity Relationships for Cu-CHA. *J Am Chem Soc* 2017, 139 (42). <https://doi.org/10.1021/jacs.7b06472>.
- (85) Wulfers, M. J.; Teketel, S.; Ipek, B.; Lobo, R. F. Conversion of Methane to Methanol on Copper-Containing Small-Pore Zeolites and Zeotypes. *Chemical Communications* 2015, 51 (21).  
<https://doi.org/10.1039/c4cc09645b>.
- (86) Oord, R.; Schmidt, J. E.; Weckhuysen, B. M. Methane-to-Methanol Conversion over Zeolite Cu-SSZ-13, and Its Comparison with the Selective Catalytic Reduction of NO<sub>x</sub> with NH<sub>3</sub>. *Catal Sci Technol* 2018, 8 (4). <https://doi.org/10.1039/c7cy02461d>.
- (87) Dyballa, M.; Pappas, D. K.; Kvande, K.; Borfecchia, E.; Arstad, B.; Beato, P.; Olsbye, U.; Svelle, S. On How Copper Mordenite Properties Govern the Framework Stability and Activity in the Methane-to-Methanol Conversion. *ACS Catal* 2019, 9 (1).  
<https://doi.org/10.1021/acscatal.8b04437>.

# Chapter 2

---

## Methodology

In the realm of physical science, the characterisation of materials has paved the way for remarkable advancements in our understanding of their structural, electronic and magnetic properties. Spectroscopy with neutrons and muons, in particular, has emerged as an indispensable tool in this pursuit, offering unparalleled insights into the dynamic behaviour of various materials. This chapter describes the fundamentals of neutron and muon spectroscopy, delineating their underlying principles and experimental methodologies, followed by a description of various other techniques employed during the course of this project that have aided in the pursuit to better understand the interactions between species involved in the partial oxidation of methane and the catalysts propagating this reaction.

### 2.1 Neutron Scattering<sup>1,2</sup>

The neutron ( ${}^1_0n$ ), discovered by J. Chadwick (1932) after bombarding beryllium with  $\alpha$ -particles (He nuclei), is a stable elementary particle (a hadron) when bound in atomic nuclei; free neutrons are unstable and undergo  $\beta$ -decay with a mean lifetime of ca. 15 minutes. Neutrons have a rest mass close to that of a proton ( $1.6749 \times 10^{-27}$  kg); a magnetic moment (spin  $\frac{1}{2}$ ); and zero charge. These latter two properties mean that neutron-matter interactions are magnetic or nuclear (via the strong nuclear force), as opposed to electromagnetic (X-rays) or electrostatic (electrons). Nuclear force, although inherently powerful, only acts over short distances, yielding weak scattering from atoms and consequently requiring large sample sizes to improve the signal. The advantage, however, is that neutrons offer deep penetration (e.g., centimetres of Al) enabling the probing of bulk-properties of a given material. If a material under study contains unpaired orbital electrons, the incident neutrons can be scattered via spin-based dipole-dipole interaction which occurs at a similar rate to nuclear scattering, making it the predominant technique for the study of magnetism; albeit with the advent of new synchrotron sources, X-rays have become a viable alternative.

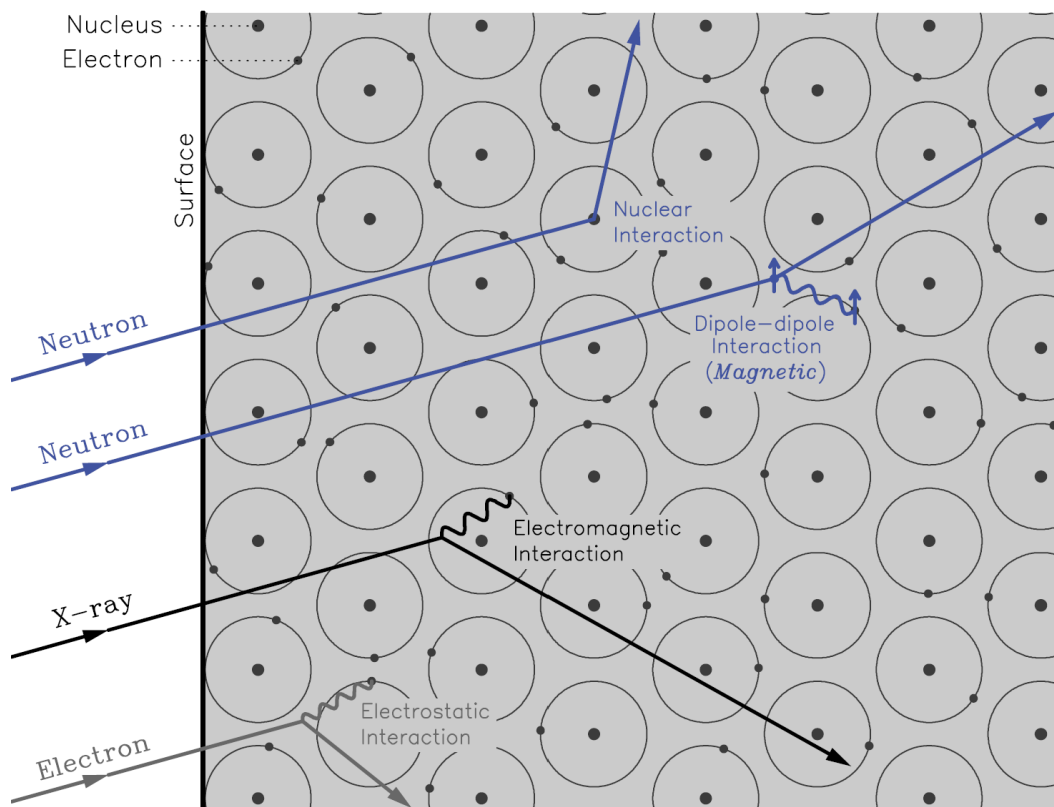


**Fig. 2.1.1. Schematic representation of the principal interactions between condensed matter and electrons, neutrons and X-rays. (Reproduced from Ref. 3)**

As with other elementary particles, neutrons display a wave-particle duality. That is, whether it is treated as a particle or a wave is entirely dependent on the phenomena that is under observation. In incoherent-inelastic neutron scattering experiments, for example, the neutron is treated as a particle (the scattered neutrons are subsequently treated as theoretical spherical waves). The propagation and spreading of neutrons is determined via diffraction and interference, which give rise to the neutrons' wave-like properties. As such, thermalised neutrons have a de Broglie wavelength of ca. 1–5 Å and energy of 0.025 eV, which are comparable to intermolecular distances and molecular vibrations, respectively. Thus, neutron scattering can reveal both structural and dynamic properties of the material under investigation.

Important to note are some distinctions between the types of scattering events that may occur during an experiment. When a neutron is scattered, there is a certain probability that the scattering event will result in no energy exchange, giving rise to *elastic* scattering. Furthermore, waves scattered from the same type of nuclei may interfere and give rise to *coherent elastic* scattering, such as that utilised in diffraction experiments, enabling the elucidation of relative positions of atoms within a material. Conversely, materials which contain

isotopic and/or spin heterogeneity may reduce the interference of the scattered waves, sometimes entirely, giving rise to *incoherent* scattering. A scattering event may also involve an energy exchange between the neutron and the scattering atom, giving rise to inelastic neutron scattering (INS). This type of *inelastic* scattering from *incoherent* systems forms the basis of vibrational spectroscopy with neutrons, as well as quasielastic neutron scattering (QENS), and is one of the main themes of this thesis. As such, it is important to highlight the advantages of both INS and QENS with respect to the well-established optical techniques:

- Unlike photons, neutrons are inherently deeply-penetrating and readily pass through the sample vessel (usually aluminium or steel) walls into the sample. This renders neutrons an ideal tool for the study of bulk properties and processes occurring within, rather than on the surface of, a material.
- The mass of the neutron (ca. 1 unified atomic mass unit) enables both energy and momentum transfer during a scattering event, and consequently the measurement is not limited to the Brillouin zone centre – hence all vibrations are active and, by and large, measurable. In other words, the spectra are not subject to optical selection rules as in, for example, IR or Raman spectroscopy; and the spectral intensities are directly proportional to elemental concentrations within the sample.
- Neutrons cover a vast energy range ( $16\text{--}4000\text{ cm}^{-1}$ ) with great accessibility to low energies below  $400\text{ cm}^{-1}$ , without compromising the quality of the spectra. QENS measurements, in particular, can readily probe low energy-changes which arise from neutrons being scattered by moving particles, enabling the direct measurement of rotational and translational diffusion.
- Sensitivity of optical techniques generally scales with the atomic number and, by extension, the number of electrons in the atoms under study. Neutrons are distinctly sensitive to  $^1\text{H}$  atoms due to their exceptionally large incoherent scattering cross section – which makes hydrogen up to ten times more ‘visible’ than any other element. Conversely, the incoherent scattering cross section of  $^2\text{H}$  atoms is around forty times smaller allowing the ‘masking’ of certain species or modes.
- Both INS and QENS spectra are readily modelled by classical and molecular dynamics, respectively. This enables, in the case of the former, the correlation between the measured intensities and the displacements of the scattering atoms, as electro-optic parameters are not required. As for the latter, the time (ps) and length ( $\text{\AA}$ ) scales probed are well within the scope of molecular dynamics simulations.

### 2.1.1 Elementary Principles of Scattering<sup>3</sup>

The following principles apply to both X-rays and neutrons, however since scattering using neutrons is the primary theme of this thesis we will focus, accordingly, on the latter. A neutron scattering event is characterised by the change in the neutron's energy,  $E$ , and momentum,  $P$ . This involves an incident particle, with a wavevector  $k_i$  and angular frequency  $\omega_i$ , emerging from a sample with a final wavevector  $k_f$  and frequency  $\omega_f$ , as shown schematically in Fig. 2.1.2.

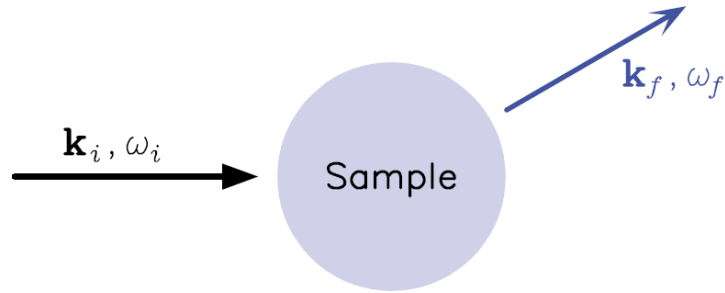


**Fig. 2.1.2. Schematic illustration of the scattering process. Reproduced from Ref. 3.**

When treated as a particle, the energy,  $E$ , of a free neutron with a velocity,  $v$ , is equal to its kinetic energy:

$$E = \frac{1}{2}mv^2$$

The neutron may also be considered as a plane wave, with a wavevector  $k$ , and wavelength  $\lambda$ :

$$k = \frac{m}{\hbar}v \qquad \lambda = \frac{2\pi}{|k|} = \frac{h}{mv}$$

Thus, the kinetic energy of the neutron can be written as:

$$E = \frac{\hbar^2 k^2}{2m} = \frac{h^2}{2m\lambda^2}$$

The energy of incident neutrons is controlled by moderators; i.e., neutrons are thermalised when travelling through a moderator at temperature  $T$ . The resultant average velocities,  $\bar{v}$ , follow a Maxwellian distribution and the energy of the neutrons is given by:

$$\bar{E} = \frac{1}{2}m\bar{v}^2 = \frac{3}{2}k_B T$$

where  $k_B$  is the Boltzmann constant. Indeed at 300 K, the energy of thermal neutrons ( $\sim 25$  meV) is comparable to the intermolecular energies of condensed matter; and the wavevector is of the same order of magnitude ( $\sim 1.8$  Å) as

molecular dimensions within solids. Hence, neutrons are an extremely powerful tool in the attempt to elucidate both dynamical and geometrical properties of matter.

The scattering experiment aims to measure two quantities, the first being the energy transfer:

$$\hbar\omega = E_f - E_i = \frac{\hbar^2}{2m}(k_f^2 - k_i^2)$$

where  $E_i$  and  $E_f$  are the initial and final energies of the neutron, respectively, with  $k_i$  and  $k_f$  the corresponding wavevectors. The second quantity measured is the wavevector transfer which yields the scattering vector:

$$\vec{Q} = \vec{k}_f - \vec{k}_i$$

Since transfer of momentum is inherent due to a change in the direction and/or energy of the neutron, the momentum transfer is given by:

$$P = \hbar\vec{Q} = m\vec{v}_f - m\vec{v}_i$$

When a neutron is scattered elastically, without an exchange in energy, the modulus of the wavevector, and thus the wavelength, remain unchanged:

$$k_i = k_f = \frac{2\pi}{\lambda}$$

Which yields an isosceles scattering triangle, with both sides equal to  $2\pi/\lambda$ . As such, elementary trigonometry gives rise to:

$$Q = 2k_i \sin\theta$$

However, a scattering event in which the neutron either gains or loses energy i.e.,  $k_i \neq k_f$ , results in a scattering triangle which is no longer isosceles. The moduli of these vectors and the scattering angle thus have to be related using the more general formula:

$$Q^2 = k_i^2 + k_f^2 - 2k_i k_f \cos 2\theta$$

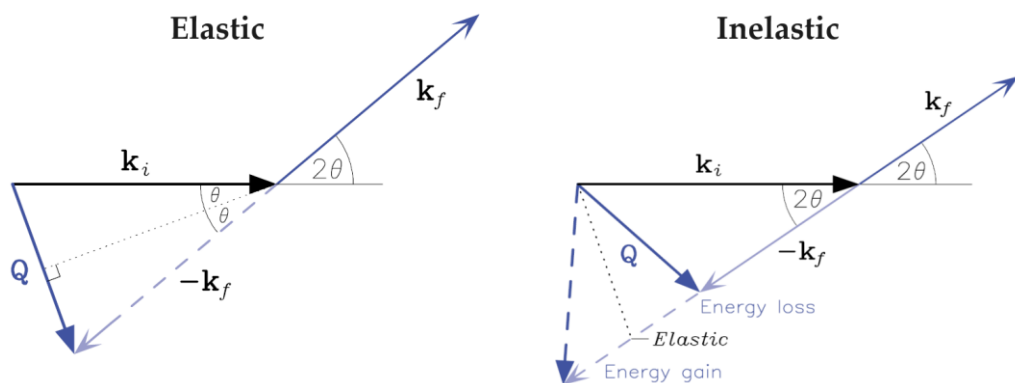


Fig. 2.1.3. Wavevector diagrams for *elastic* and *inelastic* scattering through an angle of  $2\theta$ . Figure adapted from Ref 3.

### 2.1.1.1 Scattering Cross Section<sup>4</sup>

An incident neutron passing near a nucleus encounters two potential outcomes. The first is absorption, where it may become absorbed by the nucleus, resulting in the formation of a compound nucleus in an excited state. The compound nucleus then typically undergoes decay via either  $\gamma$  radiation or, in certain scenarios such as in  $^3\text{He}$  detectors, the emission of charged particles like alpha ( $\alpha$ ) or tritons. Alternatively, the compound nucleus may undergo fission such as that observed in uranium within a reactor core. The second outcome – and the primary focus of our interest – is scattering. In this scenario, the neutron scatters off the nucleus, resulting in changes in both its direction and energy. While thermal neutrons lack the energy to directly excite the nucleus or its electronic shell, they can still undergo inelastic scattering due to the atomic motions within the nucleus. These atomic motions, characterised by significantly lower energies, influence the trajectory and energy of the neutron through the scattering process.

The basic quantity that we aim to measure is the fraction of incident particles which emerge in various directions. If the neutrons form a steady stream of incoming particles then the incident flux is specified by their number per unit time and per unit area, perpendicular to the flow. Thus, given a flux of  $I_0$  neutrons incident on a sample, the number of scattering events occurring each second,  $I_s$ , allows for the definition of a scattering cross section,  $\sigma_s$ , through the relation:

$$I_s = I_0 \sigma_s$$

Where  $\sigma_s$  has a dimension of a surface in units of barn, and where 1 barn is equal to  $10^{-24}$   $\text{cm}^2$ . Alongside the cross section, the other two quantities that are measured include the differential cross section in one direction,  $\Omega$ :

$$\frac{\partial \sigma}{\partial \Omega}$$

Which provides the probability of a neutron exiting the sample within the solid angle element  $d\Omega$  around the direction  $\Omega$ ; and the double differential cross section:

$$\frac{\partial^2 \sigma}{\partial \Omega \partial E} = \frac{1}{\hbar} \frac{\partial^2 \sigma}{\partial \Omega \partial \omega}$$

Which provides the probability of a neutron, with initial incident energy  $E_0$ , departing from the sample within the solid angle element  $d\Omega$  around direction  $\Omega$ , while experiencing an energy exchange  $E = \hbar\omega$ ; also given in barns.

### 2.1.1.2 Coherent and Incoherent Scattering<sup>1,4</sup>

The principles of coherence and incoherence revolve around the manner in which neutrons, functioning as both waves and particles, interact with the scattering entity. When treated as waves, neutrons interact with multiple atomic centres simultaneously, giving rise to new wavefronts which propagate spherically while remaining in phase; thus coherence is preserved if the scattering lattice maintains order. The constructive interference among these wavefronts yields distinct diffraction patterns, characterised by well-defined beams or reflections, only observable in specific spatial directions. This phenomenon is the hallmark of coherent scattering, where the number of reflections is limited and each reflection is correspondingly intense. As the incident neutron wave interacts with numerous atomic centres, the momentum transferred to the sample is distributed across the crystal's network of bonds rather than a single atom.

Conversely, when treating neutrons as particles, their interactions are treated as singular scattering events from distinct scattering centres within the sample. Each scattered neutron is considered as a spherical wave emanating solely from an individual source and devoid of any potential for interference between wavefronts from multiple sources, rendering this process incoherent. This type of scattering manifests as an even distribution of intensity across all directions, with the neutrons scattered indiscriminately, leading to weak scattering strength in any one direction.

The distinction between coherent and incoherent scattering hinges upon the composition of the sample. Scattering events should exhibit coherence where a structure possesses translational symmetry and long-range order. Solids composed of a single nuclear type should therefore yield a purely coherent signal. In reality, however, this theoretical limit is never achieved due to the presence of isotopes which have characteristic coherent and incoherent scattering cross sections. Hence, the total scattering cross section,  $\sigma_{\text{tot}}$ , is a sum of its coherent and incoherent constituents:

$$\sigma_{\text{tot}} = \sigma_{\text{coh}} + \sigma_{\text{inc}}$$

And they are related by the variation and mean of the scattering length,  $b$ , such that:

$$\sigma_{\text{coh}} = 4\pi \langle b \rangle^2$$

and

$$\sigma_{\text{inc}} = 4\pi(\langle b^2 \rangle - \langle b \rangle^2)$$

## 2.1.2 Neutron Production & Transportation<sup>1,5,6</sup>

The high neutron flux required for spectroscopic experiments necessitates the use of specialised neutron sources such as research fission reactors and spallation sources; such experiments are consequently confined to dedicated, large-scale facilities.

Research reactors such as the Australian Nuclear Science and Technology Organisation (ANSTO) exploit the slow-neutron-induced fission of  $^{235}\text{U}$  to produce surplus neutrons beyond those required to sustain a nuclear chain reaction. In a typical reactor, 2.5 neutrons are produced per fission event with 0.5 lost to absorption, 1 utilised to propagate the reaction and 1 available for experimental use. Initially emitted with high energies, these neutrons undergo moderation via repeated inelastic collisions with hydrogenous materials, such as water, resulting in a Maxwell–Boltzmann distribution of neutron energies; e.g., in the case of  $\text{D}_2\text{O}$  moderation at room temperature, the neutron distribution peaks around  $208\text{ cm}^{-1}$ , whilst employing a liquid  $\text{D}_2$  moderator at 25 K yields neutrons with an energy distribution which peaks around  $40\text{ cm}^{-1}$ . The fundamental difference between power and research reactors is the undesirability of heat, a byproduct of the chain reaction, in the latter, where its removal limits the maximum size – and the flux – of the reactor. Research sources provide a steady supply of cold and thermal neutrons, albeit with a narrower energy spectrum, and they are less efficient at producing epithermal neutrons which are crucial for neutron vibrational spectra.

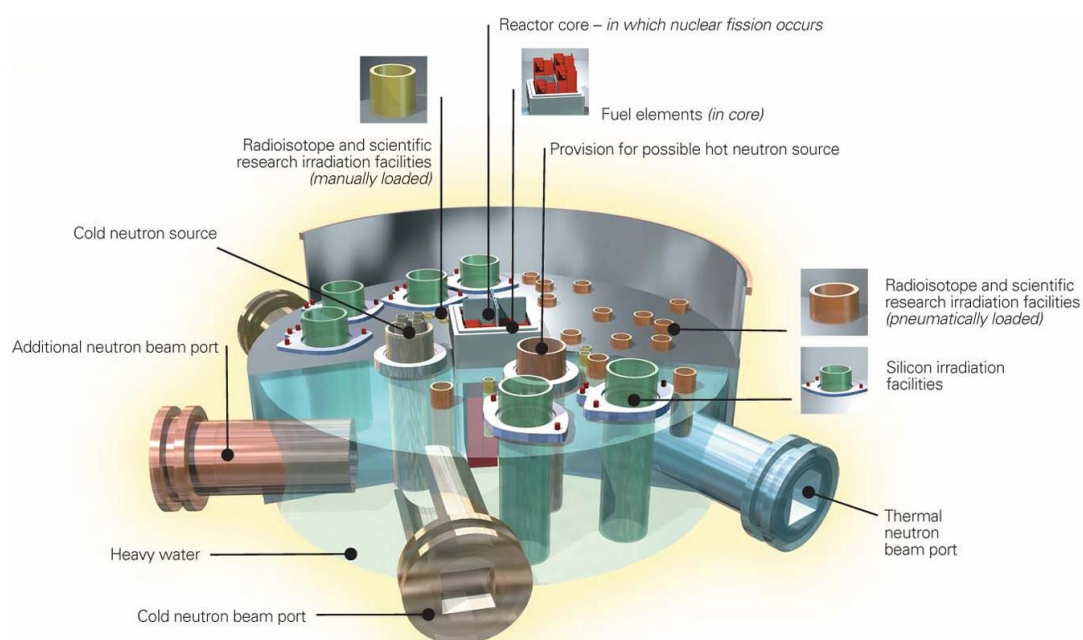
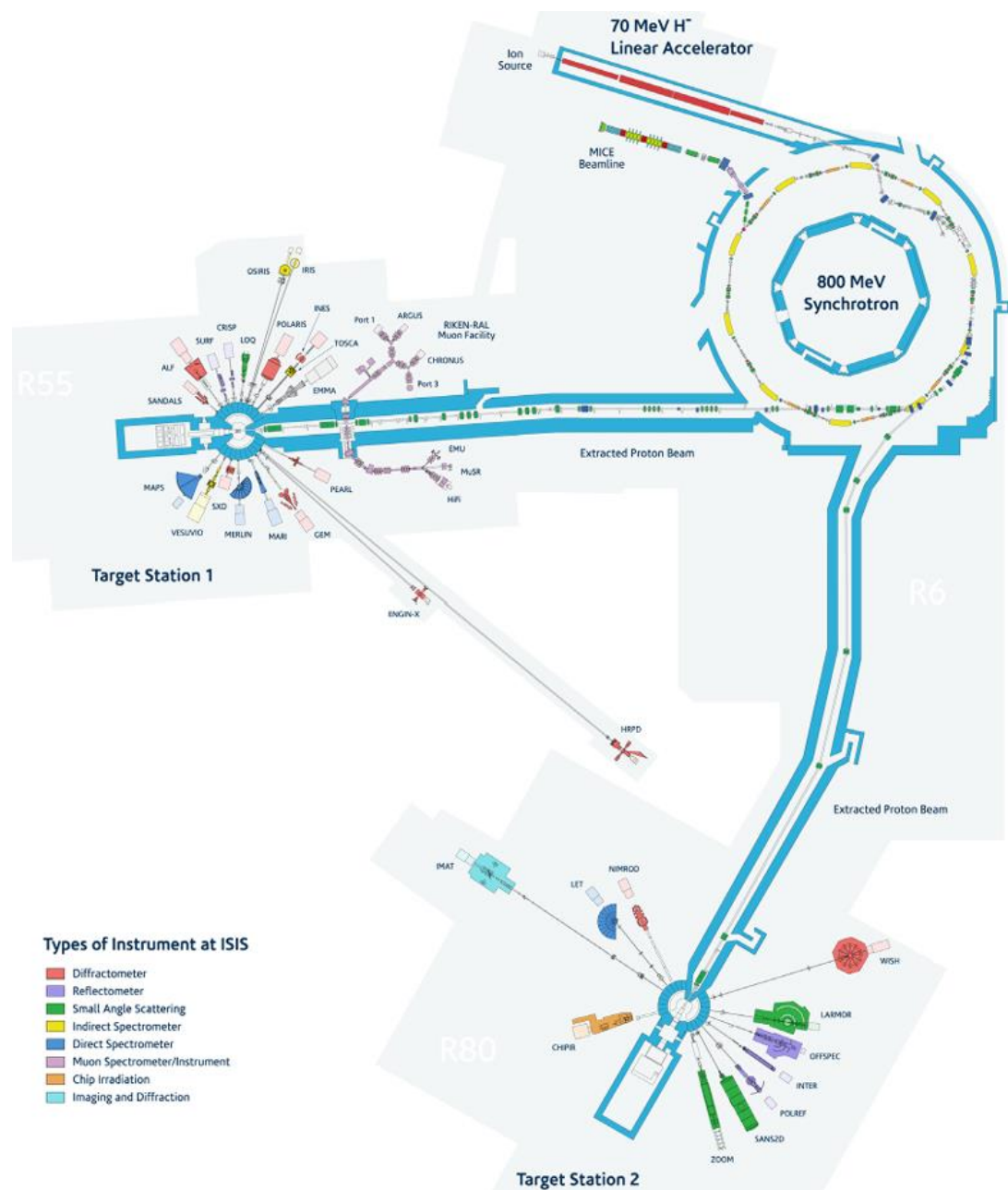


Fig. 2.1.4. Schematic of the OPAL fission reactor at ANSTO. Figure reproduced from Ref. 5.

Spallation sources like the ISIS Neutron & Muon Source produce neutrons by bombarding a heavy-metal target (typically Hg or W) with pulses of high-energy protons from a particle accelerator. Upon hitting the target nuclei, the protons instigate an intranuclear cascade which excites individual nuclei to highly energetic states. Consequently, the nuclei release the energy via evaporation of nucleons (primarily neutrons), some of which propagate the cascade whilst others leave the target material. Since each high-energy proton reaching the target yields approximately 15 neutrons, spallation sources produce incredibly intense neutron pulses with only a fraction of heat of a reactor source.



**Fig. 2.1.5. Schematic of the ISIS Neutron & Muon Source in Harwell, UK. Figure reproduced from Ref. 6.**

Similar to reactor sources, the neutrons produced by spallation necessitate moderation to useful energies prior to being utilised experimentally. However, in spallation sources this is achieved using smaller moderator tanks in order to maintain a narrow pulse-width crucial for optimal energy resolution. Consequently, a neutron pulse produced at a spallation source contains a substantial proportion of epithermal neutrons, enhancing the capabilities for vibrational spectroscopy.

Following production, neutrons must be directed and transported to the relevant instruments for experimental use. Being uncharged, neutrons travel in straight paths after moderation, necessitating clustered instrument arrangements around the source. Given their neutral nature, neutrons interact with samples and other components purely by chance, making it challenging to control their trajectory. To mitigate flux decay, flight paths between the moderator and the sample must be minimised, with beam tubes evacuated to prevent scattering from air. For low-energy neutrons, neutron guides, typically square or rectangular tubes made from metal (preferably nickel) coated flat glass, may be employed. These guides facilitate total external reflection of long-wavelength neutrons from the metal surface, effectively keeping them within the guide. Furthermore, effective shielding of sources, beamlines and instruments is essential for operator safety as well as the prevention of stray neutron interference during experiments. Materials with high neutron adsorption cross-sections such as boron, cadmium or gadolinium are thus employed for shielding purposes.

### **2.1.3 Inelastic Neutron Scattering (INS) Spectroscopy<sup>7-9</sup>**

Numerous methods exist for the analysis of the vibrational spectrum of materials, each with its own applicability to different systems. These techniques can generally be categorised into two main classes: those involving the absorption or emission of photons with energies matching vibrational transitions; and those where particles undergo inelastic scattering by a material, resulting in a change in the particle's energy equivalent to the vibrational transition energy. INS falls in the latter of these two classes which will thus be considered here in isolation.

INS spectroscopy covers a broad energy range, extending from microwave to ultraviolet frequencies and offering a wide array of applications. However, focus herein is directed to the infrared region ( $0 - 4000 \text{ cm}^{-1}$ ) which concerns

the study of bond vibration frequencies in molecules. Some of the advantages of INS are covered in **Section 2.1**, but it is paramount to reiterate the key difference between neutron spectroscopy and other optical techniques such as Raman or Infrared (IR) spectroscopy. By virtue of having a mass, an inelastic scattering event involving a neutron results in a significant transfer of both the energy ( $E, \text{cm}^{-1}$ ) and momentum ( $\mathbf{Q}, |\mathbf{Q}| = Q, \text{\AA}^{-1}$ ) resulting in a scattering intensity unconstrained by electro-optical parameters governing IR and Raman scattering. The scattering intensity,  $S$ , is given by:

$$S(Q, n\omega_i) \propto \frac{(QU_i)^{2n}}{n!} \exp [(-QU_{Tot})^2] \sigma$$

Where  $\omega_i$  represents the  $i^{\text{th}}$  mode at frequency  $\omega$ ;  $n = 1$  for a fundamental mode, 2 for a first overtone or binary combination, 3 for a second overtone or ternary combination, etc;  $Q$  denotes the momentum transfer;  $U_i$  signifies the root mean square displacement of the atoms in the mode; and  $\sigma$  is the inelastic scattering cross section of the atom. The exponential term corresponds to the Debye-Waller factor where  $U_{Tot}$  represents the total root mean square displacement of all atoms in all modes (both internal and external). Its magnitude is primarily determined by the thermal motion of a molecule; cooling the sample can diminish this effect and, therefore, INS spectra are typically collected at  $T < 30 \text{ K}$ .

### 2.1.3.1 INS Instrumentation<sup>10,11</sup>

Inelastic neutron scattering spectrometers fall into three main types. The first, and most prevalent, is the triple-axis spectrometer primarily used for coherent scattering measurements at reactor sources. The second is a direct geometry spectrometer in which the incident energy of the neutrons is fixed and the range of energy of the scattered neutrons is measured. The third type – and the one relevant to this thesis – is the indirect geometry instrument wherein the final energy of the scattered neutrons is fixed, whilst the incident neutrons have a continuous spectrum of energy. Spectrometers of this latter type have traditionally been the preferred choice for vibrational spectroscopy experiments due to their detector design, which remains constant without energy variation throughout the measurement process.

The TOSCA spectrometer at the ISIS Neutron & Muon Source was used to perform INS measurements for this thesis and is an exemplar of the indirect geometry design. In this setup, a pulse of high-energy neutrons generated from the target is moderated in water at room temperature. A disk chopper, which is placed between the moderator and the sample environment, then

serves a dual purpose of removing any remnant high-energy neutrons and preventing frame overlap. Neutrons scattered from the sample are then directed towards two analysers positioned at  $45^\circ$  and  $135^\circ$  for forward and backward scattering, respectively. These neutrons undergo Bragg reflection from the pyrolytic graphite analyser, operating at an energy of  $32 \text{ cm}^{-1}$  (4 meV). A cooled beryllium filter then filters out any high-energy neutrons. The detectors employed consist of a total of 10 banks, with 5 dedicated to each analyser. Each detector bank comprises of 13  $^3\text{He}$  tubes, facilitating the capture and analysis of neutron scattering events. Since the precise flight-path of the neutrons is known, back calculations allow the determination of the energy of the incident neutrons and thus the scattering process.

### **2.1.3.2 INS Experimental Procedure**

Samples subjected to INS measurements were processed in an argon-filled glovebox to prevent atmospheric contamination. The samples were then packaged into aluminium foil and loaded into flat-plate aluminium sample cells ( $50 \times 50 \text{ mm}$ ) sealed with indium wire gaskets to ensure a gas-tight seal. The cells were subsequently attached to a 'centre-stick' with the length adjusted to position the sample in the centre of the neutron beam and placed into the instrument. The sample environment within the TOSCA instrument contains a closed-circuit refrigerator (CCR) which, following sample loading, is purged with helium to eliminate spectral interference and prevent ice formation from vapour or air. The sample chamber is then refilled with  $\sim 30 \text{ mBar}$  of helium which acts as an exchange gas whilst the sample is being cooled below 20 K. The sample temperature is monitored at all times using a temperature sensor and data acquisition may begin only once the sample has cooled below 20 K. Post-measurement, the samples must be handled carefully and without any direct contact due to the radioactivity induced by the neutron beam. A Geiger counter is available at the beamline at all times and must be used to check the samples' activity prior to offloading. The data acquired is then reduced and analysed using Mantid.<sup>12</sup>

### **2.1.4 Quasielastic Neutron Scattering (QENS)**<sup>4,13–15</sup>

Quasielastic neutron scattering (QENS) refers to processes in which the scattering nucleus moves freely in space and time, manifesting as Doppler broadening of the elastic line in the neutron energy spectrum,  $S(Q, \omega)$ , rather

than discrete peaks associated with inelastic scattering; i.e., the neutrons are scattered with minimal energy transfer. The elastic component arises from scattering by atoms localised in space or which are moving too slowly to be resolved within the instrument's resolution; the inelastic peaks originate from atoms vibrating periodically with a fixed frequency; while the quasielastic broadening is the product of scattering by atoms undergoing stochastic motion. As such, QENS occurs within a scattered energy range of ca.  $\pm 2$  meV to sub- $\mu$ eV levels, corresponding to motions taking place on timescales in the pico- to nanosecond range.

As with the scattering cross-sections, the quantity measured in neutron scattering experiments, i.e., the double-differential scattering cross section, can be divided into its coherent and incoherent counterparts:

$$\frac{\partial^2 \sigma}{\partial \Omega \partial E} = \frac{k_f}{k_i} \frac{1}{4\pi \hbar} [\sigma_{\text{coh}} S_{\text{coh}}(Q, \omega) + \sigma_{\text{inc}} S_{\text{inc}}(Q, \omega)]$$

where  $S_{\text{coh}}(Q, \omega)$  and  $S_{\text{inc}}(Q, \omega)$  denote the coherent and incoherent scattering functions (or dynamical structure factors), respectively. The coherent component reveals interference effects among atoms enabling their mutual behaviour, such as transport properties, to be probed. The incoherent part, on the other hand, pertains to scattering from individual atoms, providing information about their discrete motions, also known as self-dynamics. The Fourier transforms of  $S_{\text{coh}}(Q, \omega)$  and  $S_{\text{inc}}(Q, \omega)$  factors yield intermediate scattering functions  $I_{\text{coh}}(Q, t)$  and  $I_{\text{inc}}(Q, t)$ , respectively; which, in turn, are Fourier transforms of the total and self, real space-time van Hove<sup>16</sup> correlation functions,  $G(r, t)$  and  $G_{\text{self}}(r, t)$ , respectively. Hence, the space-time correlation functions are incorporated into the scattering functions in a QENS experiment:

$$S_{\text{coh}}(Q, \omega) = \left(\frac{1}{2\pi}\right) \iint G(r, t) \exp[iQ \cdot r + \omega t] dr dt$$

$$S_{\text{inc}}(Q, \omega) = \left(\frac{1}{2\pi}\right) \iint G_{\text{self}}(r, t) \exp[iQ \cdot r + \omega t] dr dt$$

where the pair correlation function,  $G(r, t)$ , provides the probability of finding any nucleus at position  $r$ , at time  $t$ , if a particular atom was at origin at time  $t = 0$ ; and the self-correlation function,  $G_{\text{self}}(r, t)$ , represents the probability of finding a nucleus at position  $r$ , at time  $t$ , if that same nucleus was at the origin at  $t = 0$ . Since  $r$  and  $t$  are Fourier-transformed variables of  $Q$  and  $\omega$ , respectively, long distances in real space correspond to small values of  $Q$ , and *vice versa*. Similarly, slow diffusivities which imply long times in  $G(r, t)$  correspond to small  $\omega$ . In Einstein or tracer diffusion – the self-diffusion probed by incoherent QENS – a timescale significantly exceeding the mean time between individual diffusive jumps (and assumed to be uncorrelated),

leads to the self-correlation function taking the form of a Gaussian with a mean square deviation of  $\langle r^2 \rangle = 6D_s$ , where  $D_s$  is the tracer diffusion coefficient. Substituting this expression into the incoherent scattering function yields:

$$S_{\text{inc}}(Q, \omega) = \frac{(1/\pi)(D_s Q^2)}{[(D_s Q^2)^2 + \omega^2]}$$

which represents a normalised Lorentzian, in terms of  $\omega$ , with half width at half maximum (HWHM, also referred to as  $\Gamma$ ) of  $D_s Q^2$ . This, in other words, describes continuous long-range translational diffusion whereby particles move freely under collisions, resulting in random changes in direction. Thus observing the quasielastic width as a function of  $Q^2$  enables the determination of  $D_s$  ( $\text{m}^2\text{s}^{-1}$ ), with a linear response indicating continuous diffusion.

Real systems, however, often exhibit deviations from this ideal behaviour due to various factors, such as H-bonding, leading to residence periods between jumps. Revised models, known as jump diffusion models, have been developed to account for these deviations – especially at small length scales (and therefore large  $Q$ ). These models (depicted in Fig. 2.1.6) display  $D_s Q^2$  behaviour at low  $Q$  and then approach an asymptote, related to  $1/\tau_{\text{jump}}$ , at higher momentum transfer.

If the diffusing entity is no longer able to move freely but is instead geometrically anchored, the constrained motion, whether continuous or defined by jumps between specific sites, is referred to as localised. In this case, both an elastic signal and a quasielastic response are present. In contrast to

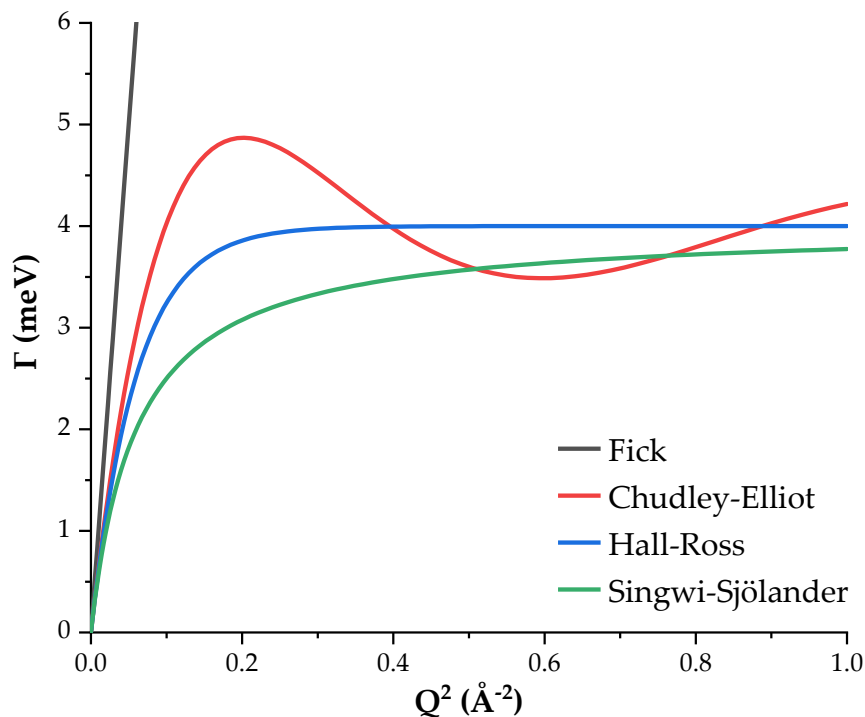


Fig. 2.1.6.  $Q$ -dependencies of  $\Gamma$  according to different diffusion models.

translational diffusion, however,  $Q$ -independent linewidths are observed which typically correspond to rotational motions.

Systems characterised by jump diffusion under confinement allow for the copresence of both  $Q$ -independent and  $Q$ -dependent linewidth behaviour. For example, jump diffusion in one dimension between two walls, separated by a distance  $L$ , will exhibit linewidths with distinct asymptotic trends at low and high  $Q$  values. At low  $Q$ , concerning large scales, narrow boundaries significantly influence the diffusion process, causing the linewidth to deviate from the  $D_s Q^2$  law and tend to a finite  $\Gamma$  value, indicating the effective linear dimension of the confining medium. This dimension can be inferred from the upper  $Q$  limit of the linewidth plateau, corresponding to  $\sim 2\pi/L_{\text{conf}}$ . At high momentum transfer values, where motion occurs over short distances ( $l \ll L_{\text{conf}}$ ), and the elementary displacement of particles is not infinitesimally small, the  $\Gamma$  of the quasielastic component tends toward  $1/\tau_{\text{jump}}$ . Between these extremes, the system recovers the  $D_s Q^2$  response, as the dimension of the boundaries becomes insignificant compared to the small distances relative to the confining medium.

The specific diffusion models used in this thesis will be described alongside the relevant results obtained in Chapter 4.

#### 2.1.4.1 QENS Instrumentation<sup>14</sup>

Quasielastic neutron scattering is performed on three primary types of spectrometers. The first is the neutron spin echo (NSE) spectrometer which employs spin-polarised neutron beams to track quasielastic scattering and assess the response in terms of the intermediate scattering function,  $I(Q, t)$ . These instruments are adept at probing length scales up to 500 Å and temporal range approaching microseconds. NSE operates using a band of spin-polarised incident neutron wavelengths,  $(\Delta\lambda_i)$ , and is primarily used for investigating collective motions.

The second two, known as direct and indirect geometry instruments, share broad design similarities and assess the quasielastic response in terms of the dynamic structure factor,  $S(Q, \omega)$ . They typically access length scales ranging 1 – 30 Å and temporal range of around 1 – 6000 picoseconds. These instruments operate by defining either the initial energy,  $E_i$ , for direct geometry or the final energy,  $E_f$ , for indirect geometry and are commonly employed for the study of local, self-motions.

Direct geometry instruments are better suited for the measure of  $Q$ - $\omega$  space, in terms of neutron energy gain, and can access a wider energy transfer window and higher neutron energies, rendering them suitable for the study of high-energy transfer inelastic events as well as quasielastic phenomena. Alas, they afford inferior resolution when compared to indirect geometry instruments.

NSE and direct geometry instruments were not utilised during this project and, henceforth, will not be discussed further.

#### 2.1.4.2 Indirect Geometry Instruments<sup>14</sup>

As aforementioned, indirect geometry instruments operate by conveying a finite distribution of incident neutron energies,  $\Delta E_i$ , to the sample position and identifying a single energy value,  $E_f$ . Within research reactor facilities, e.g., EMU at ANSTO, these types of instruments utilise a monochromator, typically single crystal, positioned prior to the sample which selectively reflects neutrons with energies satisfying the Bragg condition toward the sample. The monochromator introduces a slight Doppler shift, by virtue of being mounted on a mechanical Doppler unit, causing the incident neutron beam to exhibit a finite energy distribution,  $\Delta E_i$ . In this mode, the instrumental electronics categorise the detected neutrons into energy channels based on the velocity attributes of the Doppler drive, at the moment of Bragg reflection towards the sample. Indirect geometry instruments operating in Time-of-Flight (ToF) mode, where neutron detection relies on flight time, as in IRIS at the ISIS Neutron & Muon Source, employ bandwidth choppers (neutron-absorbing discs with wide neutron-transparent apertures) to transmit a narrowed band of incident neutron energies to the sample.

Both pulsed and reactor source indirect geometry instruments analyse the scattered neutron beam to define the final energy,  $E_f$ . This is done by deploying a large (to enhance the detected flux) array of single crystals – typically silicon or pyrolytic graphite – between the sample and the detector; neutrons leaving the sample with wavelengths satisfying the Bragg condition are thus isolated for reflection towards the detector.

The sensitivity of indirect geometry instruments is restricted by various factors. The energy resolution of a backscattering instrument at a pulsed neutron source can be expressed through a combination of ToF uncertainty ( $\Delta t$ ), instrument length uncertainty ( $\Delta L$ ), lattice spacing uncertainty ( $\Delta d$ ), and beam divergence ( $\Delta \theta$ ) all added in quadrature, if they are assumed to be statistically independent, such that:

$$\left(\frac{\Delta E}{2E}\right)^2 = \left(\frac{\Delta t}{t}\right)^2 + \left(\frac{\Delta L}{L}\right)^2 + \left(\frac{\Delta d}{d}\right)^2 + (\cot(\theta) \Delta(\theta))^2$$

Which can further be grouped into primary and secondary contributions associated with both  $E_i$  and  $E_f$ . For research reactor-based instruments, this equation can be reduced to:

$$\left(\frac{\Delta E_f}{2E_f}\right) = \left(\frac{\Delta d}{d}\right) + (\cot(\theta) \Delta(\theta))$$

Achieving optimal energy resolution, therefore, necessitates ensuring the energy-analysed beam undergoes Bragg scattering through  $180^\circ$  with negligible timing uncertainty. At a research reactor, this mandates the detector array to be placed directly behind the sample position, characterising these setups as backscattering instruments. This configuration enables high energy resolution, albeit at the expense of a substantial energy transfer window. In contrast, indirect geometry ToF instruments at pulsed sources operate with  $\theta$  close to  $180^\circ$  with their detector array positioned slightly below the sample position, characterising these setups as near-backscattering spectrometers. Although potentially less sensitive, this regime provides access to wide dynamic ranges and offers substantial enhancements in neutron flux.

### 2.1.4.3 The IRIS Spectrometer<sup>17</sup>

IRIS is a high resolution quasielastic neutron scattering instrument operating in indirect geometry and employing the time-of-flight technique for data analysis. The spectrometer is located at the N6 beamline of ISIS and utilises a liquid hydrogen moderator, cooled to 25 K, which provides a substantial flux of long-wavelength cold neutrons. The instrument can be divided into two main sections.

The ‘primary’ spectrometer facilitates neutron beam transport from the moderator to the sample position via a neutron guide which primarily comprises aligned nickel-plated glass tubes, terminating with a 2.5m-long converging nickel-titanium supermirror. The supermirror enhances the incident flux (by a factor of 2.9 at 5 Å) and focuses the beam at the sample position (32 × 21 mm). The incident neutron flux at full ISIS intensity is  $5.0 \times 10^7$  n/cm<sup>2</sup>s<sup>1</sup> with the wavelength intensity up to 18 Å. Following moderation, neutrons either pass through or are absorbed by one of the two

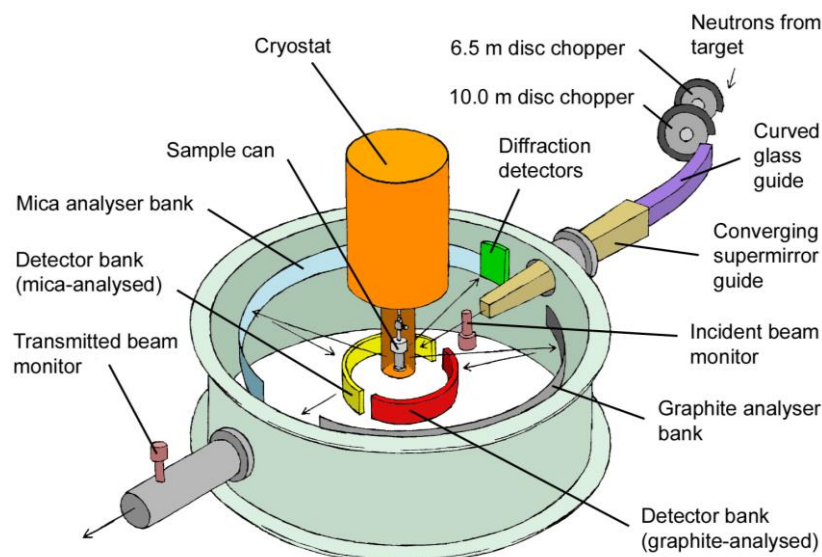


**Fig. 2.1.7. Schematic of the IRIS Spectrometer at the ISIS Neutron & Muon Source. Reproduced from Ref. 17.**

disc-choppers, depending on their incident energy. The choppers, located at 6.3 and 10 m from the moderator, define the range of neutron wavelengths incident upon the sample; and their operation frequency (50, 25, 16.6 or 10 Hz) adjusts the lower and upper limits of the incident wavelength band. Consequently, they define the energy resolution and energy-transfer (inelastic) or d-spacing range (elastic) covered during an experiment.

The secondary spectrometer comprises a 2 m diameter vacuum vessel housing two crystal analyser arrays (pyrolytic graphite, muscovite mica or fluorinated mica); two 51-element ZnS scintillator detector banks; and a diffraction bank at  $2\theta = 170^\circ$  containing ten  $^3\text{He}$  gas-tube detectors. The pyrolytic graphite analyser bank is cooled to  $\sim 10$  K to reduce background contributions from thermal diffuse scattering.

#### **2.1.4.4 The EMU Spectrometer<sup>18,19</sup>**

EMU is a cold-neutron backscattering spectrometer installed in the neutron guide hall of the OPAL research reactor at ANSTO. It operates as a crystal analyser spectrometer utilising Si (111) crystals configured for backscattering to achieve high energy resolution. A pair of highly-oriented pyrolytic graphite crystal pre-monochromators are used to extract a  $32 \times 21$  mm beam from the OPAL CG3 cold-neutron guide using their (002) reflection. A cooled beryllium block between the pre-monochromators scatters out higher-order reflections; while a disc chopper reduces downstream background. A 7 m-long

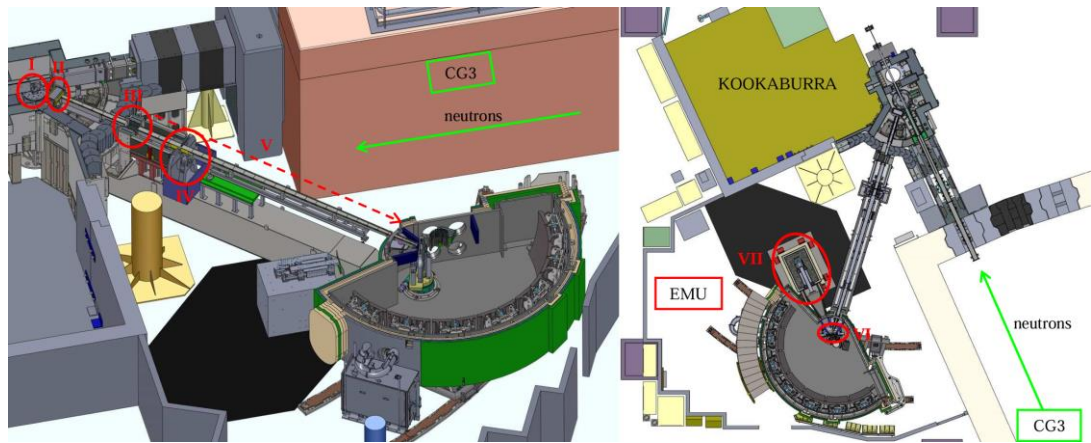


**Fig. 2.1.8. Schematic of the EMU Spectrometer at ASNTO. Highlighted is the pre-monochromator (I); cooled Be filter (II); tertiary shutter (III); background chopper (IV); focusing guide (V); graphite chopper (VI); and the backscattering monochromator (VII). Adapted from Ref. 19.**

supermirror guide is then used to focus the beam to  $3 \times 3 \text{ cm}^2$  onto the second pre-monochromator.

The second pre-monochromator, integrated with graphite elements at the periphery of a disc (graphite) chopper, directs the beam onto the scattering sample after returning from a Si (111) monochromator. Scattered neutrons are analysed by an  $8 \text{ m}^2$ , 1.8 m-radius spherical array of Si (111) crystals, providing a vertical coverage angle of  $\pm 30^\circ$ . Detection of the scattered neutrons is facilitated by 51 linear-position-sensitive  $^3\text{He}$  detectors aligned with the analyser array.

EMU achieves incident energy modulation through Doppler shifting of the monochromatised neutrons, via rapid mechanical oscillations of the backscattering monochromator (Doppler drive), while maintaining a fixed final energy. The Si (111) crystal and monochromator arrays are precisely configured for near-perfect backscattering by focusing onto the scattering sample. This is achieved by deforming the silicon crystal wafers to match their 1.8 m-radius support surfaces, which broadens the narrow width of their Bragg reflection. Consequently, this backscattering condition defines the spectrometer's  $6.27 \text{ \AA}$  wavelength and its momentum range. The capability to uphold the backscattering condition even at the smallest accessible scattering angles enables exceptional  $\sim 1.1 \text{ \mu eV}$  resolution at momentum transfers down to  $0.1 \text{ \AA}^{-1}$ .

### 2.1.4.5 QENS Experimental Procedure

The samples subjected to QENS measurements were handled in an argon-filled glovebox where they were weighed, placed into aluminium cans and sealed using indium wire gaskets, to ensure a gas-tight seal. The sample cans were annular in geometry which ensures constant sample thickness irrespective of the scattering angle, resulting in isotropic scattering, whilst also optimising the utilisation of the neutron beam area. The loaded and sealed cell is then removed from the glovebox and attached to the centre-stick, with the length adjusted to ensure the sample is situated in the centre of the neutron beam. The sample was then placed into the instrument featuring a CCR, where it was evacuated and purged to remove air and prevent spectral interference as well as ice formation; the sample chamber was then refilled with  $\sim 30$  mBar of helium which acts as an exchange gas. The sample is then cooled to base temperature ( $\sim 5$  K) to obtain a spectrum of the instrumental resolution – this can either be an empty sample, i.e., dry zeolite, or a reference material such as a vanadium can. Information relating to the composition of samples and the dosing thereof, as well as the instrumental configuration, measurement temperatures and data analysis will be discussed in further detail alongside the relevant results in Chapter 4.

## 2.2 Muon Spectroscopy<sup>20</sup>

Muon Spectroscopy traces its origins to a discovery, made in 1936, by Carl David Anderson and Seth Neddermeyer. While studying cosmic rays at the California Institute of Technology, they observed distinctive tracks in a cloud chamber, influenced by magnetic fields. Those tracks provided essential data for determining the velocity and momentum-to-charge ratio of particles, both of which enabled the derivation of the mass-to-charge ratio and have led to the identification of a novel elementary particle – the muon.

This new particle, represented by the symbol  $\mu$ , exhibited either a positive or a negative charge and had an intermediate mass between the light electron (a lepton) and the heavy proton (a baryon), leading to its initial categorisation as a meson. Hideki Yukawa's 1935 prediction of the meson as the mediator of strong nuclear interaction initially seemed to align with the muon's properties, as its mass corresponded well with Yukawa's predictions. The muon's relatively weak interaction with matter, however, contradicted the

expectations. Subsequent studies led to the pion, denoted by the symbol  $\pi$ , identified as Yukawa's meson and the short-lived precursor of the muon.

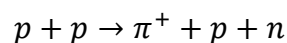
Muon spectroscopy is a collection of methods which utilise the spin of muons to examine the structural and dynamic processes within materials at the atomic scale. This technique is known as  $\mu$ SR, where the acronym assumes different meanings depending on the application and the type of experiment performed, i.e., Muon Spin Rotation, Relaxation and/or Resonance.

While both positive and negative muons may be used in  $\mu$ SR, their interactions with matter have significant variations. The negative muon, being analogous to a heavy electron, is readily captured by nuclei. This capture process leads to a notable loss of spin polarisation and the emission of radiation, thereby diminishing the measured lifetime. This renders the positive muon as the preferred option for most condensed matter applications. Thus, references to muons and  $\mu$ SR will henceforth denote the utilisation of positive muons only.

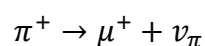
### 2.2.1 Muon Properties & Production<sup>21</sup>

Muons are elementary antiparticles which, together with electrons and tauons, belong to the lepton family. Muons possess spin ( $1/2$ ) and charge ( $+e$ ) identical to positrons, but with a mass approximately 200 greater than the electron and 9 times smaller than the proton. Furthermore, the lifetimes of protons and electrons are infinite in comparison to that of muons (at  $2.2 \mu\text{s}$ ), despite the latter having the longest lifetime of any unstable elementary particle. Muons' magnetic moment, approximately three times that of a proton, renders them exceptionally sensitive to small magnetic fields; this sensitivity makes them invaluable tools for probing weak magnetism within materials.

Muons may be produced naturally, such as those emitted by cosmic rays, or by an accelerator source. The latter is the basis of experimental muon generation, where controlled, low-energy muons that can be thermalised in a sample are required. In this process, a proton beam is directed at a target, such as beryllium or carbon, producing a pion, a proton and a neutron:

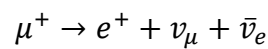


Muons are then generated alongside muon neutrinos, through the two-body decay of charged pions which have a lifetime of 26 ns; the resulting muon inherits its charge from that of the original pion:



To ensure that the decay of a pion complies with the fundamental laws of physics, it must uphold the principles of momentum and spin conservation. When a pion, which lacks its own spin, undergoes decay while at rest, it splits into a muon and a neutrino. During this decay process, the two resulting particles move away from the original pion's position with opposite momenta. Notably, a neutrino's spin is always aligned opposite to its direction of momentum. Hence, if the pion is stationary, all neutrinos will share the same spin orientation. Consequently, all the muons produced will also possess identical spins. This condition creates a completely spin-polarised beam, assuming the pions remain at rest throughout the decay process.

The generated muons themselves undergo a three-body decay process, emitting a positron, a muon neutrino and an electron neutrino:



A fundamental property of this decay process is the non-isotropic emission of the positron. Put another way, instead of having an equal chance of emerging in any direction, the positron is emitted preferentially along the axis aligned with the muon's spin at the moment of its decay. By discerning the direction in which the positron is emitted, we can deduce the orientation of the muon's spin at the time of its decay.

Since each muon has a unique lifespan according to the radioactive decay law, the detection of each positron contributes to a data point at a specific time,  $t$ . By accumulating numerous positron detections spanning millions of muon decays, we construct a histogram which serves to illustrate the average spin polarisation of the extensive ensemble of muons over time. Thus, the dataset obtained from an experiment consists of the compiled average spin polarisation values, measured as a function of time following implantation.

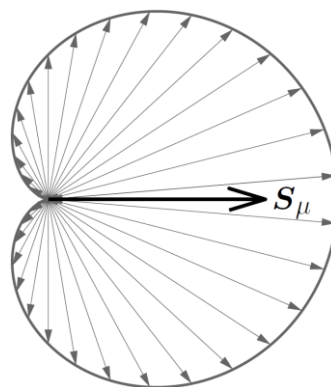


**Fig. 2.2.1** Positrons are preferentially emitted along the muon spin direction, indicated by the length of each grey arrow. Reproduced from Ref. 20.

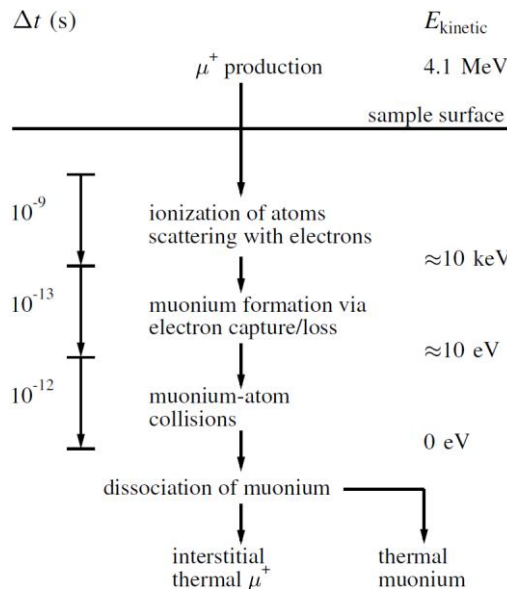


**Fig. 2.2.2. Thermalisation of surface muons post-implantation. Reproduced from Ref. 20**

## 2.2.2 Muon Implantation<sup>20</sup>

To conduct  $\mu\text{SR}$  effectively, it is essential to decelerate the muons to thermal energies before implanting them into the sample under investigation. This can be achieved by introducing a sample of sufficient thickness into the path of the muon beam; or by positioning a material in front of the sample to slow down or degrade the beam. Muons introduced into a sample are 100 % spin polarised and have an implantation range of 0.1 – 1.0 mm, depending on the density of the material. Although muons with an energy of  $\sim 4.0 \text{ MeV}$  are produced, they rapidly undergo thermalisation (within  $10^{-9} - 10^{-12} \text{ s}$ ), ultimately localising within interstitial crystallographic sites with negligible loss of polarisation. The muons' kinetic energy is gradually reduced to a few tens of keV through inelastic scattering, primarily via atomic excitations and ionisations involving Coulombic interactions. At lower energies, muons engage in collective excitations and charge exchange processes, forming muonium ( $\text{Mu}^0, \mu^+ e^-$ ) atoms through electron capture and release, further reducing the muon energy to a few hundred eV. Upon the formation of the muonium bound state, final thermalisation occurs, in most cases, through collisions between muonium and sample atoms until the muonium dissociates into a thermal  $\mu^+$  and a free  $e^-$ .

The final muon states are commonly categorised using the terms diamagnetic and paramagnetic, which reflect the magnetic properties of the electrons to which the muon is linked, given that the electronic moment significantly surpasses that of the muon. A diamagnetic muon state occurs when the muon

is not associated with any unpaired electron density, which could arise because the muon is not strongly coupled to any electrons ( $\text{Mu}^+$ ) or because it is linked to two electrons in a singlet state ( $\text{Mu}^-$ ). Alternatively, a paramagnetic muon state arises when the muon forms a strong bond with a single unpaired electron, as observed in neutral muonium ( $\text{Mu}^0$ ).

### 2.2.3 Muon Experimentation<sup>20</sup>

As aforementioned, the muon decay process, during which a positron is emitted, provides insight into the muon's state at the time of its decay. Two experimental geometries are commonly employed, with the magnetic field's orientation defined as the z-axis. The first is the longitudinal field (LF, which includes zero field, ZF) orientation. In these measurements the detectors are aligned parallel and antiparallel to the muon beam's initial polarisation, termed forward (F) and backward (B) detectors, respectively. In LF and ZF experiments, the time evolution of the positron,  $N(t)$ , is expressed as:

$$N(t) = N_0 \exp\left(-\frac{t}{\tau_\mu}\right) [1 + a_0 P_z(t)]$$

where the exponential term represents the muon decay with a lifetime  $\tau_\mu$ ;  $a_0$  is the initial asymmetry; and  $P_z(t)$  is the longitudinal polarisation function reflecting the time-dependent polarisation of the muon which is equivalent to the longitudinal relaxation function,  $G_z(t)$ . In order to extract the polarisation or relaxation functions,  $P_z(t)$  or  $G_z(t)$ , respectively, which are the quantities of interest, the forward-backward asymmetry is calculated as:

$$A(t) = \frac{N_F(t) - \alpha N_B(t)}{N_F(t) + \alpha N_B(t)} = a_0 P_z(t) = a_0 G_z(t)$$

Where  $N$  denotes the detector counts and  $\alpha = N_F/N_B$  is the calibration factor compensating for the differing scaling factors of the detectors or detector banks. This calibration factor is typically estimated for muons in a diamagnetic state via the application of a small transverse field and adjusting  $\alpha$  to provide  $A(t)$  oscillating symmetrically around zero. Typical functional representations for  $G_z(t)$  include the Kubo-Toyabe function, a damped cosine waveform, an exponential decay function or a combination thereof (*vide infra*).

The second type of measurement is in transverse field (TF), where the initial polarisation direction aligns with the x-axis, perpendicular to the magnetic field,  $B_{TF}$ , along the z-axis. In this case, the polarisation function shifts to describe the transverse polarisation function,  $P_x(t)$ :

$$P_x(t) = \cos(\gamma_\mu B_{TF} t) G_x(t)$$

here,  $\gamma_\mu$  represents the gyromagnetic ratio of the muon while  $B_{TF}$  denotes the transverse magnetic field. This function requires multiple detectors, or groups thereof, evenly distributed around the field axis to maximise the signal. The corresponding detector signals are given by:

$$N_i(t) = N_i^0 \exp(-t / \tau_\mu) [1 + A_i(t)]$$

where  $N_i^0$  serves as a scaling parameter for the count rate in the  $i^{th}$  detector and the asymmetry functions of the detector groups are defined as  $A_i(t) = a_i P_i(t)$

## 2.2.4 Muon Spin Relaxation Functions<sup>20-22</sup>

The primary focus of time-differential  $\mu$ SR involves the analysis of what are commonly known as “relaxation functions”. In this context, “relaxation” denotes alterations in the muon asymmetry; specifically, the time-evolution of muon polarisation, regardless of whether these alterations arise from reversible processes or not. Subsequent interpretation of these relaxation functions aims to delineate their connection to the fundamental mechanisms underlying their manifestation.

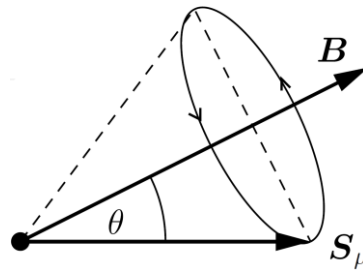


**Fig. 2.2.3** The muon spin,  $S_\mu$ , precesses around the field,  $B$ , with angular frequency of  $\omega_\mu = \gamma_\mu B$ . Reproduced from Ref. 20.

Upon implantation into a sample, muons undergo spin precession around the local magnetic field,  $B$ , with Larmor precession frequency  $\omega_\mu = \gamma_\mu B$  dictated by the muon gyromagnetic ratio,  $\gamma_\mu = 2\pi \times 135.5 \text{ MHz T}^{-1}$ . In a static magnetic field, the polarisation along the z-axis is governed by:

$$P_z(t) = \cos^2\theta + \sin^2\theta \cos(\gamma_\mu B t)$$

where  $B$  and  $t$  denote the strength of the magnetic field and time, respectively. If the magnetic field aligns along the z-axis, muons do not precess ( $\theta = 0$ ), resulting in 100 % retention of polarisation. Upon application of a transverse field ( $\theta = \pi/2$ ), the muons precess, causing a polarisation oscillation between

$\pm 1$ . In a sample with random magnetic fields in all directions, averaging over all angles yields  $\cos^2\theta = 1/3$  and  $\sin^2\theta = 2/3$ , leading to:

$$P_z(t) = \frac{1}{3} + \frac{2}{3} \cos(\gamma_\mu B t)$$

Most systems, however, are more complex, with magnetic fields exhibiting some form of distribution. A typical scenario arises when a muon, stopped in electrostatic equilibrium, experiences randomly oriented dipolar fields from neighbouring electrons and nuclei, with zero average. In cases where there is a relatively high concentration of dipolar fields, the distribution is Gaussian; whilst situations where the concentration of dipolar fields is dilute leads to a Lorentzian distribution. These are known as the Gaussian and the Lorentzian Kubo-Toyabe functions:

$$P_z^G(t) = \frac{1}{3} + \frac{2}{3} (1 - \Delta^2 t^2) e^{-\frac{\Delta^2 t^2}{2}}$$

$$P_z^L(t) = \frac{1}{3} + \frac{2}{3} (1 - at) e^{-at}$$

where  $\Delta$  and  $a$  denote the width and the rate of decay of the field distribution function at the muon site, respectively. These functions are further simplified for the fitting of the experimental data such that:

$$P_z^G(t) = \exp(-\Delta^2 t^2)$$

$$P_z^L(t) = \exp(-at)$$

Through a combination of TF, LF and ZF experiments, properly fitted to the appropriate relaxation functions, valuable insights into the internal fields surrounding the muon stopping sites within a sample can be obtained.

## 2.2.5 Muon Sources & Instrumentation<sup>21,23,24</sup>

The Muon Spin Relaxation experiments were performed on the on the EMU and GPD instruments at the ISIS Neutron & Muon Source (Rutherford Appleton Laboratory, Harwell, UK) and the Paul Scherrer Institut (PSI, Villigen, Switzerland), respectively. The former is a pulsed muon source, whilst the latter operates as a quasi-continuous source; some of the key aspects in relation to these modes of operation are outlined below.

Pulsed muon sources operate by injecting a cluster of muons into the sample at time  $t_0$ , with a specified pulse width and a predetermined interval between the pulses; with the latter normally longer than the lifetime of the muon. This configuration, coupled with negligible background between pulses, enables

the detection of incredibly small magnetic moments. With a detectable angle of 0.5 rad and the measurement extending up to 15  $\mu\text{s}$ , it is possible to detect local fields down to 0.04 mT, comparable to the dipolar contribution from a nuclear magnetic moment at typical atomic distances; and around  $10^{-3}$  smaller than a similar field induced by an electronic moment. However, the finite pulse width of the implanted muon ensemble imposes limitations on the time resolution. At ISIS, a pulse width of 60 ns renders the technique insufficient for systems exhibiting fast relaxation processes exceeding 10 MHz, or local fields exceeding 50 mT.

Continuous sources, on the other hand, require the instruments to treat each event individually. Upon entry, every muon is detected by a thin scintillation detector, initiating timing which is then halted upon emission and detection of a positron. Accumulating a significant number of such events ( $10^7$ , typically) results in a histogram of intensity versus time. To prevent mixing, the data collection pauses for a few muon lifetimes if a second muon enters before the decay of the previous one; imposing specific requirements on the rate of muon introduction into the setup for optimal operation. Furthermore, in this operation, events can be vetoed using logical coincidence electronics, i.e., should a muon bypass the sample and its holder, it may be detected and discarded by the forward and backward detectors simultaneously. This both reduces the background and allows for smaller sample sizes. The experimental time resolution is also enhanced since the continuous beam enables the precise knowledge of the implantation time of each muon, enabling the measurement of Larmor precession frequencies up to  $\sim 400$  MHz. Nonetheless, the significantly larger background limits the observation of slow processes and complicates the extraction of the polarisation function due to the requirement of additional background parameters.

### **2.2.5.1 The EMU Spectrometer**<sup>23</sup>

The EMU beamline is optimised for Zero and Longitudinal Field (ZF & LF) measurements. The spectrometer is equipped with 96 detectors, each composed of a scintillator, a light guide and a photomultiplier tube (PMT). The detectors are positioned in two opposing banks (forward and backward) around the sample location; individual banks consist of three concentric rings, each containing 16 detectors. The spectrometer allows for adjustable time resolution of 8, 16, 24 or 32 ns; longitudinal fields up to 4000 Gauss; and can measure frequencies in the 0.1 – 10 MHz range, with the upper limit determined by the finite width of the muon pulse.

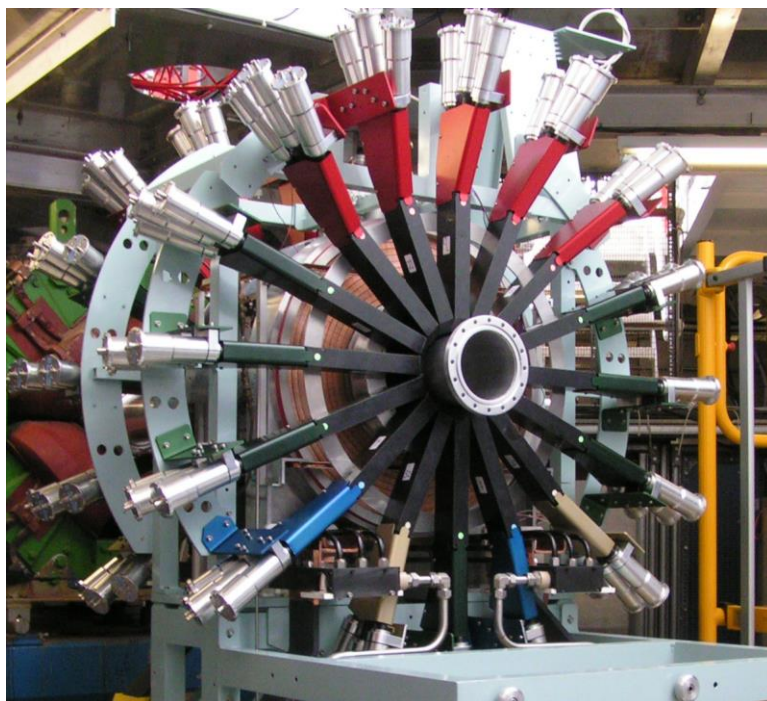


**Fig. 2.2.4. The EMU Spectrometer at the ISIS Neutron & Muon Source. Reproduced from Ref. 23.**

### **2.2.5.2 The GPS Spectrometer<sup>24</sup>**

The General Purpose Surface-Muon (GPS) spectrometer using a 'surface muon beam' by producing muons from the decay of positive pions stopped near the surface of the production target. The muons can typically penetrate approximately 1.5 mm in polyethylene and 0.65 mm in aluminium. The beamline is fitted with an electromagnetic separator and has the capacity to rotate muon-spin direction with relative to its momentum. The instrument is designed to conduct zero field, longitudinal field and transverse field experiments across a wide range of temperatures and magnetic fields. The spectrometer comprises six detectors (forward, backward and pairs of up and down) with a time resolution of 1 ns. The magnet can apply fields of up to 6600 Gauss with the orientation adjustable depending on the geometry of the experiment.

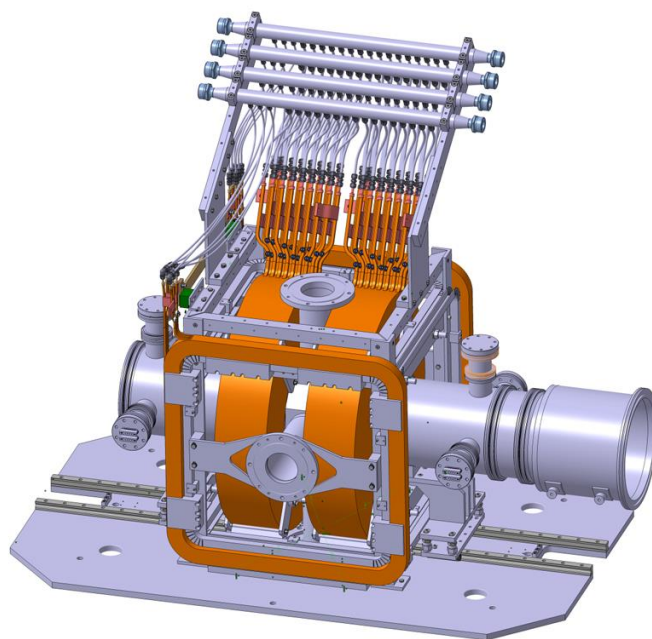


**Fig. 2.2.5. Schematic of the GPS Spectrometer at the Paul Scherrer Institut, Villigen, Switzerland. Reproduced from Ref. 24.**

### **2.2.5.3 $\mu$ SR Experimental Procedure**

Samples were prepared in an argon-filled glovebox, to prevent contamination from air, where they were loaded into silver foil packets ( $\sim 1 \times 1$  cm) and secured using silicone grease (for analysis on the GPS instrument); or loaded into aluminium sample holders and secured using silicone grease and a silver plate, screwed into the sample holder (for experiments on the EMU spectrometer). For the  $\mu$ SR measurement, the sample is attached to a sample stage; is inserted into the spectrometer; and is finally evacuated and purged using He gas to eliminate air and prevent ice formation. The sample environment features a CCR and a hot plate which were employed for temperature control (in the 9 – 300 K range) during the measurements. Each sample was initially subjected to a 20 Gauss TF to obtain instrumental calibration.

## **2.3 Materials & Characterisation**

This section details the techniques, instrumentation and experimental methodologies employed for the synthesis of the prototype methane-to-methanol conversion catalysts and the subsequent characterisation methods used to analyse these materials. These steps are crucial for the interpretation

of the results obtained from the neutron scattering and muon spin relaxation studies, which aim to elucidate the dynamics of various species within these materials.

### **2.3.1 Copper Loading**

Commercial grade, ammonium precursors of mordenite and ZSM-5, with Si/Al ratios of 10 and 15, respectively, were acquired from Alfa Aesar; while the protonic form of zeolite SSZ-13, with Si/Al ratio of 12, was generously supplied by Johnson Matthey. The ammonium precursors were calcined in order to prepare the protonic forms of mordenite (H-MOR) and ZSM-5 (H-ZSM-5). The calcination process involved heating the samples, in air, to 823 K at a rate of 1 K/min; holding for 8 hours; and subsequently cooling to room temperature.

Following calcination, the three protonic zeolites were subjected to liquid ion exchange by immersing each zeolite in a solution containing 0.1 M  $\text{Cu}(\text{NO}_3)_2$  and continuously stirring for 24 hours at room temperature. The zeolites were then washed with deionised water and resuspended in a fresh solution of 0.1 M  $\text{Cu}(\text{NO}_3)_2$ . This process was repeated three times in order to maximise the uptake of copper ions by the zeolites. The separation of the solid zeolite from the liquid solution or deionised water was facilitated by decanting the samples into test tubes and centrifuging at 4000 RPM. After the final washing stage, the samples were dried in an oven, at 353 K. The dry samples were subsequently sieved to a particle size of 75 – 150  $\mu\text{m}$ . Finally, the Cu-zeolites were activated by heating to 723 K at a rate of 1 K/min, holding for 4 hours and cooling to room temperature.

### **2.3.2 Brunauer-Emmett-Teller (BET) Surface Area Analysis**<sup>25</sup>

The specific surface area (SSA) is a parameter influencing the properties and performance of materials, as both particle and pore size can profoundly affect their behaviour. The specific surface area of a given sample is given by:

$$SSA = \frac{SA}{M}$$

Where  $SA$  and  $M$  denote total surface area and the mass of the sample, respectively. The volume specific surface area (VSSA, in  $\text{m}^2 \text{cm}^{-3}$ ) is defined as:

$$VSSA = \frac{SA}{V} = SSA \times \rho$$

Here,  $V$  represents the total volume of particles in the sample and the density value,  $\rho$  (in  $\text{g cm}^{-3}$ ), corresponds to the average density of the 'relevant' phase. The Brunauer-Emmett-Teller (BET) method is a commonly employed technique for the assessment of the specific surface area, pore volume and average pore diameter within materials in solid-state. The model is a two-parameter adsorption isotherm which describes the relationship between the amount of gas adsorbed and the pressure,  $p$ , in equilibrium with the gas phase, maintaining a constant temperature. The model has the following form:

$$\frac{p}{\sigma[p_0 - p]} = \frac{c - 1}{\sigma_0 c} \times \left(\frac{p}{p_0}\right) + \frac{1}{\sigma_0 c}$$

Here,  $\sigma$  is the surface coverage denoting the number of adsorbed molecules per unit area (or per  $\text{cm}^2$ );  $\sigma_0$  indicates the quantity of gas adsorbed in a monolayer, also expressed in molecules per unit area (or per  $\text{cm}^2$ ); and  $p_0$  is the saturation pressure of adsorbate gas which represents the point at which an infinite number of layers can be formed on the surface. The BET constant,  $c$ , is given by:

$$c \approx e^{(\Delta H_{ads} - \Delta H_{cond})}$$

Where  $\Delta H_{ads}$  and  $\Delta H_{cond}$  are heat of adsorption of the first layer and heat of condensation of the vapour, respectively. The BET model, however, is based on assumptions that the adsorption surface is uniform throughout; the heat adsorption remains constant regardless of surface coverage; there is no interaction between gas molecules adsorbed within the same layer; infinite layer adsorption is achievable; multilayer adsorption is regulated by Van der Waals interactions among the separate layers; and the energy released by multilayer adsorption matches the heat of condensation.

### **2.3.2.1 BET Experimental Procedure**

The BET surface area analysis was carried out by Dr Alice Oakley at the University of Southampton.  $\text{N}_2$  physisorption measurements were performed using a Micromeritics Gemini 2375 surface area and porosity analyser at liquid nitrogen temperature. Samples were degassed under a vacuum, at  $120^\circ\text{C}$ , overnight. Surface area measurements were determined using the Brunauer,

Emmett and Teller (BET) model; BET isotherms were obtained from 153 unique data points.

### 2.3.3 Diffraction<sup>26</sup>

The elementary principles of scattering outlined in Section 2.1.1 have detailed the interactions between radiation and matter. Diffraction is characterised by elastic scattering, where the energies of both the incident radiation and the scattering system are preserved. When the wavelength of the incident radiation is comparable to the spacing between lattice planes in a sample, constructive and destructive interference occurs, as a function of the angle of incidence, resulting in a distinct diffraction pattern. Said pattern encompasses both Bragg scattering from ordered planes or atoms and diffuse scattering from disordered regions in the material, enabling elucidation of structural information about the phases present within the sample. The diffraction process in crystalline solids is described by Bragg's law, which is expressed as:

$$\lambda = 2d \sin \theta$$

Where  $\lambda$  is the wavelength of the incident radiation,  $d$  is the distance between adjacent atomic planes and  $2\theta$  is the angle formed between the incident and the scattered beams. Within the scope of powder diffraction, an optimal powder sample consists of numerous randomly oriented crystallites, affording reproducible diffraction patterns. Thus, provided that the crystallite size is small (typically on the micro-scale) and the incident radiation can diffract from the material without significant absorption, diffraction can be applied to study a diverse range of samples including metals, ceramics, polymers, glasses and even liquids. Notably, a diffraction pattern obtained from a powder sample offers insights into the average structure of all crystallites within the sample; the derived structure consequently represents the average structure of the material.

#### 2.3.3.1 Neutron Diffraction

Neutron diffraction leverages neutrons' interactions with atomic nuclei, therefore the scattering characteristics do not uniformly increase with the atomic (Z) number and the variation in scattering lengths is significantly smaller than that observed in X-ray scattering. This renders neutron diffraction advantageous in studying materials containing light elements

alongside heavier ones, or those containing elements with a similar atomic number such as transition metals. Moreover, certain nuclei, such as vanadium, exhibit low scattering lengths, enabling construction of sample environments without introducing unfavourable features or signal interference.

Since the wavelength of a neutron is related to its mass and velocity, Bragg's law for a neutron can be defined as:

$$n \frac{ht}{mL} = 2d \sin \theta$$

where  $m$  is the mass of the neutron and  $h$  is Planck's constant; whilst  $L$  and  $t$  denote the total flight path and the time of flight, respectively.

The neutron diffraction experiments were carried out on the ENGIN-X time-of-flight neutron diffractometer at the ISIS Neutron & Muon Source. The instrument receives neutrons from a liquid methane moderator, held at 100 K, with primary (moderator to sample) and secondary (sample to detector) flight paths of 50 and 1.5 m, respectively. The frequency of the neutron pulses is adjustable between 5 and 50 Hz and the minimum attainable wavelength is approximately 0.5 Å. Details of the experimental procedure will be provided, alongside the relevant results, in Chapter 4.

### **2.3.3.2 X-Ray Diffraction**

Powder X-ray diffraction was carried out at the ISIS Materials Characterisation Laboratory on a Rigaku Miniflex benchtop X-ray diffractometer which features a 600 W Cu K $\alpha$  anode ( $\lambda = 1.5459$  Å) and a 6-position sample stage. The instrument operates using a filament which emits electrons that bombard the anode, resulting in the ejection of inner-shell electrons; with photons generated as a result of electrons filling the vacancies. The X-ray beam is collimated and directed onto the sample which, along with the detector, is rotated at predetermined angles to record the scattered beam at known  $2\theta$  values. The scans were performed in the  $0.02^\circ \leq 2\theta \leq 90^\circ$  range at  $1^\circ/\text{min}$ .

### **2.3.4 Diffuse Reflectance Infrared Fourier-transform Spectroscopy (DRIFTS)<sup>27</sup>**

Fourier transform spectroscopy relies on an interferometer to break down light into its individual components, with the Michelson interferometer central to

this process. In this setup, a polychromatic light from an infrared (IR) source is directed onto a beam splitter, which divides light into two separate beams: one beam travels toward a stationary mirror; the other is directed towards a moving mirror. After reflecting of both mirrors, the beams are recombined and directed toward the sample. Upon reaching the sample, the light may be absorbed, transmitted, reflected or scattered; the detector then collects the light that has interacted with the sample. The moving mirror oscillates back and forth over a known distance, altering the path length of the reflected beam. This variation causes the intensity of the recombined beam to fluctuate due to constructive and destructive interference, producing an interferogram. This interferogram, which is a sinusoidal signal that varies with the optical path difference (measured in millimetres), is then subjected to a Fourier transform to generate the IR spectrum.

In diffuse reflectance infrared Fourier transform spectroscopy (DRIFTS), the light reflected from the sample is what is captured by the detector, which then generates the interferogram. DRIFTS is particularly useful for analysing strongly absorbing samples. In diffuse reflectance, the IR beam penetrates the sample particles and scatters in multiple directions. The beam can also reflect off the particles' surfaces without penetrating, with multiple reflections occurring between particles. The scattered IR light is then focused by the mirror arrays within an accessory attached to the spectrometer, which directs it into the detector.

#### **2.3.4.1 DRIFTS Experimental Procedure**

The DRIFTS spectra were obtained using an Agilent Cary 680 FTIR spectrometer. The setup comprised a Harrick Praying Mantis beam accessory and a heated sample cell which enables a flow of gas through the sample environment. Inert gas (He or Ar) was used for purging the cell and transporting reagents (such as methane and water). The spectra were collected over the range of 4000 to 700  $\text{cm}^{-1}$  using a liquid nitrogen cooled MCT detector, with a resolution of 4  $\text{cm}^{-1}$ , and each spectrum was averaged over 64 scans.

### **2.3.5 Solid State Nuclear Magnetic Resonance (ssNMR)<sup>28</sup>**

Solid-state nuclear magnetic resonance (ssNMR) spectroscopy is a widely employed technique for characterising zeolite catalysts. Operating on the

principle of spin interactions between nuclei and a static magnetic field, NMR provides insights into molecular structure and dynamics within solid materials. In order for a molecule to exhibit activity in NMR, it must possess a non-zero spin quantum number, typically determined by the composition of the nucleus – specifically, an odd number of protons and neutrons. Upon exposure to a magnetic field, the Zeeman effect induces non-degenerate energy spin states, with the degree of separation influenced by the strength of the magnetic field and the nuclear interactions.

NMR spectra in solid materials are affected by several interactions including chemical shift anisotropy; spin-spin interactions (both direct and indirect, termed J-coupling); and quadrupolar interactions. J-coupling, arising from nuclei connected by bonds within a molecule, tends to be weak in solids, whereas dipole-dipole interactions, occurring between adjacent nuclei, are more pronounced due to fixed atomic positions, leading to spectral broadening. Quadrupolar interactions, involving nuclei with spins greater than  $\frac{1}{2}$ , contribute to peak broadening via interactions with electric field gradients.

Consequently, various techniques can be employed to address these challenges. Chemical shift anisotropy and spin-spin interactions can be mitigated by magic angle spinning (MAS) NMR which spins the sample at a specific angle, typically at  $54.7^\circ$ . This rotation effectively averages out the anisotropy, thus enhancing spectral resolution. Unwanted nuclear interactions can be eliminated via decoupling experiments, whereby a frequency which cancels the resonance frequencies of undesirable nuclei is applied. Moreover, signals from nuclei low in abundance can be enhanced by coupling them with more abundant nuclei, which is known as cross-polarisation.

### **2.3.5.1 ssNMR Experimental Procedure**

The ssNMR experiments and the subsequent data analysis were carried out by Dr Alice Oakley at the University of Southampton. Solid state magic angle spinning (ss-MAS) NMR was collected using an Agilent 600 MHz DD2 narrow bore magnet spectrometer. Samples were analysed in 3.2 mm zirconium oxide rotors with Vespel® caps. Direct acquisition of  $^{27}\text{Al}$  was carried out using a triple resonance probe tuned to  $^1\text{H}/^{27}\text{Al}/^{31}\text{P}$ . A 14 kHz spin rate was used, with 1280 scans for acquisition. The chemical shift axis for  $^{27}\text{Al}$  was calibrated using 1M  $\text{Al}(\text{NO}_2)_3$  aqueous solution (0 ppm). NMR data was processed and phased using Mnova 11.0 software by Mestrelab Research. The NMR data was subsequently normalised to the total sample mass within the rotor by dividing

the intensity values by total sample mass. NMR signal integration was carried out using the inbuilt integration tool within Origin® 2022b software in the region of 25 - 75 ppm.

### **2.3.6 Magnetisation Measurements**<sup>29</sup>

A magnetic properties measurement system (MPMS) comprises a small sample probe, submerged in a liquid helium bath and blanketed by liquid nitrogen; superconducting detection coils wherein the sample is manipulated; and a superconducting quantum interference device (SQUID). The SQUID is an incredibly accurate sensor used for the detection of magnetic fields and its operation is based on the principles of superconductivity and the Josephson effect; hence, it consists of a small ring of superconducting material with two Josephson junctions. Within the MPMS system, the SQUID operates as an exceptionally sensitive current-to-voltage converter, rather than directly measuring sample magnetisation. To measure the latter, a sample is mounted on a non-magnetic holder and fixed to a transport rod where it is subsequently inserted into the sample environment. The transport rod is connected to a motor which drives the sample to move vertically in discrete steps, typically divided into 32 points over a 4 cm length, through the detection coils. The current induced in the coils is then coupled inductively to the SQUID sensor, with the latter functioning as a highly linear current-to-voltage converter; the SQUID's output voltage consequently corresponds directly to the magnetisation of the sample. As the sample is expected to exhibit the ideal dipole behaviour, it must be considerably smaller than the detection coils to ensure the sample's magnetic field is limited to a small region around it and the subsequent interaction with the detection coils is uniform. To accurately determine the sample magnetisation, the system is calibrated using a sample of known magnetic susceptibility, such as palladium.

The experimental voltage response is then fitted as a function of sample position in order to determine the magnitude of the dipole moment ( $\gamma$ ); and the raw magnetisation, given in electromagnetic units (emu), is subsequently converted to CGS units ( $M_{\text{CGS}} = \text{emu cm}^{-3}$ ) via normalisation by the sample volume, followed by a conversion to SI units ( $\text{A m}^{-1}$ ) via the relation  $M_{\text{SI}} = 10^3 M_{\text{CGS}}$ . Lastly, the magnetic susceptibility,  $\chi$ , which is dimensionless and equal to the ratio of magnetisation to applied field ( $\chi = M_{\text{SI}}/H_{\text{SI}}$ ) can be calculated. Again, the units of magnetic field, which are given in Gauss, must be converted to SI units via the relation  $H_{\text{SI}} = (10^3/4\pi) H_{\text{CGS}}$ .

The measurements of magnetisation were conducted on a Quantum Design Magnetic Properties Measurement System (MPMS) with a temperature range of 1.8 – 400 K and an applied field range of 0 – 7 T; the data analysis was carried out by Dr Adam Berlie.

### **2.3.7 Thermogravimetric Analysis (TGA)**<sup>30</sup>

Thermogravimetric analysis (TGA) is a thermal analysis technique utilised to deduce changes in the physical and/or chemical properties of materials. The measurements typically involve either monitoring of temperature-induced changes at a constant heating rate, or tracking the mass loss over time whilst maintaining a constant temperature. This method affords the examination of various physical phenomena such as vaporisation, desorption, decomposition or dehydration. Additionally, TGA enables the assessment of thermal stability by evaluating the resistance of samples to thermal decomposition or degradation.

The analysis was carried out on a TGA Q50 instrument and involves placing approximately 20 mg of sample – zeolites in the present study – on a platinum pan which is then moved, by an autosampler, into a furnace. Although batch analysis is possible by virtue of the incorporated autosampler, the samples were introduced into the system individually to minimise exposure to air, since zeolites readily capture moisture and/or other contaminants. The sample is subsequently subjected to a flow of gas alongside a temperature ramp (N<sub>2</sub> and 5 K min<sup>-1</sup> to 823 K, respectively, in the present study); with the resultant changes in mass with temperature recorded and displayed graphically. Analysis of desorption and/or combustion products is possible via incorporation of a detector, such as a mass spectrometer, however this setup was not utilised in the present study.

### **2.3.8 X-Ray Absorption Near Edge Fine Structure** **(XANES)**<sup>31</sup>

X-Ray Absorption Near Edge Fine Structure (XANES) is a technique used to study the local electronic and atomic structure of materials, offering insights into the oxidation state and the local structure of the element under investigation. By finely-tuning the X-Rays to traverse a spectrum of energies near the absorption edge, specific to the element of interest, the sample absorbs

photons with ample energy to elevate an electron from the core to an empty state or continuum. In transmission mode, measuring photon intensity before and after the sample enables the observation of changes in absorption. The technique follows Beer's Law:

$$I = I_0 e^{-\mu t}$$

Where  $I_0$  and  $I$  denote the intensity of incident and transmitted X-Rays, respectively, whilst  $\mu$  is the absorption coefficient and  $t$  the sample thickness. Alternatively, some of the excited core electrons may return to their ground state by emitting fluorescent X-Rays characteristic of the element undergoing the transition. In this fluorescence mode, the emitted X-Rays are detected using a fluorescence detector positioned at an appropriate angle relative to the sample.

XANES spans the spectral range from the edge to approximately 50 eV beyond it, offering insights into the electronic properties, oxidation state and coordination geometry of samples. In the present study, the XANES region was utilised as a distinctive identifier against reference compounds to ascertain the oxidation state of copper within the sample. The experiments were conducted on the B18 general purpose XAS beamline at the Diamond Light Source synchrotron facility, through the block allocated group access granted to the UK Catalysis Hub. The samples were analysed *ex situ* and were either prepared as pellets or packaged within quartz capillaries.

### 2.3.9 X-Ray Fluorescence (XRF)<sup>32</sup>

X-Ray Fluorescence (XRF) spectroscopy operates by utilising X-Rays to induce ionisation in the inner shells of atoms within a sample. The ionisation occurs when the energy of a photon matches – or exceeds – the binding energy of an electron. High-energy photons prompt the ejection of inner shell electrons, resulting in the creation of vacancies which induce instability, leading to transfer of electrons from outer to the inner shells.

The transition of electrons to these vacancies gives rise to the emission of characteristic fluorescent radiation. This radiation occurs following the ejection of an inner orbital electron from an excited atom and subsequent transitions of atomic orbital electrons from high to low energy states. Each element emits secondary X-Rays with unique energies, categorised as K lines for transitions ending in the first shell; L lines for transitions to the second shell; and so on. The characteristic X-Ray photons are widely documented in the literature, and the fluorescent X-Ray radiation detected from the analysed

sample is a cumulative result of emissions from all elements present within the sample.

XRF has served as a valuable tool for elemental analysis in this project, facilitating the determination of chemical compositions of the modified zeolites. The measurements were conducted at the ISIS Materials and Characterisation Laboratory on the Malvern PANalytical Epsilon 3 XL spectrometer equipped with an energy-dispersive detector which detects a broad range of elements simultaneously. The samples were analysed in powder form, utilising thin-film sample pots to ensure unimpeded access for the X-Ray beam to the material. The fluorescence spectra obtained were compared to reference spectra to extract the relative proportions of the elemental components present within the samples.

## **2.4 Activity Testing**

Prior to investigating the dynamics of species relevant to the partial oxidation of methane, the prepared prototype Cu-loaded zeolites were subjected to the methane-to-methanol conversion reaction. This was done to ensure that the materials were active and, therefore, representative of the catalysts commonly employed for this conversion. This section outlines the custom-built setup used for the reaction, including the specific conditions, and the method used for quantifying the methanol produced.

### **2.4.1 Reactor Setup**

The reactor was assembled from apparatus available at the UK Catalysis Hub and comprised of a small tube furnace, portable mass-flow controllers (MFCs) and an ESS EcoCat™ portable mass spectrometer (MS).

The reactor was configured to accommodate the simultaneous flow of three gases (Ar, O<sub>2</sub> & CH<sub>4</sub>) at ambient pressure. The reactor tube was constructed of stainless steel, 20 cm in length and an inner diameter of 6 mm, and was housed in a small tube-furnace. The inlet of the reactor tube contained a 3-way union, incorporating a septum, to allow manual injection of water (*vide infra*) into the gas stream. The gas inlets, MFCs and the reactor tube were all connected using 1/8" stainless steel lines and Swagelok® fittings; the outlet of the reactor tube had a dual connection to the vent as well as the portable MS for quantification of the products. The temperature of the reactor was controlled by an inbuild

thermocouple, whilst the temperature of the catalyst bed was monitored using a thermocouple, attached via the outlet of the reactor tube, in direct contact with the catalyst bed.

## 2.4.2 Conditions

Approximately 100 mg of Cu-zeolite was carefully loaded into the reaction tube; the catalyst bed was approximately 2 cm in length which was maintained in the centre of the tube using quartz wool plugs on either side. A flow of Ar gas was then introduced, and the MS signal monitored to ensure the system is leak-free. The methane-to-methanol conversion is then carried out in three stages comprising activation, reaction and extraction of products.

The zeolite was activated *in situ* by heating, at a rate of  $10\text{ }^{\circ}\text{C min}^{-1}$ , to  $450\text{ }^{\circ}\text{C}$ , holding for 1 hour and then cooling to  $200\text{ }^{\circ}\text{C}$ , all under a flow of oxygen. Once cooled, the catalyst was purged with argon for 30 min to remove any remnant  $\text{O}_2$  and prevent overoxidation in the next stage. Reaction was then carried out by flowing  $\text{CH}_4$  over the catalyst bed for 1 hour. The system was subsequently purged, with argon, for 30 min. The extraction of methanol was facilitated by manually injecting HPLC-grade water into the flow of argon. The MS signals were monitored, and water was injected until the signal for methanol was below the limit of quantification, defined here as signal-to-noise ratio of 3. All flowrates were maintained at 100 sccm and the gases were undiluted, i.e., 100 % Ar,  $\text{O}_2$  and  $\text{CH}_4$  were used.

Quantification of products was facilitated by calibrating the MS signal to known concentrations of methanol. This was achieved via 5 duplicate injections ( $0.1 - 0.5\text{ }\mu\text{L}$ ) of HPLC-grade methanol at extraction conditions, i.e., at  $200\text{ }^{\circ}\text{C}$  and a flow of Ar (100 % at 100 sccm), with the reactor tube empty. The resultant MS response was integrated, and linear regression analysis performed to ensure  $R^2 \geq 0.99$ .

## 2.4.3 Mass Spectrometry<sup>33</sup>

The methanol produced in the reaction was quantified using gas-phase ion analysis, utilising a quadrupole mass spectrometer operating under ultra-high vacuum conditions and housing essential components such as filaments, a quadrupole and an ion detector. A quadrupole mass spectrometer operates on the principle of mass-selective action generated by an alternating electric field

within a quadrupole mass filter (QMF). This field is characterised by hyperbolic potential distributions in two perpendicular directions (X,Y) which remains stable along the third direction (Z), enabling the precise mass selection of ions.

The QMF consists of four parallel metal rods arranged in a square or rectangular configuration. Each rod carries an alternating current (AC) and direct current (DC) voltage, generating a radiofrequency (RF) electric field. These fields stabilise or destabilise the paths of ions passing through, based on their mass and charge; i.e., the ion trajectory is determined by their interaction with these fields: smaller ions are influenced more heavily, gravitating towards negative poles, while larger ions pass through relatively unaffected. Hence, adjustments to these voltages allow for targeted mass selection within the quadrupole.

The scanning process, afforded by the chosen DC voltage range, allows for the sequential analysis of ions across a spectrum of  $m/z$  values. Those ions that successfully pass through the quadrupole, reach a Faraday detector, where their ion current, which is proportional to their concentration, is measured. A secondary electron multiplier (SEM) can also be used, which generates secondary electrons upon collision with ions or electrons. These secondary electrons are then multiplied, resulting in a significantly amplified signal.

A critical component of the MS is the ion source which typically uses electron-impact ionisation to generate ions from sample molecules. A heated filament emits electrons which ionise sample molecules upon collision. Different filament materials such as tungsten, thoria-coated iridium or rhenium offer varying stability and performance under different vacuum conditions.

## 2.5 Bibliography

- (1) Mitchell, P. C. H.; Parker, S. F.; Ramirez-Cuesta, A.; Tomkinson, J. *Vibrational Spectroscopy with Neutrons, with Applications in Chemistry, Biology, Materials Science and Catalysis*; 2005; Vol. 3.
- (2) Price, D. L.; Skold, K. Introduction to Neutron Scattering. *Methods in Experimental Physics* 1986, 23 (PA). [https://doi.org/10.1016/S0076-695X\(08\)60554-2](https://doi.org/10.1016/S0076-695X(08)60554-2).
- (3) Redfern, S. Elementary Scattering Theory For X-Ray and Neutron Users, by D.S. Sivia. *Contemporary Physics* 2011, 52 (5). <https://doi.org/10.1080/00107514.2011.582162>.

- (4) Bée, M. *Quasielastic Neutron Scattering: Principles and Applications in Solid State Chemistry, Biology and Materials Science*; 1988.
- (5) Schulz, J. *ANSTO & OPAL Research Reactor Overview*.  
<https://ansn.iaea.org/Common/topics/OpenTopic.aspx?ID=13196>.
- (6) Thomason, J. W. G. The ISIS Spallation Neutron and Muon Source—The First Thirty-Three Years. *Nuclear Instruments and Methods in Physics Research, Section A: Accelerators, Spectrometers, Detectors and Associated Equipment* 2019, 917.  
<https://doi.org/10.1016/j.nima.2018.11.129>.
- (7) Albers, P. W.; Parker, S. F. Inelastic Incoherent Neutron Scattering in Catalysis Research. *Advances in Catalysis*. 2007.  
[https://doi.org/10.1016/S0360-0564\(06\)51003-X](https://doi.org/10.1016/S0360-0564(06)51003-X).
- (8) Parker, S. F.; Lennon, D.; Albers, P. W. Vibrational Spectroscopy with Neutrons: A Review of New Directions. *Applied Spectroscopy*. 2011.  
<https://doi.org/10.1366/11-06456>.
- (9) Parker, S. F.; Ramirez-Cuesta, A. J.; Daemen, L. Vibrational Spectroscopy with Neutrons: Recent Developments. *Spectrochimica Acta - Part A: Molecular and Biomolecular Spectroscopy* 2018, 190.  
<https://doi.org/10.1016/j.saa.2017.09.057>.
- (10) Parker, S. F.; Fernandez-Alonso, F.; Ramirez-Cuesta, A. J.; Tomkinson, J.; Rudic, S.; Pinna, R. S.; Gorini, G.; Fernández Castañón, J. Recent and Future Developments on TOSCA at ISIS. In *Journal of Physics: Conference Series*; 2014; Vol. 554. <https://doi.org/10.1088/1742-6596/554/1/012003>.
- (11) Perrichon, A. On the Spectral Resolution of the Broad-Band Indirect-Geometry Time-of-Flight Neutron Spectrometer TOSCA. *Nuclear Instruments and Methods in Physics Research, Section A: Accelerators, Spectrometers, Detectors and Associated Equipment* 2022, 1041.  
<https://doi.org/10.1016/j.nima.2022.167401>.
- (12) Arnold, O.; Bilheux, J. C.; Borreguero, J. M.; Buts, A.; Campbell, S. I.; Chapon, L.; Doucet, M.; Draper, N.; Ferraz Leal, R.; Gigg, M. A.; Lynch, V. E.; Markvardsen, A.; Mikkelsen, D. J.; Mikkelsen, R. L.; Miller, R.; Palmen, K.; Parker, P.; Passos, G.; Perring, T. G.; Peterson, P. F.; Ren, S.; Reuter, M. A.; Savici, A. T.; Taylor, J. W.; Taylor, R. J.; Tolchenov, R.; Zhou, W.; Zikovsky, J. Mantid - Data Analysis and Visualization Package for Neutron Scattering and  $\mu$  SR Experiments. *Nuclear Instruments and Methods in Physics Research, Section A:*

*Accelerators, Spectrometers, Detectors and Associated Equipment* 2014, 764.  
<https://doi.org/10.1016/j.nima.2014.07.029>.

- (13) Karlsson, M. Proton Dynamics in Oxides: Insight into the Mechanics of Proton Conduction from Quasielastic Neutron Scattering. *Physical Chemistry Chemical Physics* 2015, 17 (1).  
<https://doi.org/10.1039/c4cp04112g>.
- (14) Telling, M. T. F. *A Practical Guide to Quasi-Elastic Neutron Scattering*; Royal Society of Chemistry, 2020.
- (15) Fritzsche, H.; Huot, J.; Fruchart, D. *Neutron Scattering and Other Nuclear Techniques for Hydrogen in Materials*; 2016.
- (16) Van Hove, L. Correlations in Space and Time and Born Approximation Scattering in Systems of Interacting Particles. *Physical Review* 1954, 95 (1). <https://doi.org/10.1103/PhysRev.95.249>.
- (17) Molecular Spectroscopy Group, I. N. & M. S. *The IRIS User Guide 4 th Edition*. <https://www.isis.stfc.ac.uk/Pages/irisman.pdf>.
- (18) de Souza, N. R.; Klapproth, A.; Iles, G. N. EMU: High-Resolution Backscattering Spectrometer at ANSTO. *Neutron News* 2016, 27 (2).  
<https://doi.org/10.1080/10448632.2016.1163985>.
- (19) Australian Nuclear Science and Technology Organisation. *EMU Cold-neutron Backscattering Spectrometer User Manual*.  
<https://www.ansto.gov.au/media/5842/download?inline>.
- (20) Stephen J. Blundell, Roberto De Renzi, Tom Lancaster, and F. L. P. *Muon Spectroscopy: An Introduction*; Stephen J. Blundell, Roberto De Renzi, Tom Lancaster, and F. L. P., Ed.; Oxford University Press: Oxford, 2021.
- (21) Hillier, A. D.; Blundell, S. J.; McKenzie, I.; Umegaki, I.; Shu, L.; Wright, J. A.; Prokscha, T.; Bert, F.; Shimomura, K.; Berlie, A.; Alberto, H.; Watanabe, I. Muon Spin Spectroscopy. *Nature Reviews Methods Primers*. 2022. <https://doi.org/10.1038/s43586-021-00089-0>.
- (22) Carretta, P.; Lascialfari, A. *NMR-MRI, MSR and Mössbauer Spectroscopies in Molecular Magnets*; 2007. <https://doi.org/10.1007/978-88-470-0532-7>.
- (23) Giblin, S. R.; Cottrell, S. P.; King, P. J. C.; Tomlinson, S.; Jago, S. J. S.; Randall, L. J.; Roberts, M. J.; Norris, J.; Howarth, S.; Mutamba, Q. B.; Rhodes, N. J.; Akeroyd, F. A. Optimising a Muon Spectrometer for Measurements at the ISIS Pulsed Muon Source. *Nuclear Instruments and*

*Methods in Physics Research, Section A: Accelerators, Spectrometers, Detectors and Associated Equipment* 2014, 751.  
<https://doi.org/10.1016/j.nima.2014.03.010>.

- (24) Luetkens, A. A. & H. *GPS User Guide*. Laboratory for Muon Spectroscopy.  
[https://www.psi.ch/sites/default/files/import/smus/InstrumentGpsEN/User\\_Guide\\_present\\_version.pdf](https://www.psi.ch/sites/default/files/import/smus/InstrumentGpsEN/User_Guide_present_version.pdf).
- (25) Gibson, N.; Kuchenbecker, P.; Rasmussen, K.; Hodoroaba, V. D.; Rauscher, H. Volume-Specific Surface Area by Gas Adsorption Analysis with the BET Method. In *Characterization of Nanoparticles: Measurement Processes for Nanoparticles*; 2019.  
<https://doi.org/10.1016/B978-0-12-814182-3.00017-1>.
- (26) Goonetilleke, D.; Sharma, N. In Situ Neutron Powder Diffraction Studies. *Physical Sciences Reviews* 2019, 4 (6).  
<https://doi.org/10.1515/psr-2018-0155>.
- (27) Stuart, B. H. *Infrared Spectroscopy: Fundamentals and Applications*; 2005.  
<https://doi.org/10.1002/0470011149>.
- (28) Watanabe, S. "Solid-State NMR in Zeolite Catalysis." *Johnson Matthey Technology Review* 2020, 64 (2), 197–198.  
<https://doi.org/10.1595/205651320x1582541146190>.
- (29) Francombe, M. H.; I. Braginski, A.; Krause, H.-J.; Vrba, J. Chapter 6 – Squid Magnetometers. In *Handbook of Thin Film Devices*; 2000.
- (30) Parameshwaran, R.; Sarı, A.; Jalaiah, N.; Karunakaran, R. Applications of Thermal Analysis to the Study of Phase-Change Materials. In *Handbook of Thermal Analysis and Calorimetry*; 2018; Vol. 6.  
<https://doi.org/10.1016/B978-0-444-64062-8.00005-X>.
- (31) Hutchings, G.; Davidson, M.; Catlow, R.; Hardacre, C.; Turner, N.; Collier, P. *Modern Developments in Catalysis*; 2017.  
<https://doi.org/10.1142/q0035>.
- (32) Karathanasis, A. D.; Hajek, B. F. Elemental Analysis by X-Ray Fluorescence Spectroscopy. In *Methods of Soil Analysis, Part 3: Chemical Methods*; 2018. <https://doi.org/10.2136/sssabookser5.3.c7>.
- (33) Batey, J. H. The Physics and Technology of Quadrupole Mass Spectrometers. *Vacuum* 2014, 101.  
<https://doi.org/10.1016/j.vacuum.2013.05.005>.

Prior to investigating the dynamics of species relevant to the partial oxidation of methane within Cu-loaded mordenite, SSZ-13 and ZSM-5 zeolites, the efficacy of these materials, in terms of the methane-to-methanol conversion, was evaluated. This step ensured that the prepared zeolites accurately represented the catalysts commonly employed for this reaction. As such, the following chapter focusses on the activity of the three Cu-loaded zeolites towards this conversion, as well as their characterisation to elucidate the changes induced by this reaction.

### 3.1 Material Preparation

The zeolites mordenite, SSZ-13 and ZSM-5 were prepared and loaded with copper as per *Section 2.3.1* in Chapter 2. Powder X-ray diffraction (PXRD) patterns were obtained before and after copper impregnation (Fig. 3.1.1). No discernible alterations in the patterns were observed, indicating effective integration of Cu and the absence of any additional CuO outside the framework. The resultant Cu-loaded mordenite, SSZ-13 and ZSM-5 samples contained 2.93, 2.60 and 1.87 % Cu (w/w), respectively, determined via XRF analysis.

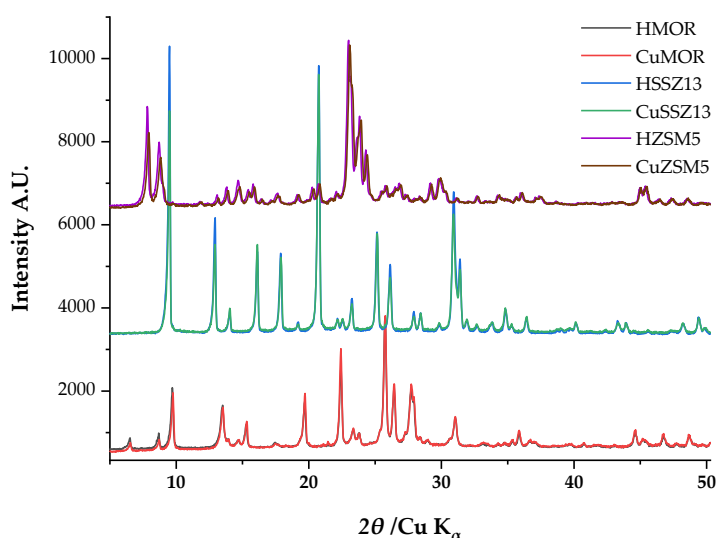


**Fig. 3.1.1** PXRD patterns of protonic and Cu-loaded zeolites.

## 3.2 Activity

The following section explores the methodologies employed to ascertain the activity of the Cu-loaded zeolites towards the partial oxidation of methane. This process towards establishing an effective method was not without its challenges, as various obstacles were encountered along the way. However, through persistent experimentation and refinement, an effective approach was ultimately developed which enabled the assessment of these materials' performance.

### 3.2.1 Hidden Catlab Microreactor

The initial stages of method development involved the use of the Hidden Catlab microreactor, consisting of a reactor, mass-flow controls and a mass spectrometer. This phase aimed to optimise crucial parameters such as sample size, gas compositions and flow rates in order to successfully carry out the methane-to-methanol conversion. Encouragingly, initial observations hinted at the desired reactivity, indicating the potential efficacy of the chosen materials and methods. However, this promising start was immediately met with a series of challenges that necessitated careful troubleshooting and adaptation. Foremost among these hurdles were persistent issues with pressure within the mass spectrometer, stemming primarily from the blockage of the capillary liner connecting the reactor with the mass spectrometer. This obstruction hindered the flow of gases between the two pieces of apparatus, requiring frequent interventions to rectify the issue via disassembly, cleaning and/or replacement of the liner, reassembly and testing of the apparatus to ensure a leak and contaminant-free system. Moreover, occurrence of blockages in the molecular leak within the mass spectrometer exacerbated the situation, demanding further down-time for disassembly, cleaning and/or replacement of parts, and subsequent reassembly and testing.

Despite successful troubleshooting and rectification of blockages, further issues persisted. Breakage of the inner reactor tube during the experimental runs caused leaks and further down-time for replacement of parts. Furthermore, issues arose with the positioning of the thermocouple within the reactor chamber, as its inadvertent contact with the reactor walls disrupted the temperature program's accuracy, introducing further complications. These collective challenges not only consumed significant amount of time and resources, but also hindered the acquisition of a robust dataset crucial for

meaningful analysis of the materials' activity. It became increasingly clear that a more adaptable and robust methodology was necessary to overcome these obstacles and enable the acquisition of reliable experimental results, essential for the determination of activity of these materials.

### 3.2.2 Multi-capillary Reactor

Following the challenges encountered with the Catlab microreactor, attention was shifted to a multi-capillary reactor custom-built for the B18 beamline at Diamond Light Source, designed for X-ray absorption spectroscopy (XAS) experiments. During sample preparation for the XANES measurements (*vide infra*), it was discovered that this setup successfully facilitated methane partial oxidation reactions. Consequently, this setup was utilised in order to attempt to acquire the necessary activity data for the three Cu-loaded zeolites. While initial results were promising, challenges swiftly arose, particularly with loading and securing the capillaries to maintain a sealed atmosphere. Despite progress, issues emerged with the heating cartridges of the reactor's heating block. This initially caused shorts and blown fuses in the fume hood used to house the reactor. Subsequently, some heating cartridges were found to be defective, impeding the attainment of the required temperature of 450 °C, essential for the material activation stage of the reaction. These setbacks added further delays to acquisition of reliable data as well as the calibration curves necessary for quantification. A new strategy was thus deemed necessary to address these technical challenges, ensure successful execution of experiments and, crucially, to attain the necessary activity data after significant time already invested to little avail.

### 3.2.3 DRIFTS

In an attempt to address the persistent challenges in analysing the activity of the three prototype methane-to-methanol (MTM) conversion catalysts, diffuse reflectance Fourier transform infrared spectroscopy (DRIFTS) was used with the aim to elucidate the surface species formed during the partial oxidation of methane. The spectra were acquired via 32 scans at a resolution of 4 cm<sup>-1</sup> and were collected after several stages: high-temperature oxygen activation, methane reaction, post-reaction; and after water injection for methanol desorption. Each zeolite sample underwent pretreatment in an *in situ* cell. The sample was heated, under a flow of oxygen, to 400 °C, held for one hour and

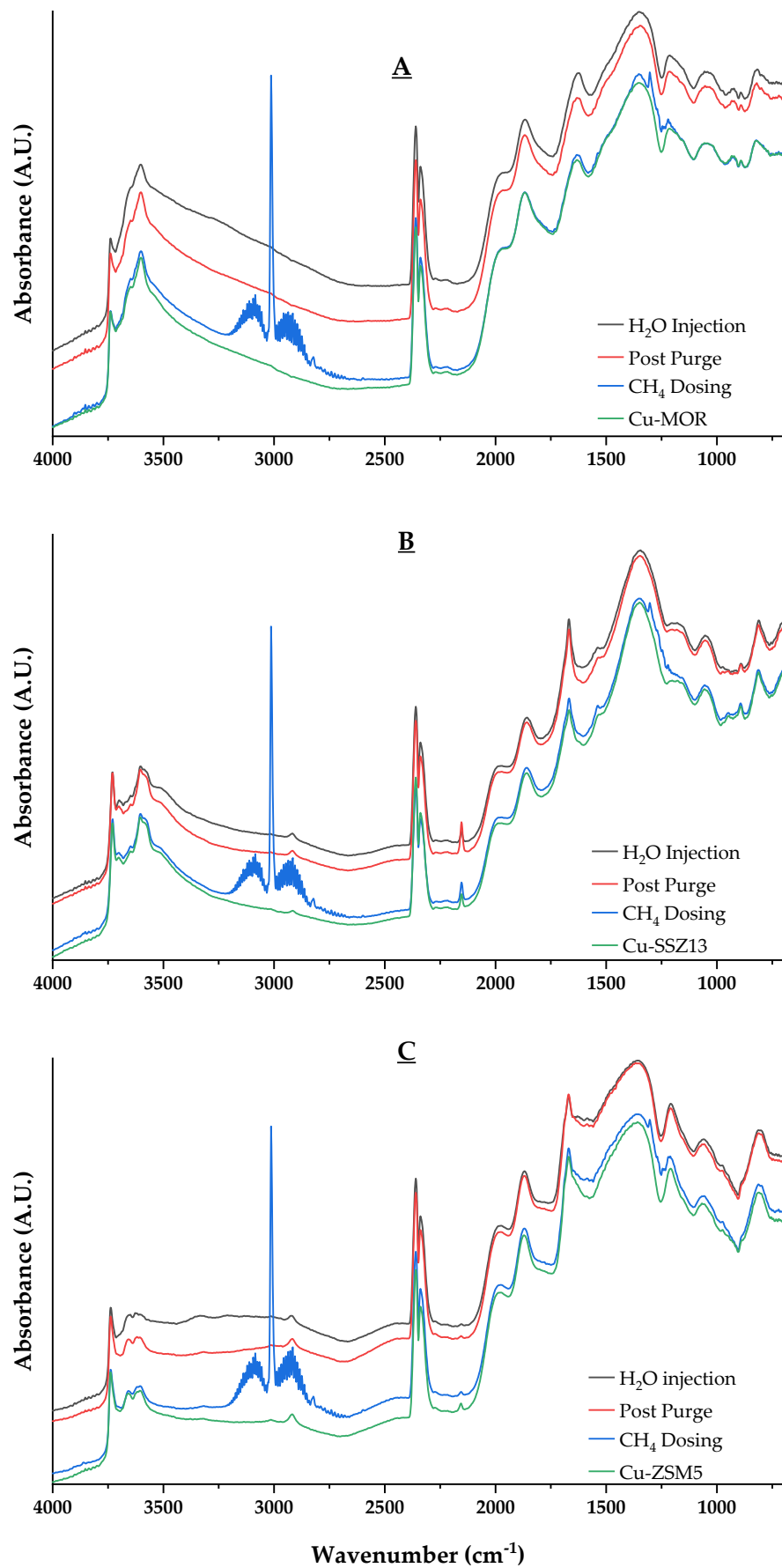


**Fig. 3.2.3 DRIFTS spectra obtained from CuMOR (A), CuSSZ13 (B) and CuZSM5 (C) during various stages of the methane-to-methanol conversion reaction.**

cooled to 200 °C. The system was then purged, with helium, for 30 minutes to remove any remnant O<sub>2</sub>. Methane (80% in He) was subsequently introduced into the system for 1 hour, followed by another 30-minute purge to remove gaseous and weakly-adsorbed methane. Finally, water was manually injected (5 µL) into the flow of helium to facilitate the desorption of methanol. All flowrates were maintained at 50 sccm (using mass flow controls) and a KBr background spectrum was recorded separately. The spectra were analysed after ratioing the background with the adsorbate spectra and are presented in Fig. 3.2.3.

In all cases, the region below 2000 cm<sup>-1</sup> is predominantly characterised by the zeolite framework modes, consisting of strong adsorbing bands attributed to the SiO<sub>4</sub> and AlO<sub>4</sub> units within the zeolite. Three distinct environments are visible in the region above 3500 cm<sup>-1</sup>, relating to the O-H stretch modes. Among these, the bands at ~3600 cm<sup>-1</sup> and ~3730 cm<sup>-1</sup> correspond to Brønsted acid sites within the zeolite and silanol (Si-O-H) groups terminating the zeolite framework on its outer surface, respectively; whilst the band at ~3650 cm<sup>-1</sup> is ascribed to extra-framework aluminium. Moreover, a doublet peak around ~2348 cm<sup>-1</sup>, arising from gaseous CO<sub>2</sub>, is also present in all three samples; whilst a weak band at 2155 cm<sup>-1</sup>, attributed to CO, is only present in the SSZ-13 and ZSM-5 samples. Occurrence of both CO and CO<sub>2</sub> is attributed to contamination, rather than methane oxidation, due to the presence of these bands prior to the introduction of methane into the system.

Upon introduction of methane (blue trace), an intense peak at ~3013 cm<sup>-1</sup> which corresponds to a ν<sub>3</sub> band and two broad bands at ~2920 and ~3075 cm<sup>-1</sup> become prominent in all samples and correspond to C-H stretching vibrations of gaseous methane; with the latter two bands containing fine vibration-rotation structures. A further band at ~1300 cm<sup>-1</sup> corresponds to the C-H bending vibrations of methane, again present in all three samples. The weak bands visible at 2596 and 2820 cm<sup>-1</sup> correspond to the overtone of the ν<sub>4</sub> bending vibration and from the ν<sub>2</sub> + ν<sub>4</sub> combination of bending vibrations, respectively. A sharp absorption band at 2153 cm<sup>-1</sup>, corresponding to Cu<sup>I</sup> monocarbonyl, is present within Cu-SSZ-13; the same band shows weak absorption on Cu-MOR and is absent in Cu-ZSM-5. This is in good agreement with the CO-adsorption experiments (*vide infra*) which show that a higher temperature (225 °C) is required to desorb the monocarbonyl species from Cu-SSZ-13 compared to the other two zeolites (145 °C).

After the final purging with helium, no surface species related to methane partial oxidation could be identified. The persistent presence of CO and CO<sub>2</sub> bands in the spectra, attributed to contamination, made it impossible to determine whether any CO or CO<sub>2</sub> have formed due to overoxidation of

methane. Furthermore, the increasing baseline observed in the spectra is likely due to the movement of the catalyst bed, which further complicates any meaningful analysis.

### 3.2.4 Custom Setup

Encountering the various aforementioned challenges caused the approach to the problem to be reassessed. It became evident that the requirements for the experiment – a well-controlled temperature program, precise mass flow controls and a reliable detector – were well within the capabilities of the equipment available separately in the laboratory. Although not integrated like the apparatus comprising the CatLab system, these essential components could be utilised in tandem to execute the reaction effectively. Thus, a custom-built reactor setup (outlined in *Section 2.4.1*) comprising a small tube furnace, portable mass-flow controllers and a portable mass spectrometer was assembled.

Upon establishing the adequacy of this setup for the demands of the experiment, the focus was shifted to method development aimed at determining the optimal parameters for flow rates, gas compositions and methanol desorption steps. This latter part required particular attention in order to determine whether the desorption of methanol can be facilitated via a steady stream of water by either multiple, timed injections (50  $\mu\text{L}$ ) or a single large injection (500  $\mu\text{L}$ ). Both of these attempts led to water condensation within the tubing as well as water saturation of the sample. This indicated that the desorption temperature of 200  $^{\circ}\text{C}$  was insufficient to rapidly vaporise such a large amount of water, leading to ineffective desorption. In response to this, the method was amended to employ smaller injections of water (5  $\mu\text{L}$ ) to enable effective vaporisation. A further precaution was implemented to mitigate the risk of condensation and ensure optimal desorption: after each injection, a deliberate waiting period was introduced to allow time for the elution process to occur effectively, which was monitored via the MS. This pause served the purpose of preventing the buildup of water within the system, thus minimising the potential for condensation and ensuring the successful removal of methanol from the sample. Additionally, the flowrates were adjusted and increased to 200 sccm to expedite desorption, as lower flowrates (100 sccm and below) resulted in each injection requiring over an hour to elute, unnecessarily prolonging the experimental process.

Successful method development allowed the ideal conditions to be deduced and for the experimental process to be streamlined. Utilising undiluted gases

proved effective and aided in simplification of the setup. Optimisation of flowrates was undertaken to achieve a balance between effective activation and reaction whilst minimising gas consumption and waste. Flowrates of 50 sccm were determined sufficient for both the activation and reaction steps, ensuring adequate gas supply while conserving resources. Higher flowrates of 200 sccm were employed during the purging and desorption stages to more efficiently remove any residual gases and facilitate the desorption process, respectively.

Consequently, the three samples were subjected to the methane partial oxidation reaction using this reactor setup and reaction conditions (also outlined in Sections 2.4.1 and 2.4.2, respectively). Each Cu-loaded zeolite was reacted five consecutive times in

**Table 3.1 Methanol produced during each of the five cycles of the reaction.**

Reaction Cycle	Methanol Produced ( $\mu\text{mol g}_{\text{cat}}^{-1}$ )		
	CuMOR	CuSSZ13	CuZSM5
1	17.80	8.38	5.11
2	18.62	10.78	6.41
3	18.07	11.52	6.07
4	18.84	9.17	5.94
5	18.26	10.51	5.85

order to check their activity over time. Calibration of the MS signal to known quantities of methanol was performed at the end of each of the five cycles using the procedure outlined in Section 2.4.2. An exemplar calibration curve is in Fig. 3.2.4. Examples of the MS response of methanol ( $m/z = 31$ ) obtained during one of the extraction stages is presented in Fig 3.2.5; and the methanol produced during each of the five cycles of the reaction is presented in Table 3.1.

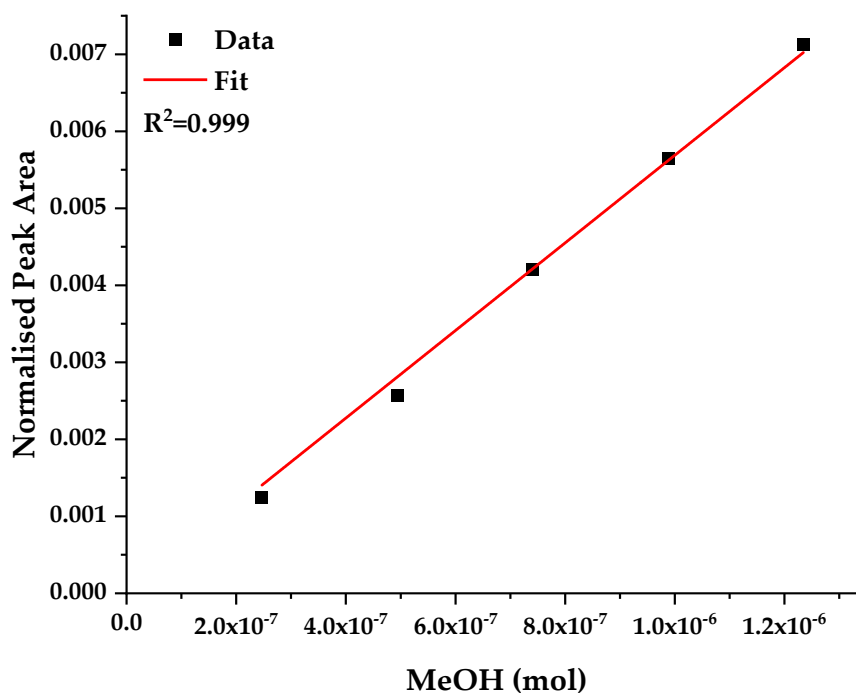


**Fig. 3.2.4 Exemplar calibration curve used to quantify the methanol produced after reaction with Cu-SSZ13.**

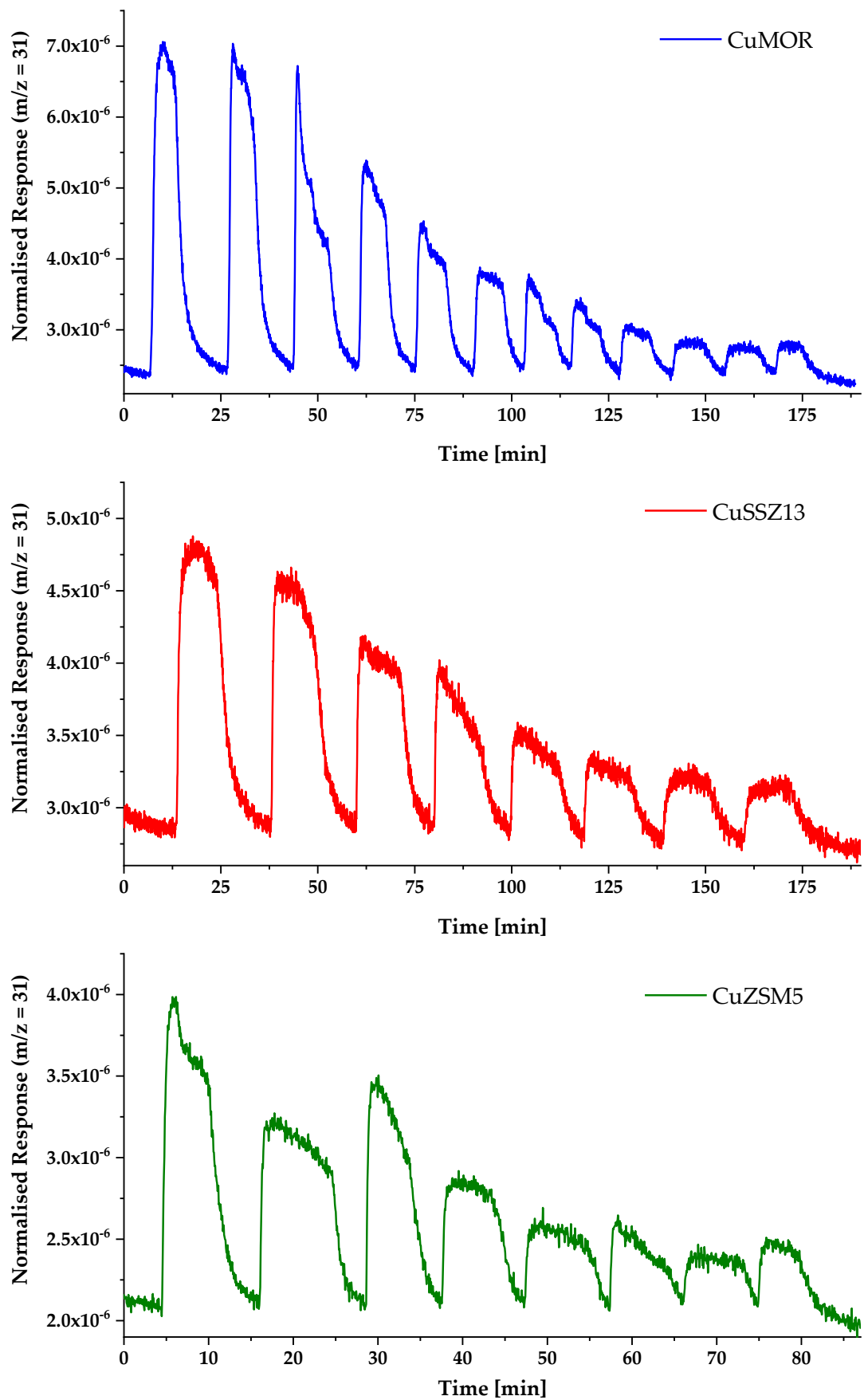
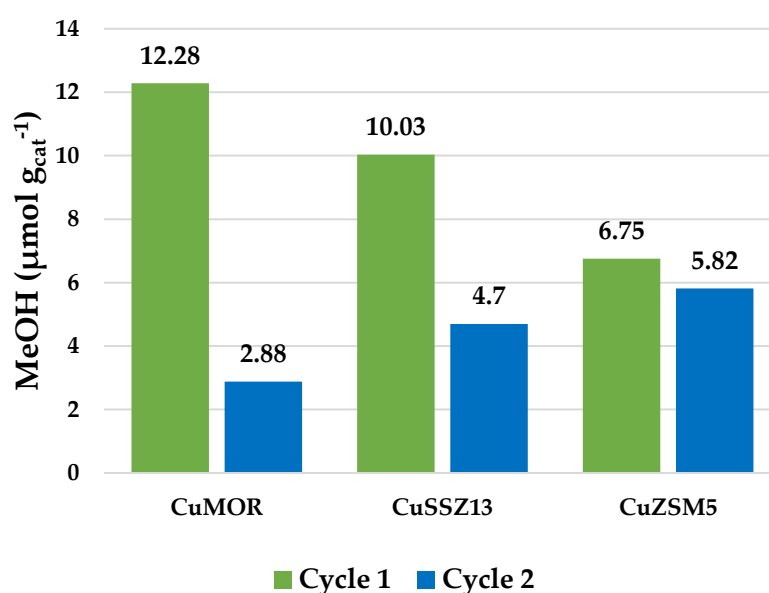


Fig. 3.2.5 Methanol response during the extraction stage of the first reaction cycle for each Cu-loaded zeolite.

All three samples were shown to be active towards the partial oxidation of methane but with significant variations in the methanol produced. Cu-MOR displayed the best performance with methanol produced at 17.80  $\mu\text{mol g}_{\text{cat}}^{-1}$  during the first cycle; whilst the methanol produced using Cu-ZSM-5 was over 70 % lower at 5.11  $\mu\text{mol g}_{\text{cat}}^{-1}$ . The activity of these materials corresponds well to their variation in Si/Al ratio and, in turn, the copper loading; i.e., a lower Si/Al ratio and higher copper loading result in higher activity towards methane-to-methanol conversion, which is expected since the copper active sites are responsible for methane activation. No significant decrease in methanol production over the five cycles of the reaction was observed. This suggests the materials are stable and no structural changes affecting methane conversion rate are occurring over the five cycles studied. The average methanol production over the five cycles was at 18.32, 10.07 and 5.88  $\mu\text{mol g}_{\text{cat}}^{-1}$ , in Cu-MOR, Cu-SSZ-13 and Cu-ZSM5, respectively.

Furthermore, the effects of water on the activity of the samples were investigated, since it has been reported that water may act as a soft oxidant<sup>1</sup>, thus eliminating the requirement for the high-temperature activation with molecular oxygen. The three samples were subjected to two cycles of the reaction without a high-temperature activation in between; i.e., at the end of the first reaction cycle, the sample was purged with inert gas followed by reaction with methane and subsequent extraction. The activity thus derived is presented in Fig. 3.2.6. A significant decrease in methanol production during the second cycle can be observed for both Cu-MOR and Cu-SSZ13 samples, at 76 % and 53 %, respectively. Interestingly, the effect within the ZSM-5 sample is much smaller with the activity decreasing by only 14%.



**Fig. 3.2.6 MeOH production rates with (green) and without (blue) high-temperature oxygen activation.**

Although the activity data does not provide an insight into the copper speciation within the samples (*vide infra*), it is clear that high-temperature activation with molecular oxygen is not intrinsically necessary for this conversion to take place. Indeed, use of water as the sole oxidant has been documented by Sushkevich *et al.*<sup>2</sup> albeit at an elevated pressure of 7 bars. The regime employed in this study, however, shows that omission of the activation step results in a significantly reduced activity, likely due to insufficient active site regeneration at ambient pressure.

Important to note is that the activity measured in the samples used in this study are an order of magnitude lower than some of the recent reports. For example, a study by Dyballa *et al.* documented methanol production up to 169  $\mu\text{mol g}_{\text{cat}}^{-1}$  within Cu-MOR after optimisation of both the material and the conditions.<sup>3</sup> In the present study, the primary objective was to investigate the dynamics of various species within these materials and, as such, optimisation of each of the three zeolites was omitted for ease of preparation of the materials in bulk for neutron studies.

### 3.3 Copper Speciation

#### 3.3.1 Cu Self-Reduction

A frequently encountered, yet poorly understood, phenomenon is the “autoreduction” or “self-reduction” occurring during the activation of Cu-exchanged zeolites. This process involves the spontaneous conversion of certain Cu(II) species to Cu(I) at elevated temperatures, typically above 673 K, within an inert environment, without the presence of a reducing agent.<sup>4-12</sup> In order to investigate the occurrence of autoreduction in the samples used for this study, diffuse reflectance Fourier-transform infrared spectroscopy (DRIFTS) was employed, utilising a CO probe to examine the presence of Cu(I) species after high-temperature activation under inert gas flow. The spectra were acquired via 32 scans at a resolution of 4  $\text{cm}^{-1}$ . Prior to measurement, each zeolite underwent pretreatment in an *in situ* cell. The sample was heated, under a flow of helium, to 400 °C, held for one hour and cooled to room temperature. A background spectrum was recorded and the sample was then dosed with CO (10% in He) for one hour. The cell was subsequently purged with a flow of He for 30 minutes to eliminate gaseous and weakly adsorbed CO. Initial spectra were captured at room temperature, followed by stepwise temperature increase in 20 °C increments, until all CO bands have diminished.

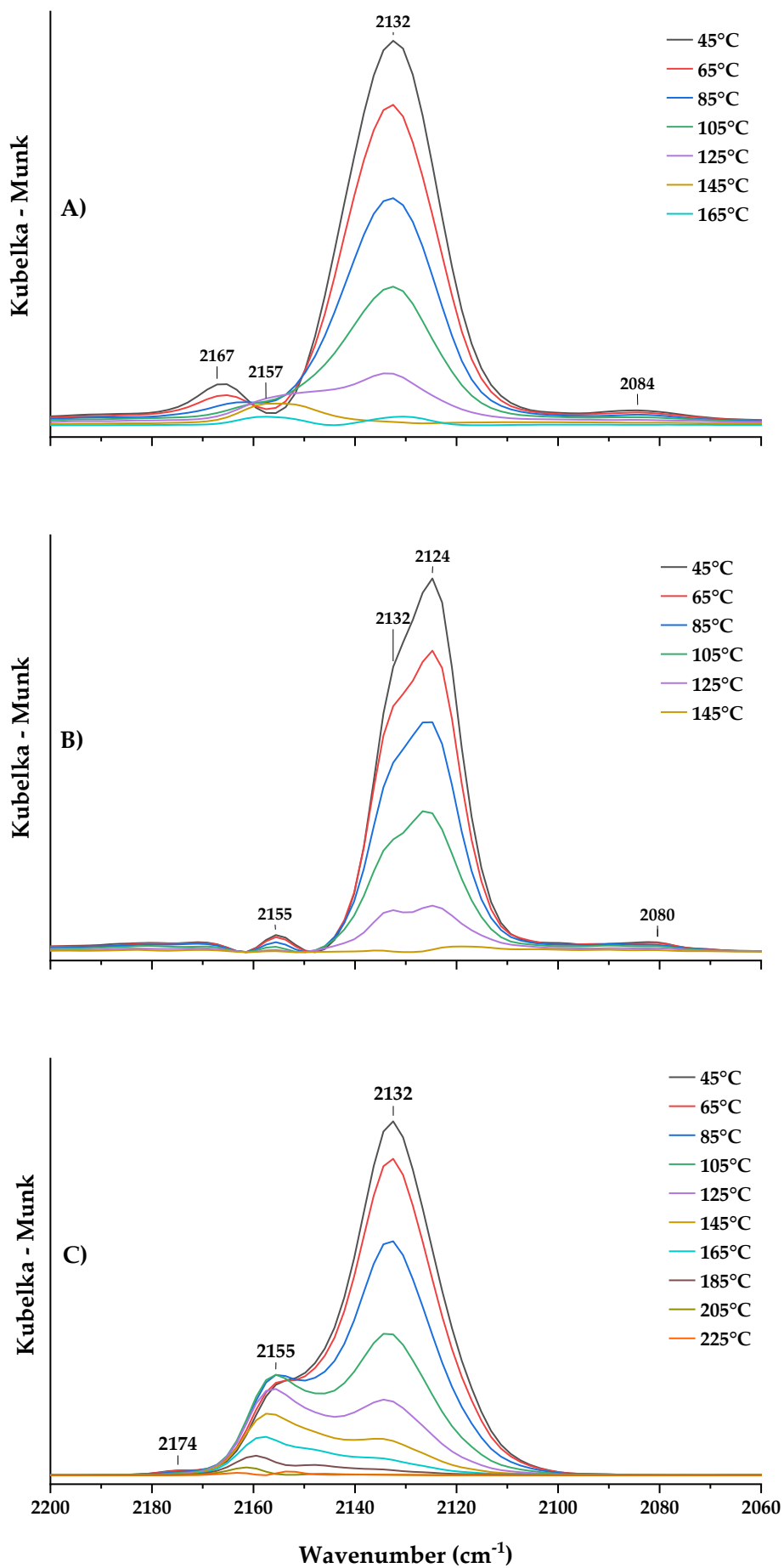


Fig. 3.3.1 Desorption of CO from Cu-MOR (A), Cu-ZSM-5 (B) and Cu-SSZ-13 (C).

Spectra were analysed after subtracting the background from the adsorbate spectra. Flows of helium and CO were maintained at 30 sccm using mass flow controls. The spectra acquired are presented in Fig 3.3.1.

Three distinct bands are evident in the spectra obtained from Cu-MOR. The band at  $2132\text{ cm}^{-1}$  corresponds to  $\text{Cu}^{\text{I}}\text{CO}$  monocarbonyl surface species. Bands at  $2157$  and  $2167\text{ cm}^{-1}$  are attributed to low- and high-frequency vibrations of  $\text{Cu}^{\text{I}}(\text{CO})_2$ , respectively, with the former being distinguishable only at  $125\text{ }^{\circ}\text{C}$ . A small band at  $2084\text{ cm}^{-1}$  may correspond to either  $\text{Cu}^{\text{I}}$  or  $\text{Cu}^{\text{0}}$  due to a  $30\text{ cm}^{-1}$  overlap of these species.<sup>13</sup> Desorption proceeds uniformly until a temperature of  $125\text{ }^{\circ}\text{C}$ , where the monocarbonyl band at  $2132\text{ cm}^{-1}$  decreases and diminishes before the dicarbonyl, indicating a stronger retention of the latter.

Cu-ZSM-5 spectra shares similarities to that of Cu-MOR, with bands assigned to  $\text{Cu}^{\text{I}}$  monocarbonyls at  $2124$  and  $2132\text{ cm}^{-1}$ , and  $\text{Cu}^{\text{I}}(\text{CO})_2$  dicarbonyl at  $2155\text{ cm}^{-1}$ . Both mordenite and ZSM-5 samples show characteristic disappearance of monocarbonyl bands above  $125\text{ }^{\circ}\text{C}$ , while the dicarbonyl bands diminish above  $145\text{ }^{\circ}\text{C}$ .

The Cu-SSZ-13 sample displays only two prominent bands at  $2132$  and  $2155\text{ cm}^{-1}$  assigned to mono- and dicarbonyl species, respectively. Similar to the previous samples, desorption of  $\text{Cu}^{\text{I}}\text{CO}$  proceeds faster, but a much higher temperature of  $225\text{ }^{\circ}\text{C}$  is required to completely desorb CO.

### 3.3.2 XANES

The samples were further subjected to XANES measurements in order to deduce the valence state of copper within these materials at the different stages of the reaction, again to ensure that the samples are representative of the materials employed for the methane-to-methanol conversion. The spectra were collected *ex situ*, with the activated and post-extraction samples pelletised; whilst the reacted samples were sealed and loaded into quartz capillaries.

The collected spectra were then compared to reference Cu(I) and Cu(II) samples, presented in Fig. 3.2.1. All of the spectra collected contain a distinct pre-edge feature at  $8977\text{ eV}$ , deriving from the  $1s \rightarrow 3d$  transition and indicative of Cu(II) species.<sup>14</sup> Presence of Cu(II) is also characterised by a rising-edge feature at  $8986\text{ eV}$  which, although clearly defined in the samples measured after the reaction (Fig 3.3.2 B), is not present in spectra collected after activation and extraction stages. This is likely the result of these samples being exposed to air and therefore significantly hydrated prior to analysis, which is

consistent with literature documenting XANES spectra of fresh, hydrated Cu-Mordenite.<sup>15</sup> A pre-edge feature at 8983 eV is distinguishable in the three spectra recorded after reaction with methane and is characteristic of Cu(I) 1s → 4p transition. The reaction with methane thus results in a mixture of Cu(I) and Cu(II) present within the sample, indicating that only some of the Cu(II) species take part in the partial oxidation of methane, again consistent with literature. This feature is not present in the samples measured after activation and extraction stages, indicating that only Cu(II) species are present after activation and post extraction. This supports the aforementioned notion that water is able to re-oxidise Cu(I) species back to Cu(II). Despite this, however, the activity measured is significantly decreased, which suggests that the Cu(II) formed via water-aided oxidation is not active towards the partial oxidation of methane.

Linear combination fits of the spectra were performed and are in agreement with the assignments: the samples contain 100 % Cu(II) species after activation and extraction stages; whilst post-reaction the samples contain a mixture of Cu(I) and Cu(II). The linear combination fits of spectra collected after extraction and the proportions of Cu in the two valence states is presented in Fig. 3.3.3.

Thus, the XANES measurements reveal that the valence state of copper in the samples changes during the different stages of the methane-to-methanol conversion process. These findings are in agreement with literature<sup>15,16</sup>, which also documents the role of Cu(II) and Cu(I) in the methane-to-methanol conversion. The present study confirms that Cu(I) forms during the reaction and suggests that water can re-oxidise Cu(I) back to Cu(II); although the latter, formed in this manner, is not active in methane partial oxidation, as evidenced by the decreased activity measured post-reaction.

While these measurements provide valuable information about the valence states of copper during the reaction, they do not offer precise insight into the exact structure of the active sites responsible for the methane-to-methanol conversion. Indeed, Sushkevich *et al.*<sup>16</sup> concluded that XAS and IR methods are not sensitive enough to differentiate between the different structures of copper-oxo species. This limitation highlights the need for complementary techniques to achieve a more detailed understanding of the active copper species within these zeolitic hosts.

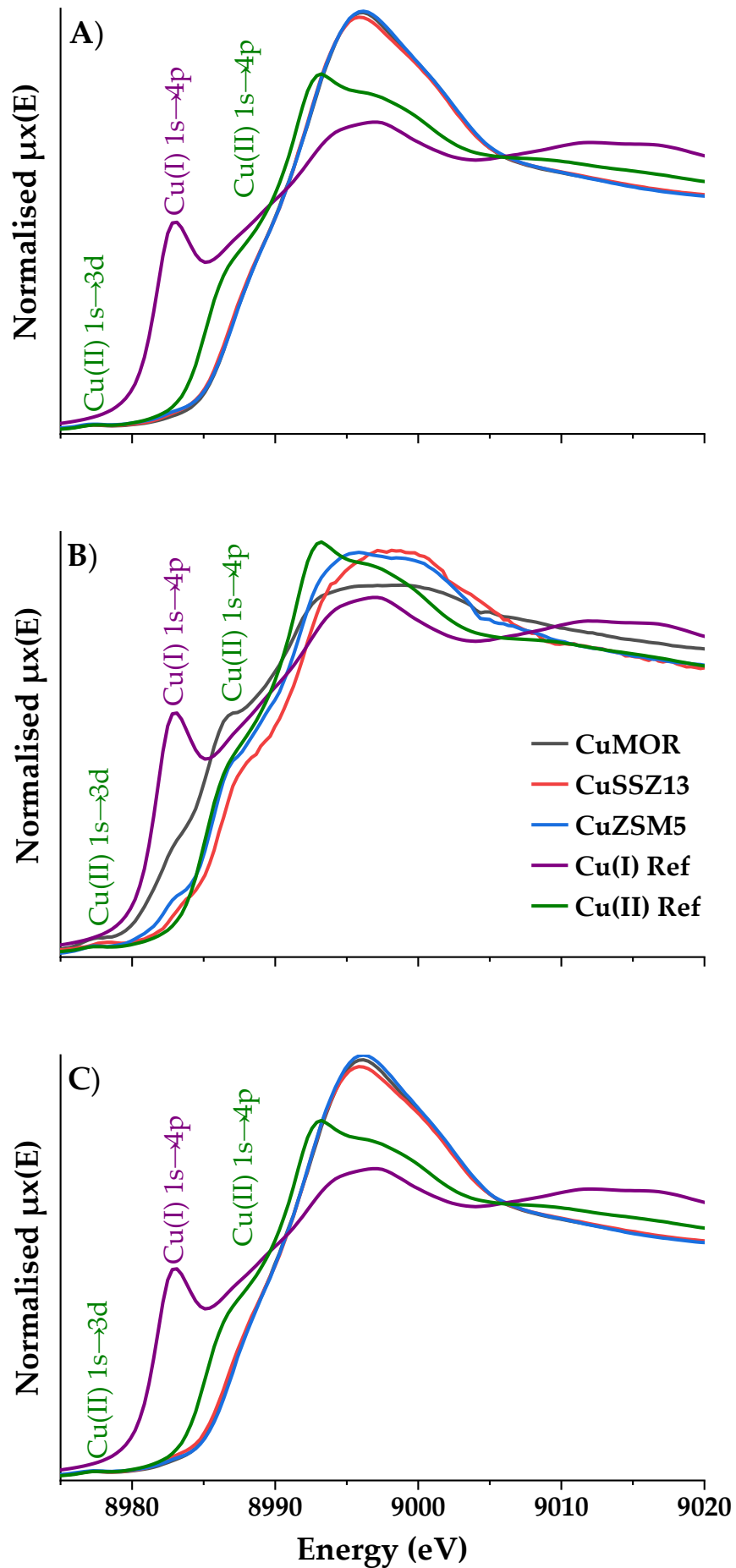


Fig. 3.3.2 XANES spectra of the samples after activation (A); reaction (B); and extraction (C) alongside the Cu(I) and Cu(II) reference spectra.

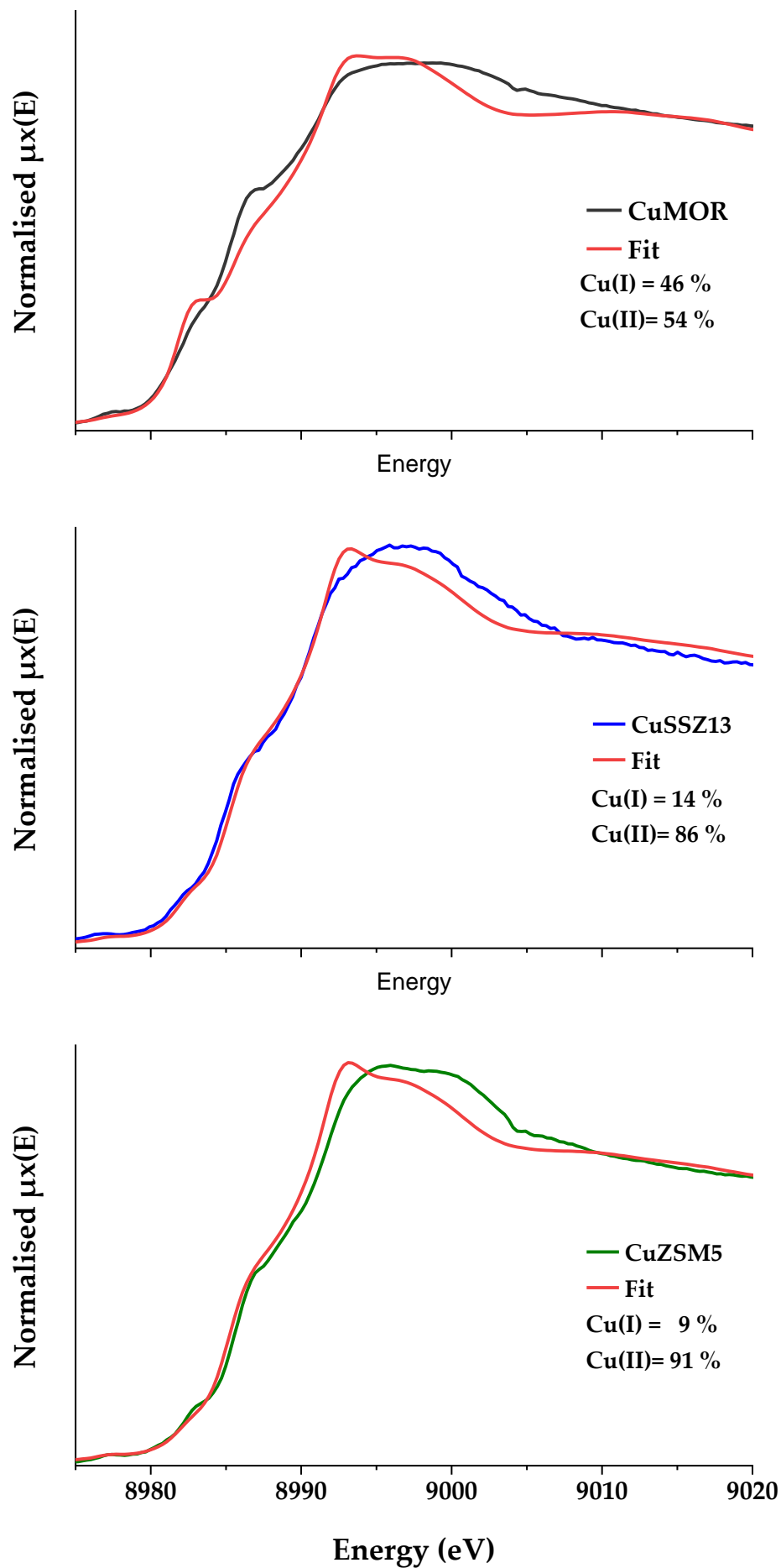
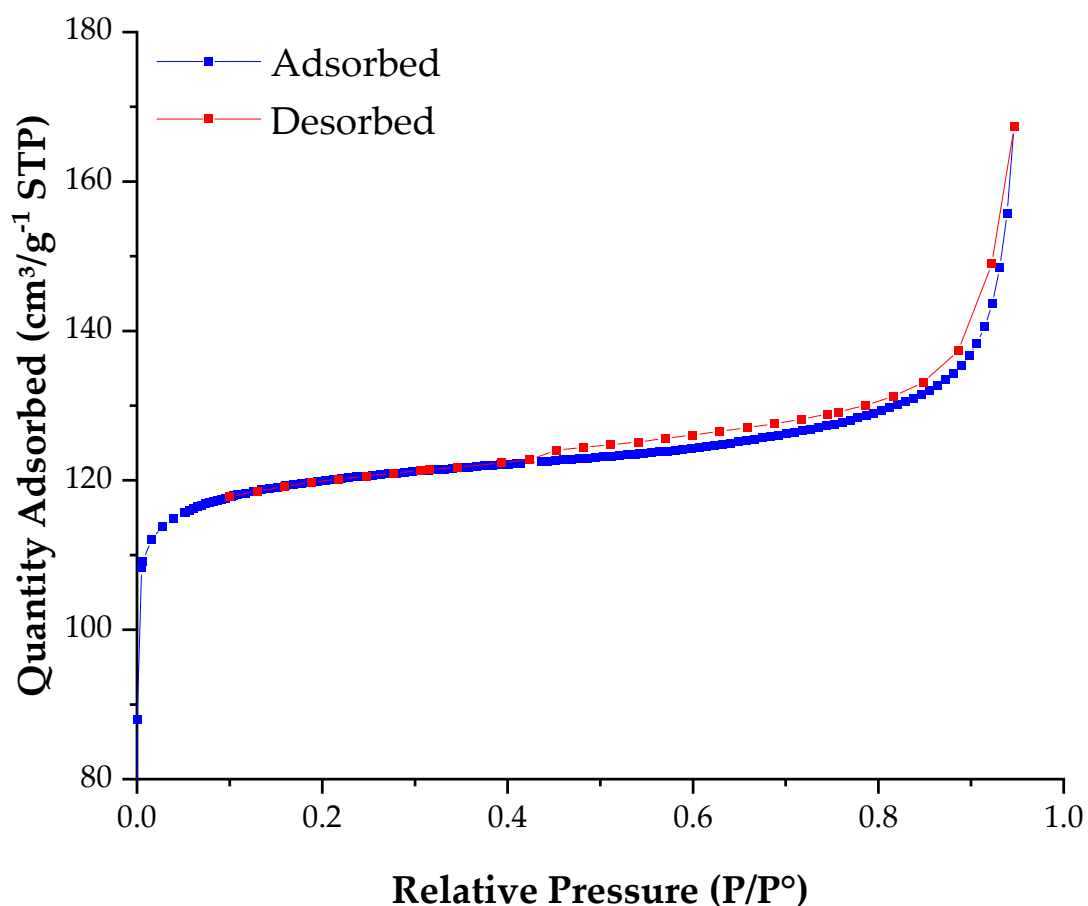


Fig. 3.3.3 Data and linear combination fits to CuMOR (top), CuSSZ-13 (middle), and CuZSM-5 (bottom) collected after reaction with methane.

## 3.4 Structural Changes

### 3.4.1 Surface Area

Surface area analysis was performed on the three zeolites in order to investigate whether the reaction conditions affect the surface area of these microporous materials. The measurements were thus performed on the three zeolites prior to ion exchange (protonic forms); after ion exchange and high-temperature, oxygen activation; and post-reaction with methane. The results of the surface area analysis are presented in Table 3.2. Exemplar N<sub>2</sub> adsorption/desorption isotherms obtained from H-mordenite are shown in Fig. 3.4.1.



**Fig. 3.4.1. Adsorption and desorption isotherms for nitrogen on H-mordenite.**

For both mordenite and SSZ-13, a consistent decrease in surface area was observed after each stage of the process. The initial measurements of the protonic forms show the highest surface areas (367 and 531 m<sup>2</sup> g<sup>-1</sup> for mordenite and SSZ-13, respectively) which marginally reduced (349 and 492 m<sup>2</sup> g<sup>-1</sup>, respectively) after Cu-doping and subsequent activation. This reduction is likely the result of partial-occupation of the zeolites' micropores by copper

ions or small copper-oxide clusters. The high-temperature activation may also induce structural changes, such as dealumination and subsequent collapse of some micropores, leading to a reduction in the accessible surface area.

**Table 3.2 Surface area of the three zeolites prior to Cu-doping; after Cu-doping and activation; and post-reaction. \*Single point surface area.**

Zeolite	Surface Area (m <sup>2</sup> g <sup>-1</sup> )		
	Protonic	Cu-doped	Post-Reaction
Mordenite	367	349	317
SSZ-13	531	492	388
ZSM-5*	215	297	253

Following methane reaction, further decreases in surface area are evident. This may be due to the formation of hydrocarbon species or intermediates which partially block the pores. However, the changes in the surface area are relatively small, suggesting that the overall structural integrity of the mordenite and SSZ-13 samples is, by and large, preserved during the experimental process – albeit this only reflects a single reaction cycle.

For ZSM-5, the surface area analysis was inconclusive as only a single-point BET surface area could be obtained. This makes it difficult to draw any meaningful conclusions, since it does not provide any detailed isotherm data necessary to accurately determine surface area, particularly in materials such as zeolites which have varied pore structures. That is, the single point data would fail to capture any localised changes in the surface area, such as collapse or blockage of some of the pores.

In conclusion, the slight reductions in surface area for mordenite and SSZ-13 suggest that these zeolites experience some pore occupation and/or structural adjustments during copper loading and methane reaction stages; however their frameworks remain largely intact. In contrast, the data obtained for ZSM-5 does not allow for a clear assessment of how its structure is affected through each stage of the experimental process.

### **3.4.2 Dealumination**

The three samples were subjected to <sup>27</sup>Al NMR spectroscopy across several key stages: initial examination of fresh, protonated zeolite before copper impregnation; analysis after introduction of Cu and the subsequent activation; samples after the full methane-to-methanol conversion reaction; and after five consecutive cycles of the reaction, all of which are presented in Fig 3.4.2.

Notably, the introduction of copper into the framework leads to a significant reduction in intensity of the peak around 53 ppm (tetrahedral, framework Al) and a significant dampening or disappearance of the peak at around 0 ppm (octahedral, extraframework Al), which is attributed to paramagnetism of copper. This phenomenon, coupled with the absence of a suitable calibration curve relating the peak intensity in each environment to the number of Al nuclei present, prevents quantitative analysis. Thus the spectra could only be examined qualitatively, whereby reductions in peak areas are compared to that of the activated samples which provides insight into the changes induced by the reaction.

When examining the individual zeolite responses, mordenite demonstrated minimal changes initially but displayed a reduction in peak area after five reactions. This observation suggests the possibility of dealumination within the structure, albeit without precise localisation as the extraframework Al peak is dampened. Zeolite SSZ-13 exhibited a consistent decrease in peak area after each stage of the process, indicating progressive alterations in the aluminium environment; i.e., a loss of the tetrahedral Al. In contrast, the ZSM-5 sample showed the highest stability throughout the experimental stages, with minimal changes observed in its NMR spectra. This stability implies lower susceptibility to dealumination induced by the experimental conditions compared to the other two samples.

Interestingly, while there are clear signs of dealumination occurring, as evidenced by the loss of intensity of tetrahedral aluminium species (particularly noticeable in mordenite and SSZ-13), the concomitant changes in their activity were not observed during the activity tests. This discrepancy suggests that even if dealumination is indeed taking place within these structures, it is not adversely affecting their activity – at least over the five reaction cycles studied. One plausible interpretation of this is that the dealumination is taking place in regions where there are no Cu-active sites present; implying spatial segregation of the dealuminated sites from the catalytically active copper sites and suggesting a more complex relationship between the structural changes and performance than initially anticipated. Further studies over more reaction cycles, as well as  $^{29}\text{Si}$  NMR analysis to enable quantification, are thus warranted to examine these observations, as this was not possible in the present study due to time constraints.

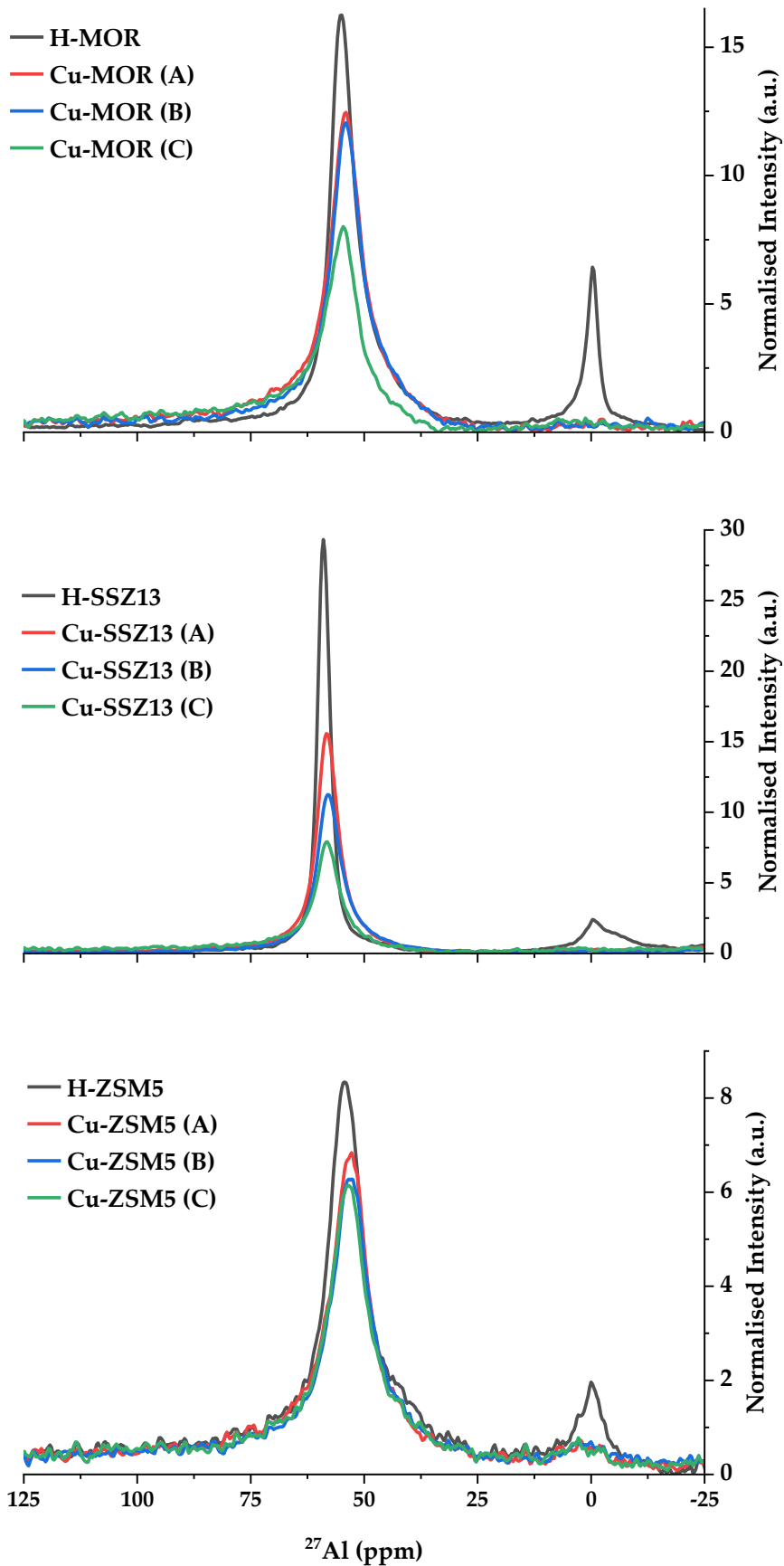


Fig. 3.4.2  $^{27}\text{Al}$  MAS-NMR spectra of the protonated and Cu-doped zeolites. (A) refers to activated sample; (B) sample after one reaction cycle; and (C) sample after five reaction cycles.

### 3.5 Bibliography

- (1) Mitsudome, T.; Arita, S.; Mori, H.; Mizugaki, T.; Jitsukawa, K.; Kaneda, K. Supported Silver-Nanoparticle-Catalyzed Highly Efficient Aqueous Oxidation of Phenylsilanes to Silanols. *Angewandte Chemie - International Edition* 2008, 47 (41).  
<https://doi.org/10.1002/anie.200802761>.
- (2) Sushkevich, V. L.; Palagin, D.; Ranocchiari, M.; Van Bokhoven, J. A. Selective Anaerobic Oxidation of Methane Enables Direct Synthesis of Methanol. *Science (1979)* 2017, 356 (6337).  
<https://doi.org/10.1126/science.aam9035>.
- (3) Dyballa, M.; Pappas, D. K.; Kvande, K.; Borfecchia, E.; Arstad, B.; Beato, P.; Olsbye, U.; Svelle, S. On How Copper Mordenite Properties Govern the Framework Stability and Activity in the Methane-to-Methanol Conversion. *ACS Catal* 2019, 9 (1).  
<https://doi.org/10.1021/acscatal.8b04437>.
- (4) Martini, A.; Borfecchia, E.; Lomachenko, K. A.; Pankin, I. A.; Negri, C.; Berlier, G.; Beato, P.; Falsig, H.; Bordiga, S.; Lamberti, C. Composition-Driven Cu-Speciation and Reducibility in Cu-CHA Zeolite Catalysts: A Multivariate XAS/FTIR Approach to Complexity. *Chem Sci* 2017, 8 (10).  
<https://doi.org/10.1039/c7sc02266b>.
- (5) Li, Y.; Hall, W. K. Catalytic Decomposition of Nitric Oxide over Cu-Zeolites. *J Catal* 1991, 129 (1). [https://doi.org/10.1016/0021-9517\(91\)90024-X](https://doi.org/10.1016/0021-9517(91)90024-X).
- (6) Keith Hall, W.; Valyon, J. Mechanism of NO Decomposition over Cu-ZSM-5. *Catal Letters* 1992, 15 (3). <https://doi.org/10.1007/BF00765276>.
- (7) Jang, H. J.; Keith Hall, W.; D'Itri, J. L. Redox Behavior of CuZSM-5 Catalysts: FTIR Investigations of Reactions of Adsorbed NO and CO. *Journal of Physical Chemistry* 1996, 100 (22).  
<https://doi.org/10.1021/jp952525x>.
- (8) Iwamoto, M.; Yahiro, H.; Tanda, K.; Mizuno, N.; Mine, Y.; Kagawa, S. Removal of Nitrogen Monoxide through a Novel Catalytic Process. 1. Decomposition on Excessively Copper Ion Exchanged ZSM-5 Zeolites. *Journal of Physical Chemistry* 1991, 95 (9).  
<https://doi.org/10.1021/j100162a053>.
- (9) Kuroda, Y.; Iwamoto, M. Characterization of Cuprous Ion in High Silica Zeolites and Reaction Mechanisms of Catalytic NO

Decomposition and Specific N<sub>2</sub> Adsorption. *Top Catal* 2004, 28 (1–4).  
<https://doi.org/10.1023/B:TOCA.0000024340.33790.f8>.

- (10) Lee, D. K. Kinetic Evaluation of Mechanistic Models for O<sub>2</sub> Release from ZSM-5-Supported [Cu<sup>2+</sup>-O-Cu<sup>2+</sup>] Ions by Thermal Reduction or Chemical Interaction with Impinging N<sub>2</sub>O Molecules. *Catal Letters* 2005, 99 (3–4). <https://doi.org/10.1007/s10562-005-2123-7>.
- (11) Liu, D. J.; Robota, H. J. In Situ XANES Characterization of the Cu Oxidation State in Cu-ZSM-5 during NO Decomposition Catalysis. *Catal Letters* 1993, 21 (3–4). <https://doi.org/10.1007/BF00769481>.
- (12) Llabrés i Xamena, F. X.; Fiscaro, P.; Berlier, G.; Zecchina, A.; Palomino, G. T.; Prestipino, C.; Bordiga, S.; Giamello, E.; Lamberti, C. Thermal Reduction of Cu<sup>2+</sup>-Mordenite and Re-Oxidation upon Interaction with H<sub>2</sub>O, O<sub>2</sub>, and NO. *Journal of Physical Chemistry B* 2003, 107 (29). <https://doi.org/10.1021/jp0275847>.
- (13) Hadjiivanov, K. I.; Kantcheva, M. M.; Klissurski, D. G. IR Study of CO Adsorption on Cu-ZSM-5 and CuO/SiO<sub>2</sub> Catalysts:  $\sigma$  and  $\pi$  Components of the Cu<sup>+</sup>-CO Bond. *Journal of the Chemical Society - Faraday Transactions* 1996, 92 (22). <https://doi.org/10.1039/FT9969204595>.
- (14) Borfecchia, E.; Pappas, D. K.; Dybala, M.; Lomachenko, K. A.; Negri, C.; Signorile, M.; Berlier, G. Evolution of Active Sites during Selective Oxidation of Methane to Methanol over Cu-CHA and Cu-MOR Zeolites as Monitored by Operando XAS. *Catal Today* 2019, 333. <https://doi.org/10.1016/j.cattod.2018.07.028>.
- (15) Newton, M. A.; Knorpp, A. J.; Pinar, A. B.; Sushkevich, V. L.; Palagin, D.; Van Bokhoven, J. A. On the Mechanism Underlying the Direct Conversion of Methane to Methanol by Copper Hosted in Zeolites; Braiding Cu K-Edge XANES and Reactivity Studies. *J Am Chem Soc* 2018, 140 (32). <https://doi.org/10.1021/jacs.8b05139>.
- (16) Sushkevich, V. L.; Safonova, O. V.; Palagin, D.; Newton, M. A.; van Bokhoven, J. A. Structure of Copper Sites in Zeolites Examined by Fourier and Wavelet Transform Analysis of EXAFS. *Chem Sci* 2020, 11 (20). <https://doi.org/10.1039/d0sc01472a>.

---

## Experiments With Neutrons

The direct methane-to-methanol conversion using copper-loaded zeolites is a promising area of research, yet the literature lacks comprehensive studies of the molecular dynamics taking place within these catalysts. Despite a growing body of research on the active sites and conversion mechanisms, few studies focus on how various molecules behave within these Cu-loaded materials. While there exists an extensive body of research on other molecules such as ammonia,<sup>1</sup> methanol,<sup>2</sup> propene<sup>3</sup> and water<sup>4</sup> confined within different zeolite structures, the understanding of such processes within Cu-based methane-to-methanol conversion catalysts remains insufficient.

Understanding the dynamic interactions at the interface between the catalyst and various species, including reactants, intermediates and products is a crucial aspect of catalysis. The rate-limiting step in a catalytic process can involve the transport of reactants to the active site; adsorption of reactants on the active site; conversion of reactants at the active site; or the subsequent removal and transport of products from the active site.<sup>5</sup> Understanding these processes is vital, as the behaviour of guest molecules within the zeolite framework plays a fundamental role in determining the catalytic performance of the material. A comprehensive review by Mitra *et al.*<sup>6</sup> highlights several factors influencing the dynamics of guest-host interactions in zeolites. Such factors include framework topology, cation content, and the size, symmetry and quantity of the guest molecules. These variables collectively determine the ease with which reactants and products are able to move to and from the active sites within these materials. Diffusion is the primary process by which guest molecules move within the framework and mass transfer limitations affect the overall rates of reactions.<sup>7</sup> Nonetheless, there is currently no consensus on the specific mechanisms governing diffusion in zeolites due to the complexity of the interplay between the guest-host structures and chemistry.<sup>8,9</sup>

Investigating the dynamics of various species can be challenging, however, due to the overlap of different types of molecular motions, such as rotations and translations. Macroscopic techniques, including gravimetry<sup>10</sup> and membrane permeation,<sup>11</sup> focus on mass transfer processes in the presence of concentration gradients. In contrast, microscopic methods such as pulsed field gradient nuclear magnetic resonance (PFG-NMR)<sup>12</sup> and quasielastic neutron scattering (QENS)<sup>13</sup> probe the stochastic motions of molecules, thus allowing the analysis of molecular self-diffusivity in absence of a concentration

gradient. Neutron scattering is particularly valuable for investigating the structural and dynamic properties of materials because the wavelength and energy of neutrons align well with the interatomic distances and molecular kinetics. Moreover, the large incoherent scattering cross section of hydrogen makes neutrons an excellent tool for probing dynamics involving protons, providing insights that are often difficult to obtain using other methods.<sup>14</sup> Unlike other measurement techniques which average data over longer distances and times, QENS provides direct insights into the diffusion mechanisms taking place, making it an ideal tool for investigating the behaviour of various molecules within copper-loaded zeolites.

## **4.1 Dynamics of Water**

### **4.2.1 Motivation**

Purely siliceous zeolitic materials are hydrophobic and repel the sorption of water molecules.<sup>15</sup> However, increasing the aluminium and the corresponding cation content within the zeolitic framework enhances dipole-ion interactions, thereby increasing the material's polarity and reducing its hydrophobicity.<sup>16</sup> By facilitating methanol desorption, water plays a crucial role in the methane-to-methanol conversion process, as well as in a myriad of other biological, chemical and geophysical processes.<sup>4</sup> Understanding how water molecules interact with surfaces and navigate geometrical confinement is critical for optimising catalyst design for broader applications as well as the methane-to-methanol conversion.

### **4.2.2 Experimental**

#### **4.2.2.1 Preparation of Zeolites**

The zeolites were prepared and ion-exchanged with copper as per Section 2.3.1 of Chapter 2. The resulting Cu-loaded mordenite, SSZ-13 and ZSM-5 zeolites contained copper at concentrations of 3.31 %, 3.15 % and 5.32 % by weight, respectively, as determined through XRF analysis using the Malvern Epsilon 3. The powder X-ray diffraction (PXRD) patterns of the catalysts, both before and after ion exchanged, were recorded using a Rigaku Miniflex

diffractometer and are presented in Fig. 4.1.1. The patterns were compared with the zeolite structure database to confirm their structural integrity.<sup>17</sup> The absence of changes in the PXRD patterns before and after copper loading indicates the successful incorporation of copper into the zeolite frameworks, with no visible loss of crystallinity or detectable CuO.

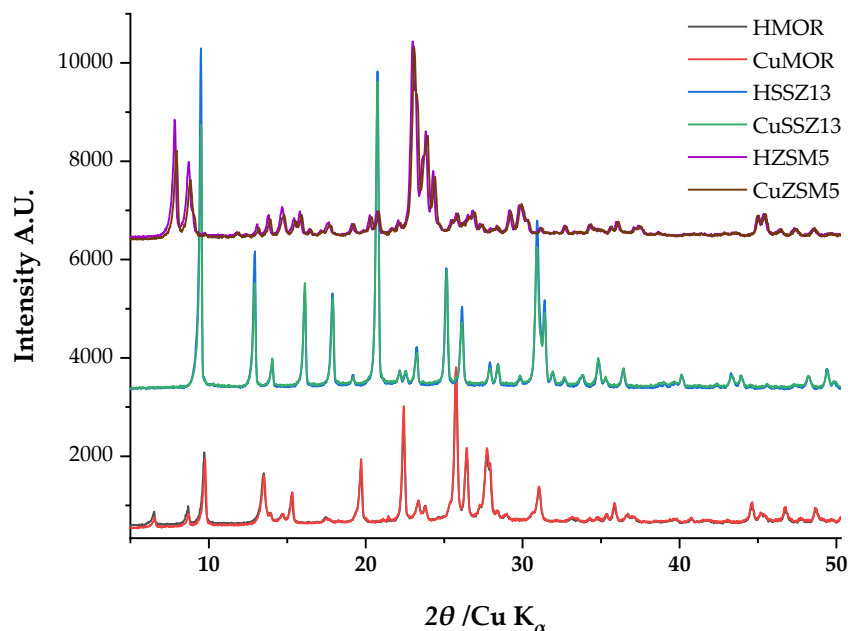


**Fig. 4.1.1** PXRD patterns of protonic and Cu-loaded zeolites.

#### 4.2.2.2 Water Dosing

The samples were initially dried in a furnace at 623 K, overnight, using a stainless steel CF16 sample holder sealed with copper gaskets and connected to a vacuum system incorporating a turbopump. After drying, the samples were transferred to an argon-filled glovebox for further handling. A measured portion of each sample was then placed in a desiccator containing saturated KNO<sub>3</sub> solution, which maintained 95 % relative humidity, for 20 hours to allow equilibration. The samples were subsequently reweighed and sealed in aluminium cans for QENS measurements. This process yielded three samples: 2.51 g of Cu-MOR, containing 37.8 % water (w/w) at approximately 97 water molecules per unit cell (MPUC); 2.20 g of Cu-SSZ-13, containing 20.0 % water (w/w) at approximately 30 MPUC; and 2.16 g of Cu-ZSM-5, containing 12.50 % water (w/w) at approximately 46 MPUC.

### 4.2.2.3 QENS Measurements

The QENS measurements were conducted using the IRIS<sup>18</sup> spectrometer at the ISIS Neutron & Muon Source. The graphite analyser, using the (002) reflection, provided a resolution of 17.5  $\mu\text{eV}$  and a Q range of 0.4–1.9  $\text{\AA}$ . The samples were initially cooled to below 15 K to acquire the instrumental resolution function; spectra were then collected at temperatures of 100 K, 200 K and 300 K. The experimental spectra were analysed by fitting them with the resolution function, convoluted with a delta function to account for the elastic scattering from immobile atoms, and Lorentzian functions to model the energy broadening from scattering by moving particles. The data reduction and analysis were carried out using the Mantid<sup>19</sup> and DAVE<sup>20</sup> software packages.

### 4.2.3 Results & Discussion

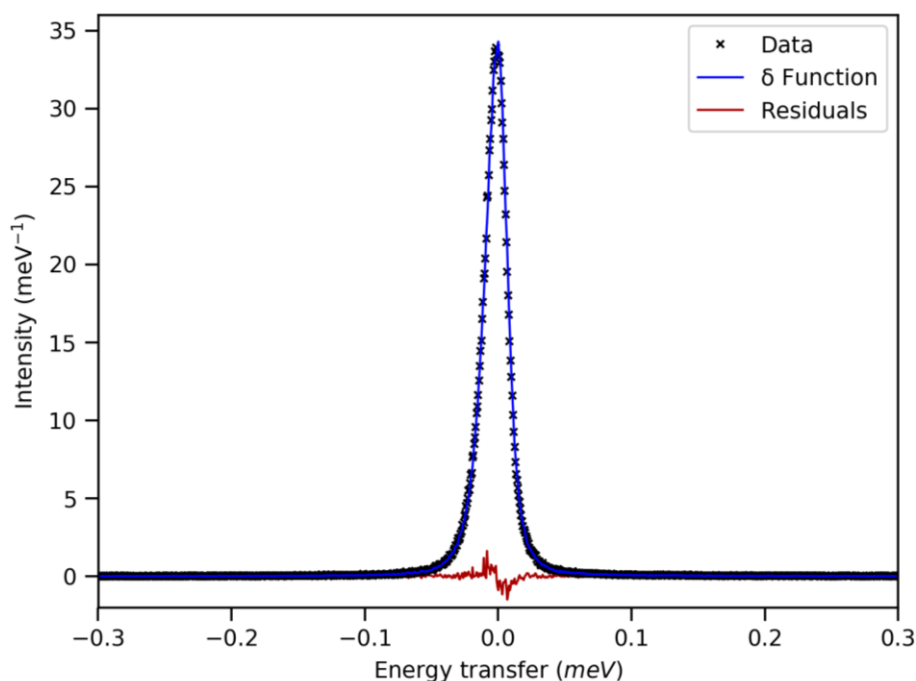


**Fig. 4.1.2 Data obtained from Cu-ZSM-5 at 100 K and the fit applied.**

The spectra obtained at 100 K contained a quasielastic peak which, for all three Cu-loaded zeolites, was adequately fitted using a delta function convoluted with the instrumental resolution, as shown in Figure 4.1.2. This suggests that all observed scattering is elastic, which occurs from static atoms, whether originating from the zeolitic framework or the adsorbed water molecules. Any diffusive motions were therefore outside the experimental time-window, as

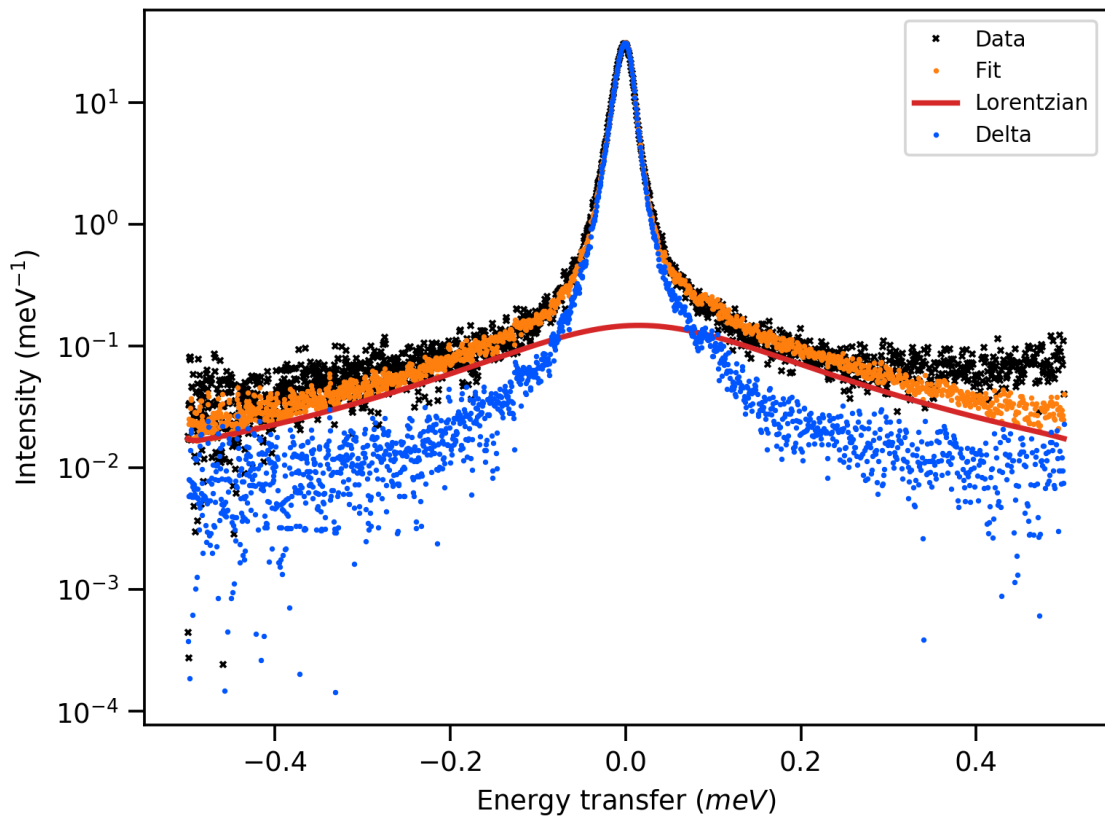


Fig. 4.1.3 Data obtained from CuMOR at 200 K and the fits applied.

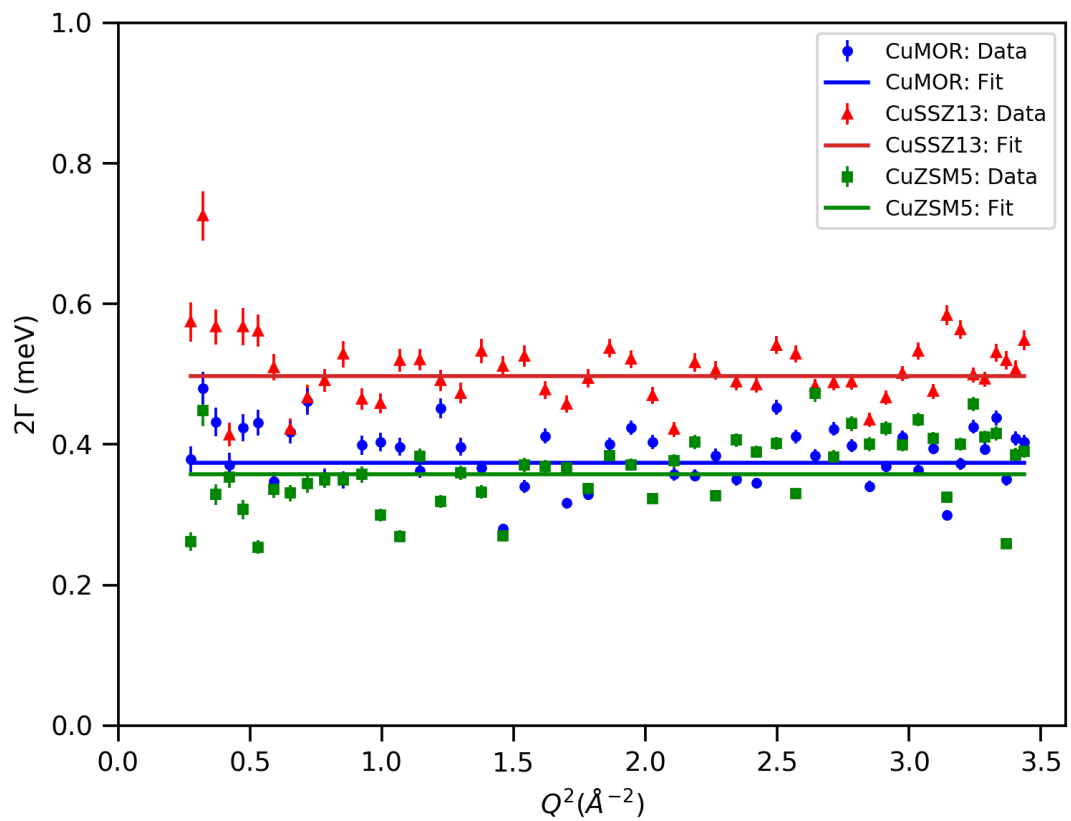
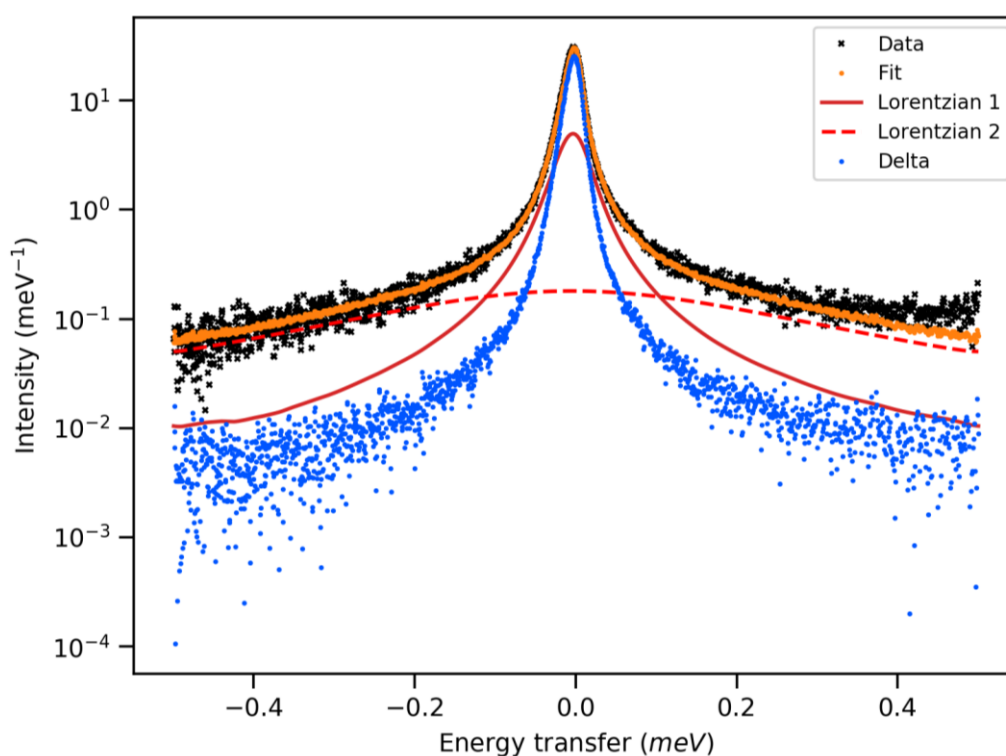


Fig. 4.1.4 Lorentzian linewidths from fits to spectra measured at 200 K.

defined by the instrumental resolution. Increasing the temperature to 200 K resulted in broadening of the quasielastic peak for all three water-sorbed samples, which consequently required a resolution-convoluted delta function and a single Lorentzian function to adequately fit the data (Fig. 4.1.3). The linewidths (HWHM or  $\Gamma$ ) obtained for all three Cu-zeolites were independent of  $Q$  – i.e., consistent across different scattering vector values – as shown in Fig. 4.1.4. These linewidths correspond to the time constant for the rotational motion of water molecules, with the exact values listed in Table 4.1. While the elastic incoherent scattering function (EISF) may be used to analyse the geometry of confined molecular motion, its application herein was constrained by the limited  $Q$  range as well as the small size of the water molecules.



**Fig. 4.1.5 Data obtained from Cu-SSZ-13 at 300 K and the fits applied.**

At 300 K, the spectra obtained from all three samples showed a further broadening of the quasielastic line, which was effectively modelled using a combination of two Lorentzian components: one for rotational motion and one for translational motion. The linewidths associated with the latter were analysed using the Singwi & Sjölander<sup>21</sup> (SS) jump diffusion model, which has the following form:

$$\Gamma_Q = \frac{1}{\tau_0} \left[ 1 - \left( \frac{\exp - (2W)}{1 + DQ^2\tau_0} \right) \right]$$

where

$$2W = DQ^2\tau_0 \frac{\langle R^2 \rangle}{\langle l^2 \rangle}$$

In this model,  $\tau_0$  represents the average time a molecule spends oscillating before undergoing linear diffusive motion;  $\langle R^2 \rangle$  denotes the mean square radius of the thermal cloud created by the oscillatory motions; and  $\langle l^2 \rangle$  is the mean square jump length. The derived parameters for both rotational and translational dynamics are summarised in Table 4.1.

**Table 4.1 Rotational & Translational Dynamics of Water in three Cu-loaded zeolites at 200 and 300 K.**  $\tau_r$  and  $\tau_t$  correspond to rotational and translational components, respectively.

Sample	T (K)	$\tau_r$ (ps)	$\sqrt{\langle l^2 \rangle}$ (Å)	$\tau_t$ (ps)	$D_s$ (m <sup>2</sup> s <sup>-1</sup> )
Cu-MOR	200	3.52	–	–	–
Cu-SSZ-13	200	2.65	–	–	–
Cu-ZSM-5	200	3.69	–	–	–
Cu-MOR	300	2.16	4.17	23.19	$1.25 \times 10^{-9}$
Cu-SSZ-13	300	2.23	3.44	20.64	$9.53 \times 10^{-10}$
Cu-ZSM-5	300	2.27	7.06	21.35	$3.89 \times 10^{-9}$
Cu-ZSM-5*	300	n/a	3.65	7.99	$2.77 \times 10^{-9}$

\*Quasielastic line broadening fitted using a single Lorentzian and a background

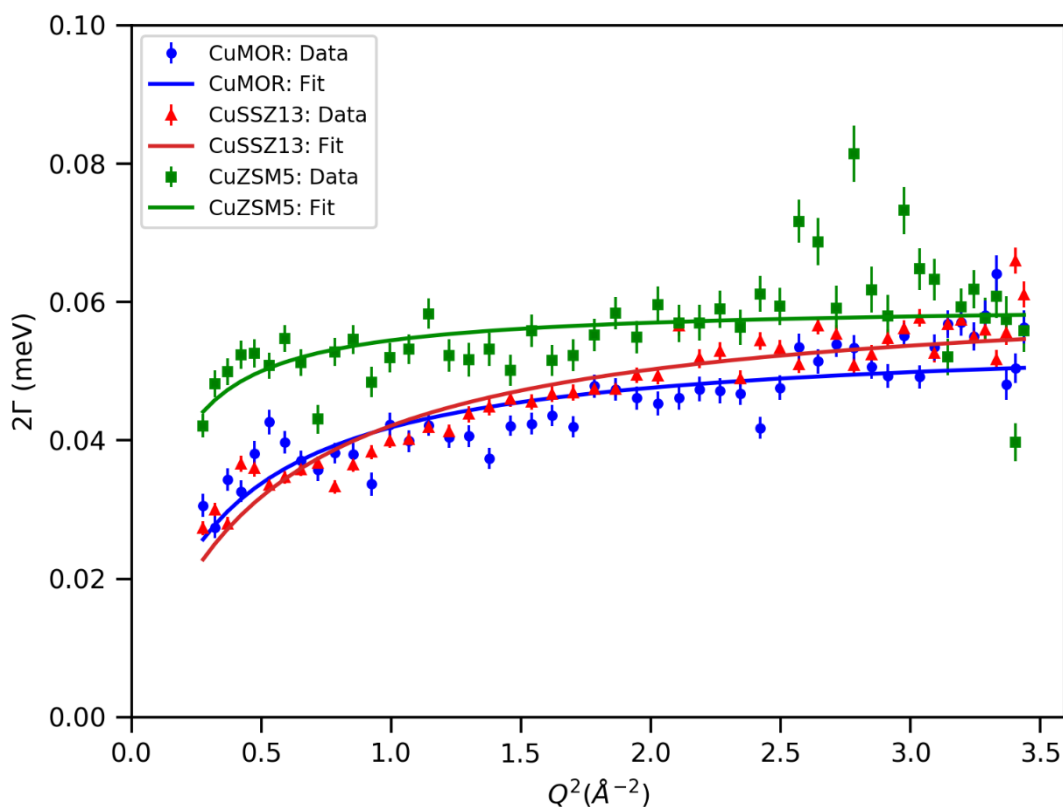


**Fig. 4.1.6 Linewidths of the translational component from fits to spectra measured at 300 K.**

For the mordenite and ZSM-5 samples, the rotational times were similar at 3.52 ps and 3.69 ps, respectively, at 200 K. This similitude is likely the result of a comparable cation content (3.31 % in Cu-MOR and 3.15% in Cu-ZSM-5), providing a comparable number of adsorption sites. In contrast, Cu-SSZ-13 displayed a considerably shorter rotation time of 2.65 ps, attributed to its higher cation content (5.32 %) and a smaller cavity size ( $3.8 \times 3.8 \text{ \AA}$ ). These factors enhance water-cation interactions, leading to more frequent reorientation of the water molecules. Upon increasing the temperature to 300 K, a decrease in rotational time was observed for Cu-MOR and Cu-ZSM-5; however minimal changes were observed within Cu-SSZ-13, suggesting that the amount and distribution of copper, along with the cavity size, have a more significant impact on rotational dynamics than the temperature probed.

The diffusion constant for water within Cu-ZSM-5, derived from the two-Lorentzian fit, appears questionable. Although the residence time was comparable to the other samples, the calculated diffusion constant ( $3.89 \times 10^{-9} \text{ m}^2 \text{ s}^{-1}$ ) exceeds that of bulk water at room temperature ( $2.5 \times 10^{-9} \text{ m}^2 \text{ s}^{-1}$ ); and the jump length ( $7.06 \text{ \AA}$ ) is larger than the pore cage size ( $5.6 \times 5.6 \text{ \AA}$ ). The data was subsequently fitted using a single Lorentzian component alongside a flat background – indicating motions too fast for the experimental time window – which resulted in a more realistic jump length of  $3.65 \text{ \AA}$ . However, this

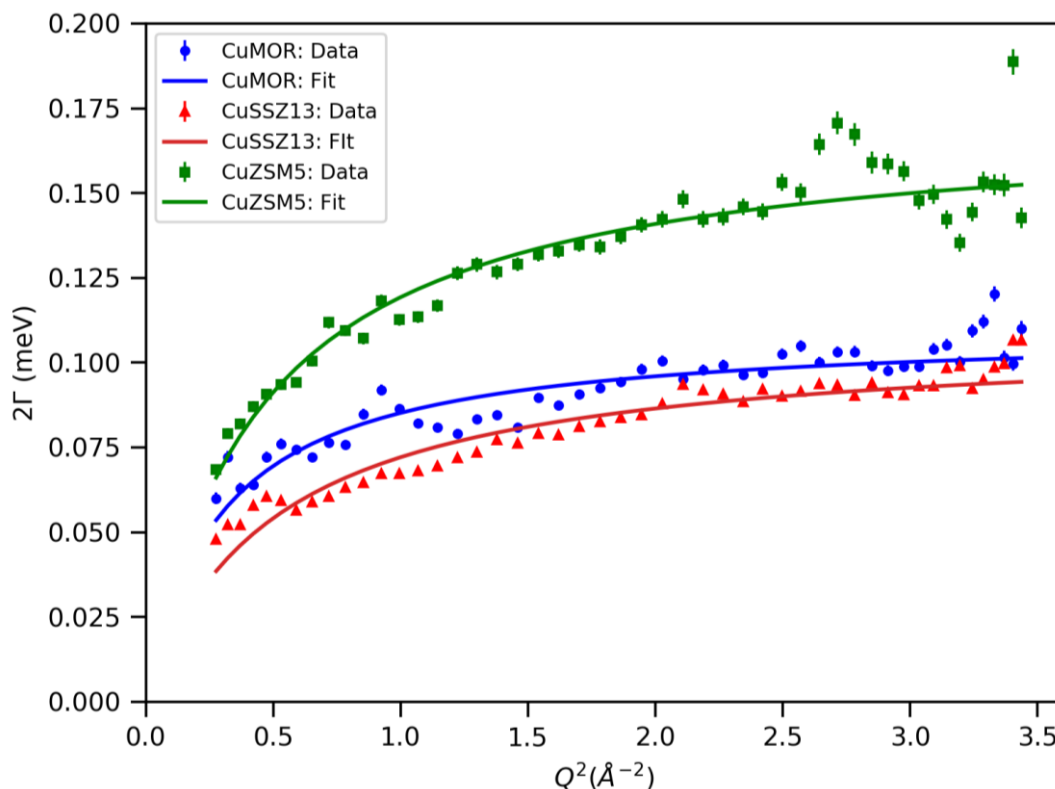


**Fig. 4.1.7** Linewidths from spectra obtained at 300 K and fitted using a single Lorentzian and a flat background.

resulted in a reduced residence time and the diffusion constant still exceeding that of bulk water. Interestingly, each fitting model produced either a jump length or a residence time parameter comparable to those of the other two samples studied. This suggests that within ZSM-5, the rates of rotational and translational motions may overlap too closely to be resolved separately without higher instrumental resolution. The single-Lorentzian and flat background fit was also applied to the other two samples for comparison purposes. Although this model provided Lorentzian linewidths which were adequately fitted using the SS jump diffusion model (see Fig. 4.1.7), it resulted in higher residuals in the individual spectra, indicating that additional components are necessary for a more accurate representation of the quasielastic line broadening. Thus, the two-Lorentzian model is considered a better fit for these systems, as supported by the diffusion constants obtained for both mordenite and SSZ-13 samples. For example, the diffusion constant for mordenite, at  $1.25 \times 10^{-9} \text{ m}^2 \text{ s}^{-1}$ , is comparable to that found in Prussian blue ferrocyanide ( $1.36 \times 10^{-9} \text{ m}^2 \text{ s}^{-1}$ ) which has pores of similar size ( $\sim 6 \text{ \AA}$ ).<sup>22</sup>

Some of the water molecules are situated in hydration shells around charge-balancing cations and experience reduced mobility; Mitra *et al.*<sup>23</sup> documented that, at lower temperatures, such water can become effectively immobile for the timescale of the instrument, leading to reduced average diffusivity. An increase in temperature reduces this fraction, thus enhancing overall mobility. Sharma *et al.*<sup>24</sup> have also reported this phenomenon, attributing it to increased thermal energy, which allows water molecules to break free from cation coordination. Furthermore, the amount of water affects the diffusivity thereof; larger water clusters with more molecules situated farther from the framework cations experience less hindrance. Hence, the slower diffusivity observed in SSZ-13, at  $9.53 \times 10^{-10} \text{ m}^2 \text{ s}^{-1}$ , is due to its higher cation content, smaller pore size and lower water content.

#### 4.2.4 Conclusions

QENS was successfully employed to explore the dynamics of water confined within three different Cu-loaded zeolites. At 100 K, no motions were detected; at 200 K, rotational dynamics were observed; and at 300 K, both rotational and translational motions were evident. The diffusion constants for mordenite and SSZ-13 at 300 K were found to be slower than those of bulk water, attributed to the strong interactions between water molecules and the Cu ions within the zeolites' pores, which impede the movement between adjacent positions.

Notably, SSZ-13 exhibited even slower diffusivity due to its higher Cu counterion concentration and a lower water content.

Calculated jump lengths within mordenite and SSZ-13 were smaller than the zeolites' pores, suggesting that the observed diffusivity is localised within the pores; with the jump lengths comparable to those in bulk water. Grifoni *et al.*<sup>25</sup> recently reported that water does not diffuse between zeolite's pores, but rather forms clusters of limited size at the Brønsted acid sites (BAS). This occurs due to the initial water molecule remaining close to the zeolite framework to avoid excessive charge separation; with the hydrogen bond network keeping the water clusters compact, preventing the water molecules from diffusing throughout the entire cavity. Thus, the jump lengths observed in this study likely correspond to movements within water clusters located at various cationic sites and BAS. For Cu-ZSM-5, it was not possible to separately resolve the rotational and translational dynamics of water, likely due to the close overlap of these motions in terms of their rate.

## **4.3 Dynamics of Methane**

### **4.3.1 Motivation**

Studying the dynamics of methane within Cu-loaded zeolites is pivotal in advancing the understanding of methane partial oxidation. Methane's inherent stability renders it an exceptionally challenging substrate for catalytic reactions; and the role of copper-loaded zeolites in facilitating this process is of great interest. Understanding how methane behaves within these zeolites, including its mobility and interactions with the copper sites, is of paramount importance in delineating reaction mechanisms and the efficiency of this catalytic process. This knowledge is crucial in advancing the optimisation of catalyst performance, improving the overall efficiency of methane conversion and thus enhancing the ability to utilise methane as a valuable feedstock in various industrial applications.

### **4.3.2 Experimental**

#### **4.3.2.1 Preparation of Zeolites**

The zeolites were prepared and ion-exchanged with copper according to the procedure detailed in Section 2.3.1 of Chapter 2. These samples – Cu-loaded mordenite, SSZ-13, and ZSM-5 – were the same as those used in the water study, but only the dry portion was utilised for the subsequent pretreatment and measurements. The copper concentrations were 3.31 %, 3.15 % and 5.32 % (w/w), respectively, as determined by XRF analysis using the Malvern Epsilon 3.

#### **4.3.2.2 Methane Dosing**

The dry copper zeolites used in the water study were transferred to flow-through sample cans and sealed, with the sample handling performed in an argon-filled glovebox. The samples were then dosed with methane by flowing 50% CH<sub>4</sub> (in Ar) at 100 sccm for one hour. Following this, the samples were transferred back to the glovebox and sealed in aluminium sample cans using indium wire gaskets to prevent contamination with air.

#### **4.3.2.3 QENS Measurements**

The QENS measurements were performed using the IRIS<sup>18</sup> spectrometer at the ISIS Neutron & Muon Source, UK. The graphite analyser, with a (002) reflection, achieved a resolution of 17.5  $\mu\text{eV}$  and a Q range from 0.4 to 1.9  $\text{\AA}^{-1}$ . The samples were initially cooled to 15 K to determine the instrumental resolution function. Measurements were then taken at 100 K, 200 K and 300 K to complement the previous study of water. The experimental spectra were then analysed by fitting them with a resolution function convoluted with combinations of Delta and/or Lorentzian functions to account for elastic and quasi-elastic scattering, respectively. Data reduction and analysis were conducted using MANTID<sup>19</sup> and DAVE.<sup>20</sup>

### **4.3.3 Results & Discussion**

The QENS measurements of methane adsorbed onto Cu-mordenite, Cu-SSZ-13 and Cu-ZSM-5 resulted in low-intensity spectra across the whole temperature range studied (100 – 300 K). The spectra were thus adequately

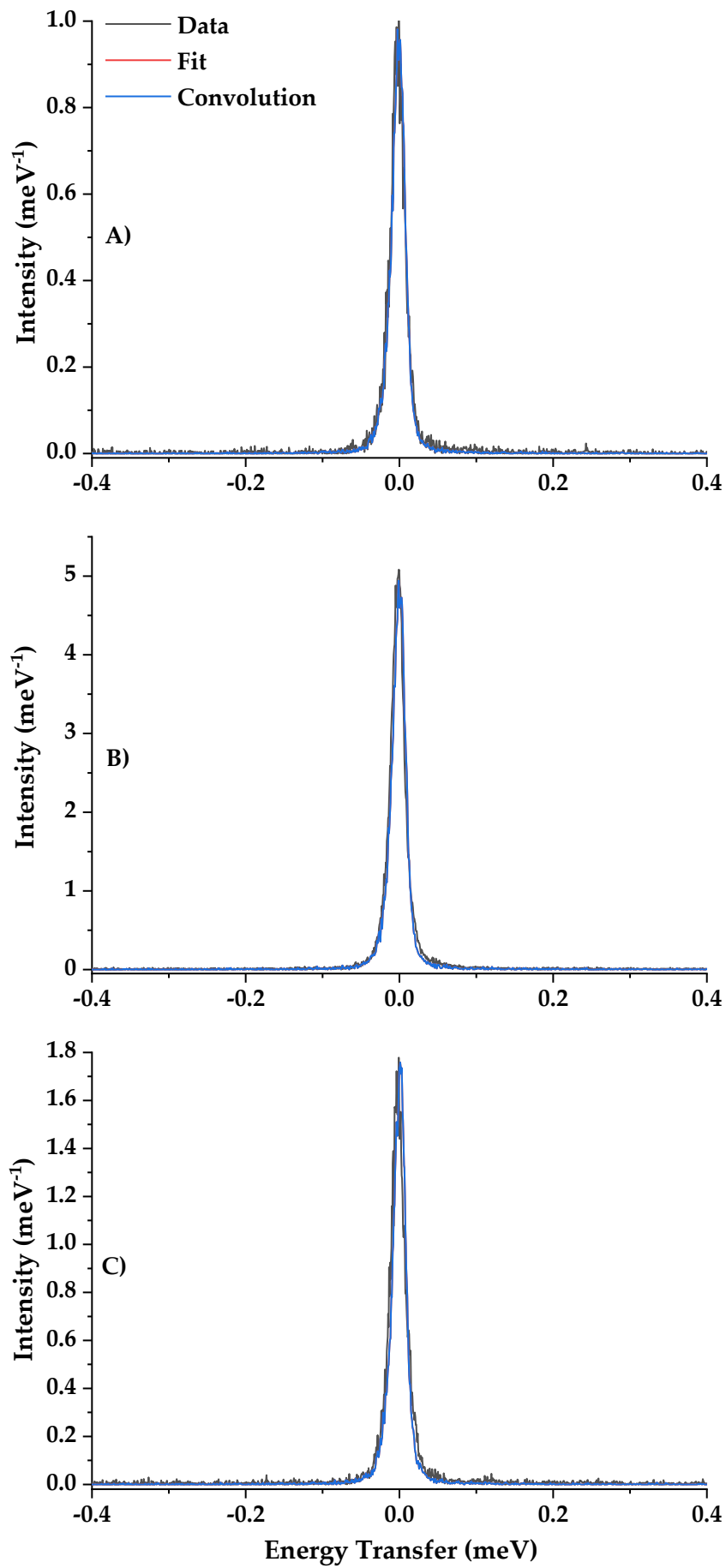


Fig. 4.2.1 Spectra obtained from the Cu-loaded and methane-dosed mordenite (A), SSZ-13 (B) and ZSM-5 (C) at 300 K and the fits applied.

fitted with a resolution-convoluted delta function, indicating that no motions were observed within the experimental time-window of the instrument.

The lack of observable motion could be attributed to several factors. One possibility is very low adsorption of methane on the zeolite samples. Such low adsorption could be due to sample loss during pretreatments in the previous, water study as well as the present one, reducing the effective surface area available for the adsorption on methane. Alternatively, it is also possible that no significant adsorption of methane occurred at all, resulting in the absence of detectable dynamic processes in the QENS measurements. Lastly, the time taken for the measurements may not have been sufficient to acquire an adequate signal – especially in the case of low methane adsorption.

In contrast, previous studies have documented the diffusivity of methane within Na-MOR<sup>26</sup> and Na-ZSM-5<sup>27</sup> zeolites using pulsed field gradient nuclear magnetic resonance (PFG-NMR) and QENS experiments. These results were largely in agreement with molecular dynamics simulations, indicating effective methane diffusion in sodium-based zeolites. Furthermore, the derived diffusion coefficients were in the order of  $10^{-9} \text{ m}^2 \text{ s}^{-1}$ , which are well within the experimental time-window of the IRIS spectrometer used in this study. The discrepancy between these findings and the present study, therefore, may highlight the critical role of the cation type and pretreatment conditions in facilitating both methane adsorption and mobility.

Overall, the findings suggest that the experimental conditions used in the present study were not optimal for subsequent observation of methane dynamics within these Cu-loaded zeolite systems. Further investigation is necessary to determine whether modifying the pretreatment process or adjusting the experimental parameters could enhance methane adsorption and the subsequent observation of the dynamics thereof. Comparing such results with documented studies on other zeolites could then provide valuable insights into optimising conditions for methane adsorption and mobility with regards to the partial oxidation of methane.

#### **4.3.4 Conclusions**

QENS measurements of methane adsorbed onto the three Cu-loaded zeolite samples yielded low signal spectra at all temperatures. The spectra were adequately fitted with a resolution-convoluted delta function, indicating no observable methane dynamics within the experimental time window. The lack of detectable dynamics may be due to very low methane adsorption, possibly

resulting from sample loss during pretreatment, or no significant adsorption occurring. Previous research successfully probing methane dynamics within other, similar zeolites implies that further work is needed to optimise the experimental conditions, including pretreatment processes and measurement parameters, to enhance methane adsorption and enable the study of its dynamics within these materials.

## **4.4 Dynamics of Methanol**

### **4.4.1 Motivation**

Previous research has provided insights into methanol dynamics within various zeolites such as H-ZSM-5,<sup>2</sup> revealing that an increase in the Si/Al ratio correlates with a greater proportion of mobile methanol atoms. This study extends these findings by investigating the behaviour of methanol in Cu-loaded zeolites, which relates to the methanol desorption following the partial oxidation of methane. The objectives were therefore twofold: first, to understand how methanol behaves in the presence of copper within the zeolite framework, and second, to understand the impact of copper on methanol dynamics by comparing the results with those from similar studies of other zeolite systems. Through this comparative analysis, the study aimed to delineate how copper modifies methanol interactions and mobility, thereby improving the understanding of the role of Cu sites in this catalytic process and beyond.

### **4.4.2 Experimental**

#### **4.4.2.1 Preparation of Zeolites**

The zeolites were prepared and subjected to ion exchange with copper according to the method described in Section 2.3.1 of Chapter 2. The resulting Cu-loaded mordenite, SSZ-13 and ZSM-5 zeolites contained 3.31 %, 3.15 % and 5.32 % (w/w), respectively, as determined via XRF analysis using the Malvern Epsilon 3. This equated to approximately 1 Cu per unit cell (PUC) in each zeolite.

#### 4.4.2.2 Methanol Dosing

The zeolites were subjected to drying and activation by heating in a furnace to 723 K, at a rate of 10 K/min under pure oxygen flow; held at this temperature for 1 hour; and subsequently cooled to room temperature. Methanol dosing involved flowing pure argon through a bubbler containing HPLC-grade methanol for 30 minutes. The QENS samples were dosed at 298 K, whilst the samples intended for INS measurements were dosed at 350 K to match the intermediate temperature studied via QENS. Pretreatments were carried out in sealable, flow-through cans as described in reference, with all flow rates maintained at 200 sccm. The samples were then transferred to an argon glovebox and sealed in aluminium cans using indium wire gaskets. Methanol uptake, determined via thermogravimetric analysis, was approximately 9, 7 and 13 molecules per unit cell (MPUC) within Cu-mordenite, Cu-SSZ-13 and Cu-ZSM-5, respectively.

#### 4.4.2.3 QENS Measurements

QENS measurements were performed using the cold-neutron backscattering spectrometer Emu<sup>28</sup> at the Australian Nuclear Science and Technology Organisation (ANSTO). The Si (111) reflection analyser provided a resolution of 1.0  $\mu\text{eV}$  and covered a Q-range of 0.1–2.0  $\text{\AA}^{-1}$ . To achieve a satisfactory signal-to-noise ratio for fitting, the data were re-binned in Q, adjusting the accessible limits to 0.2–1.8  $\text{\AA}^{-1}$  from the theoretical maximum range. The instrumental resolution function was obtained using a vanadium standard measurement. Methanol-dosed zeolites were measured at 300, 325, 350 and 375 K. The experimental spectra were fitted by convoluting the instrumental resolution with a combination of a delta function, representing elastic scattering from immobile atoms, and Lorentzian functions, representing the doppler broadening of the elastic line from moving particles. Data reduction, can subtraction subsequent analysis were carried out using Mantid<sup>19</sup> and DAVE.<sup>20</sup>

#### 4.4.2.4 INS Measurements

INS measurements were performed using the indirect geometry spectrometer TOSCA<sup>29</sup> at the ISIS Neutron & Muon Source, UK. To minimise thermal motions and background signals, the samples were cooled to below 20 K prior to collection of the INS spectra.

### 4.4.3 Results & Discussion

Spectra collected at 300, 325, 350 and 375 K contained both elastic and quasielastic components. Each spectrum was successfully fitted using the instrumental resolution convoluted with a delta function for the elastic component and a single Lorentzian function for the quasielastic component. A subset of the data is presented in Fig. 4.3.1. All spectra contain a prominent elastic component which originates from the relatively static atoms in the zeolite framework, which scatter coherently and generate a low-resolution background with strong Bragg scattering. Due to experimental time constraints during the pandemic, obtaining a data set of the empty zeolites for subtraction was not feasible. As a result, separating incoherent and coherent elastic scattering was not possible, thereby precluding the analysis of the elastic incoherent structure factor (EISF).

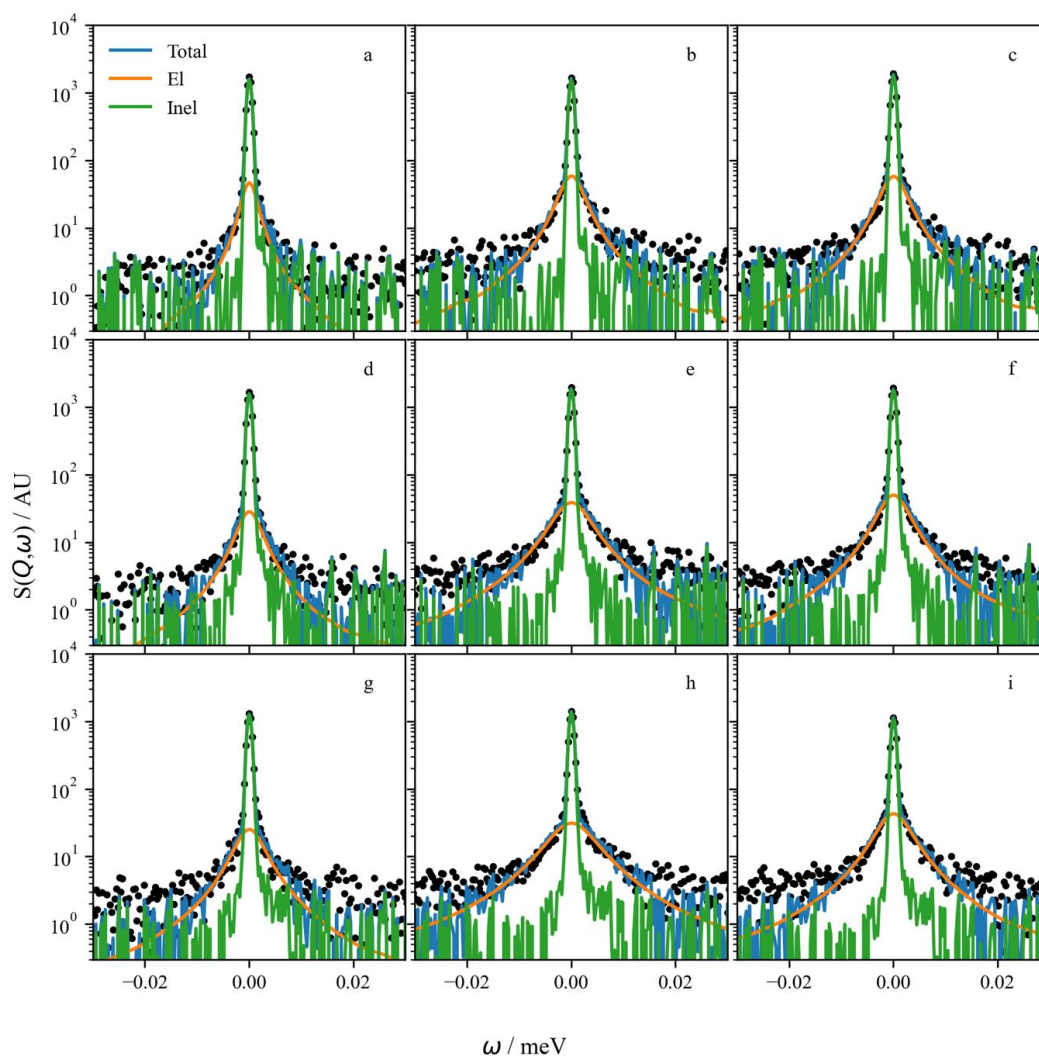


Fig. 4.3.1 Fits applied to the data from CuMOR (a, d, g); CuSSZ13 (b, e, h); and CuZSM5 (c, f, i) at 375 K for  $Q$  values of 0.4 (a,b,c), 1.0 (d, e, f) and 1.8  $\text{\AA}^{-1}$  (g, h, i).

Incoherent inelastic scattering is predominantly influenced by hydrogen atoms due to their high incoherent scattering cross-section, The motions of methanol within the experimental time window of the instrument are indicated by the presence of a Lorentzian component. The delta function accounts for the elastic scattering from both coherent sources (zeolite framework) and incoherent sources (immobile hydrogen atoms). The linewidths (HWHM,  $\Gamma$ ) of the Lorentzian component were modelled as a function of  $Q^2$  to identify the type of motion under observation. The non-linear  $Q$ -dependence of the linewidths at all temperatures suggests translational jump diffusion rather than bulk diffusion. Various models were tested, with the Singwi & Sjölander<sup>21</sup> (SS) jump diffusion model providing the best fit for the data across all temperatures (Fig 4.3.2).

The diffusion coefficients, jump lengths and residence times derived from this study are summarised in Table 4.3. The calculated jump lengths are smaller than the pore sizes of the frameworks, indicating that the diffusion observed is localised within the pores of the framework, rather than the entire cavity. Across the entire temperature range, methanol in Cu-SSZ-13 exhibits significantly higher diffusion coefficients ( $2.25 - 2.50 \times 10^{-10} \text{ m}^2 \text{ s}^{-1}$ ) than within Cu-mordenite ( $1.04 - 1.84 \times 10^{-10} \text{ m}^2 \text{ s}^{-1}$ ) and Cu-ZSM-5 ( $1.22 - 1.87 \times 10^{-10} \text{ m}^2 \text{ s}^{-1}$ ). This discrepancy is likely the result of Cu-SSZ-13 having fewer adsorption sites – approximately 3 per unit cell (PUC) as opposed to around 4 PUC in mordenite and 6 PUC in ZSM-5, as determined by the Si/Al ratio. At 300 K, the diffusion coefficients appear to correlate with the density of adsorption sites: a higher number of acid sites leads to reduced diffusivity. This reduction is attributed to increased interactions between methanol and the Brønsted acid sites (BAS) as well as Cu within the pores.

**Table 4.3 Jump lengths, residence times and diffusion coefficients for zeolite-confined methanol, derived from QENS.**

Sample	T (K)	$\sqrt{\langle l^2 \rangle}$ (Å)	$\tau_0$ (ps)	$D_s$ ( $\times 10^{-10} \text{ m}^2 \text{ s}^{-1}$ )
CuMOR	300	$2.0 \pm 0.3$	$47.8 \pm 11.0$	$1.3 \pm 0.5$
	325	$2.9 \pm 0.4$	$77.2 \pm 13.2$	$1.8 \pm 0.6$
	350	$2.9 \pm 0.4$	$76.4 \pm 12.2$	$1.8 \pm 0.6$
	375	$1.8 \pm 0.2$	$51.3 \pm 10.3$	$1.0 \pm 0.4$
CuSSZ13	300	$3.7 \pm 0.3$	$90.2 \pm 8.9$	$2.6 \pm 0.5$
	325	$3.3 \pm 0.3$	$80.8 \pm 7.2$	$2.2 \pm 0.4$
	350	$3.3 \pm 0.2$	$72.8 \pm 6.2$	$2.5 \pm 0.4$
	375	$2.7 \pm 0.2$	$53.2 \pm 5.0$	$2.3 \pm 0.4$
CuZSM5	300	$2.4 \pm 0.2$	$77.5 \pm 10.3$	$1.2 \pm 0.3$
	325	$2.7 \pm 0.2$	$81.5 \pm 9.1$	$1.5 \pm 0.3$
	350	$3.1 \pm 0.3$	$83.8 \pm 8.4$	$1.9 \pm 0.4$
	375	$2.4 \pm 0.2$	$59.6 \pm 6.3$	$1.6 \pm 0.4$

When the temperature is increased to 325 K, the diffusion coefficient of methanol increases in mordenite and ZSM-5 as anticipated. However, counterintuitively, it decreases in Cu-SSZ-13. At 350 K, the effect on methanol mobility varies further: there is minimal change observed in diffusion within Cu-mordenite, a slight reduction in residence time between jumps in Cu-SSZ-13 (from 80.83 to 72.83 ps) and a notable increase in jump length within Cu-ZSM-5 (from 2.71 to 3.07 Å).

At the highest temperature of 375 K, the most significant changes in methanol diffusivity were observed, affecting jump lengths, residence times and diffusion coefficients. All three samples showed a reduction in residence times by approximately 20 ps and a decrease in the jump lengths of up to 1.11 Å (in Cu-mordenite). Notably, the findings in this study are inconsistent with previous reports of methanol diffusion within zeolites. These include the observation of considerable variations in jump lengths across the temperature range studied; and the overall methanol diffusivity not showing a consistent temperature dependence. Specifically, neither the diffusion coefficients nor

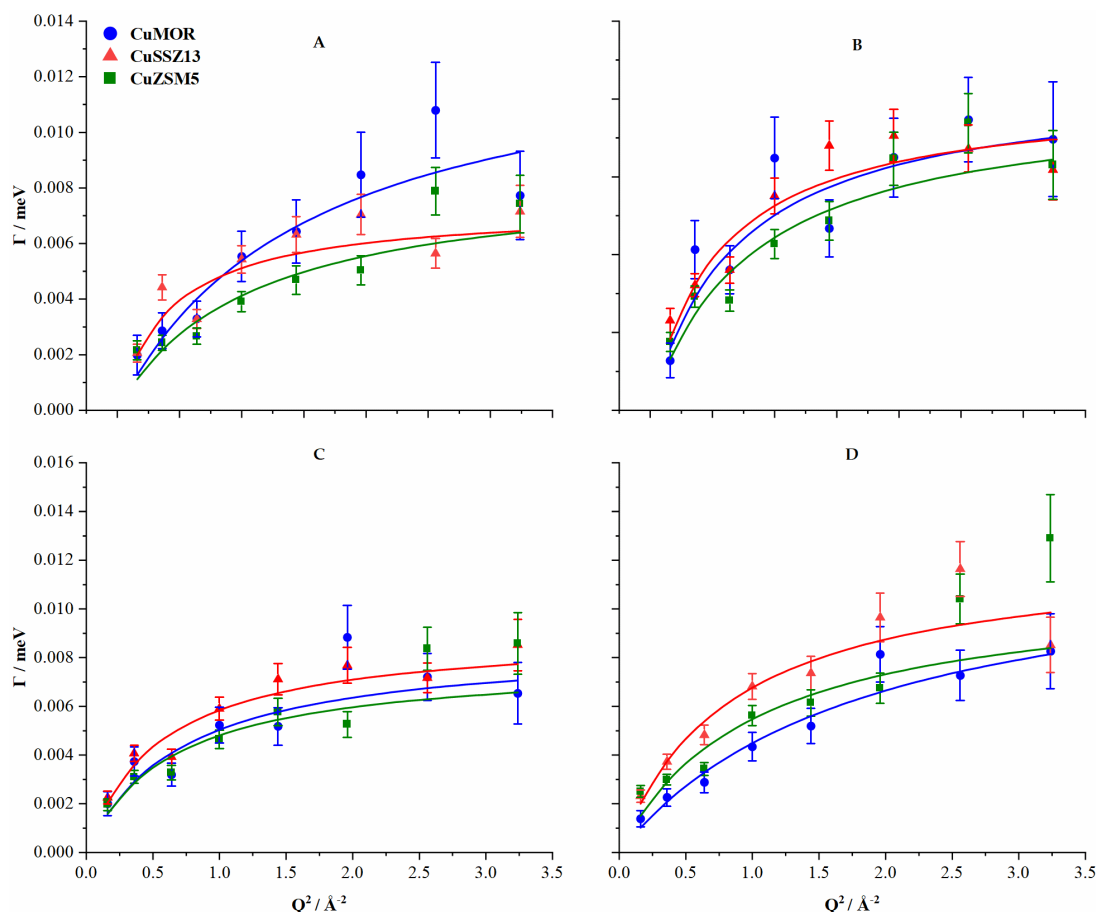


**Fig. 4.3.2** Lorentzian linewidths of the quasielastic component from the QENS spectra and the Singwi & Sjölander jump diffusion model applied. A, B, C and D correspond to data obtained at 300, 325, 350 and 375 K respectively.

the residence times follow Arrhenius behaviour when plotted against  $1/T$ . Given that the data were well-fitted using a single Lorentzian function convoluted with a delta function and the instrumental resolution, it is thus hypothesised that these discrepancies arise from at least two dynamic processes occurring within the experimental time window and operating on similar time and length scales. Two such processes may differentiate the ‘free’ and ‘bound’ or ‘activated’ methanol formed at higher temperatures. One hypothesis is that methanol adsorbed on the BAS via hydrogen bonding may dissociate to form surface methoxy groups. This process has been documented in H-ZSM-5<sup>30</sup> at room temperature, though Zachariou *et al.*<sup>31</sup> have suggested that such methoxylation requires heating to 423 K. In order to investigate this, the three methanol-dosed zeolites were subjected to inelastic neutron scattering measurements, with the spectra presented in Fig. 4.3.3. A weak, broad band around  $800\text{ cm}^{-1}$  is attributed to hydroxyl bending vibrations of hydrogen-bonded methanol. The broadness of the band suggests that hydrogen-bonded water, formed during methoxylation, might also be contributing to the signal. Sharp bands at  $1155\text{ cm}^{-1}$  and  $1450\text{ cm}^{-1}$  correspond to  $\text{CH}_3$  rocking and bending modes, respectively. A further broad band peaking at  $1580\text{ cm}^{-1}$  overlaps with the latter, attributed methyl vibration modes and low-frequency external modes of methanol. A broad band at  $3200\text{ cm}^{-1}$ , though poorly resolved due to instrumental limitations, combines CH and OH stretching vibrations in methanol.<sup>31,32</sup> The presence of bands associated with methyl rocking and hydroxyl and methyl deformation

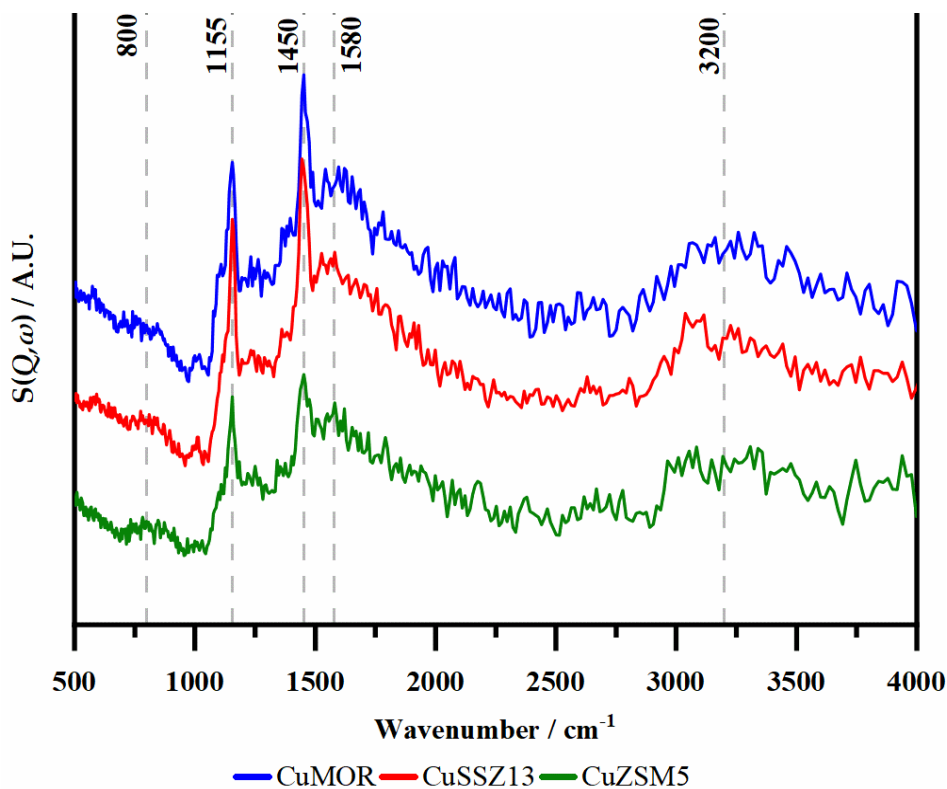


Fig. 4.3.3 INS Spectra of Methanol adsorbed on the three zeolites at 350 K.

confirms the presence of methanol. However, INS alone does not provide evidence of methoxylation, making it difficult to conclude whether methanol has dissociated. Despite the sorption temperature of 375 K being lower than the 423 K reported by Zachariou *et al.*<sup>31</sup> for methoxylation, the copper present in these materials may act as a catalyst, lowering this temperature. The quasielastic spectra suggest a combination of temperature-dependent motions, indicating that methoxy formation on the BAS is likely. The observations in this study suggest that methanol is diffusing in clusters around cationic sites with the dynamics of any methoxy groups formed occurring at similar rates, rendering their individual characterisation challenging.

#### **4.4.4 Conclusions**

QENS and INS were applied to three Cu-loaded zeolites in order to study the dynamics of methanol within these systems. The diffusion constants derived from the study are in agreement with existing literature<sup>33–35</sup> but reveal non-Arrhenius behaviour and variability in calculated jump lengths, suggesting the presence of multiple concurrent processes. INS confirmed the presence of undissociated methanol and indicated some degree of methoxy group formation, which likely contributes to the observed dynamics; with the other process identified as the clustering of undissociated methanol at cationic adsorption sites. These insights are made possible by the high-resolution capabilities of the Emu spectrometer, which affords the observation of slower processes on the molecular time and length scales. The observed complexities highlight the intricate nature of methanol diffusion in Cu-zeolites and emphasise the need for continued research and refinement of models to achieve a thorough understanding of diffusion in zeolitic materials.

### **4.5 Neutron Diffraction**

Zeolites are extensively utilised as catalysts across various industries, yet the interactions between pore walls and sorbates remain poorly understood. The confinement of sorbates within the zeolite's pores introduces steric effects that can hinder diffusion and the co-sorption of reactants. The charged framework of zeolites enables single-site catalysis through metallic cations and imparts both Lewis and Brønsted acidity, which are crucial for their function as solid acid catalysts. The effectiveness of Brønsted acid sites is influenced by the hydration level of the zeolite due to hydronium ion-water cluster formation.<sup>36</sup>

To manage this, zeolites are often subjected to hydrothermal treatment post-synthesis to dealuminate the framework. This process can either reduce the number of acid sites or enhance diffusion by opening meso- and macropores.<sup>37,38</sup> Reactions that involve or produce water can alter the catalyst's topology and chemical selectivity over time. Pertinent examples of this include the methane-to-methanol conversion which utilises water as the methanol desorption solvent; and the selective catalytic reduction of NO<sub>x</sub> with ammonia which converts toxic nitrogen oxides into nitrogen and water. Understanding how sorbates such as water affect the topology of these catalysts is therefore of considerable interest in pursuit of optimal catalytic processes.<sup>38,39</sup>

## **4.5.1 Experimental**

### **4.5.1.1 Diffraction Measurements**

The high resolution diffraction measurements were performed on the Engin-X instrument at the ISIS Neutron & Muon Source.

Commercial-grade zeolite SSZ-13 (chabazite, Si/Al = 12) was kindly supplied by Johnson Matthey. The sample was placed in a cylindrical, stainless steel reactor with a nominal diameter of 16 mm, featuring CF flanges sealed with copper gaskets. Helium gas flow was controlled via custom mass-flow control system from Bronkhorst. To achieve saturated water vapour loading, the gas was passed through a heated bubbler containing water maintained at 42 °C. Trace-heated stainless steel lines were used to direct the gas to the sample position. Data collection was performed alternately, at the front and rear of the catalyst bed, with only the rear data presented herein. To highlight the trends observed, each diffraction peak was fitted using a Gaussian function.

The zeolite was first exposed to water vapor with the reactor maintained at 47 °C. After 133 minutes, the water dosing system was bypassed and dry gas was introduced into the reactor. At 921 minutes, the sample was heated to 80 °C under a dry gas flow to facilitate desorption of water.

## **4.5.2 Results & Discussion**

Fig. 4.4.1 illustrates the time evolution of selected diffraction peaks from the zeolite catalyst, presenting both the raw data and the gaussian functions. The first red line marks the transition from water-saturated gas flow to a dry gas

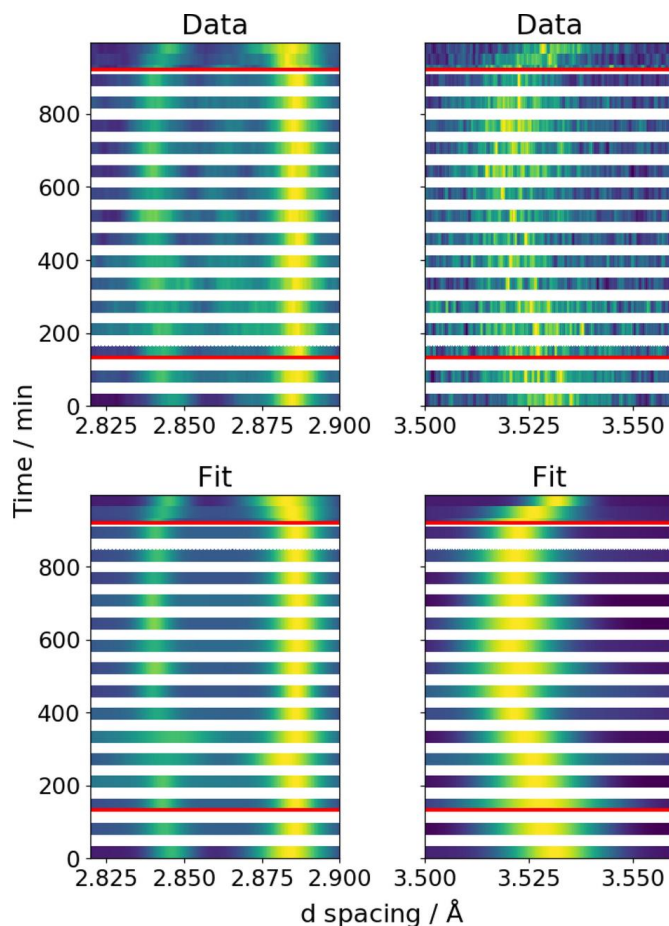


**Fig. 4.4.1** Diffraction measurement from SSZ-13 catalyst as a function of time. Lines at 133 and 921 min show the termination of water dosing and the onset of heating respectively.

glow at 133 minutes. The second red line indicates the initiation of heating to 80 °C at 921 minutes onstream.

The peak at around 3.53 Å shows the most significant response, displaying a shift to lower d-spacing during the initial water dosing. This shift persists even after bypassing the water vapour generator, continuing up to 400 minutes, suggesting a gradual diffusion of water from the zeolite's surface to its bulk; the peak position then stabilises under the given conditions. Upon heating at 921 minutes, the peak shifts back towards its initial position. In contrast, the peaks at 2.84 Å and 2.88 Å display less pronounced changes during the initial water dosing and dry flow stages. However, notable changes occur during the final heating stage. The peak at 2.84 Å follows a similar trend to the peak at 3.53 Å, whilst the peak at 2.88 Å demonstrates a contrasting effect. This behaviour highlights the anisotropic contraction of the zeolite upon water adsorption.

To further investigate this behaviour, neutron diffraction patterns of each zeolite were obtained during the QENS measurements discussed in Sections 4.1 and 4.2 (*vide supra*), presented in Fig. 4.4.2. The patterns of activated

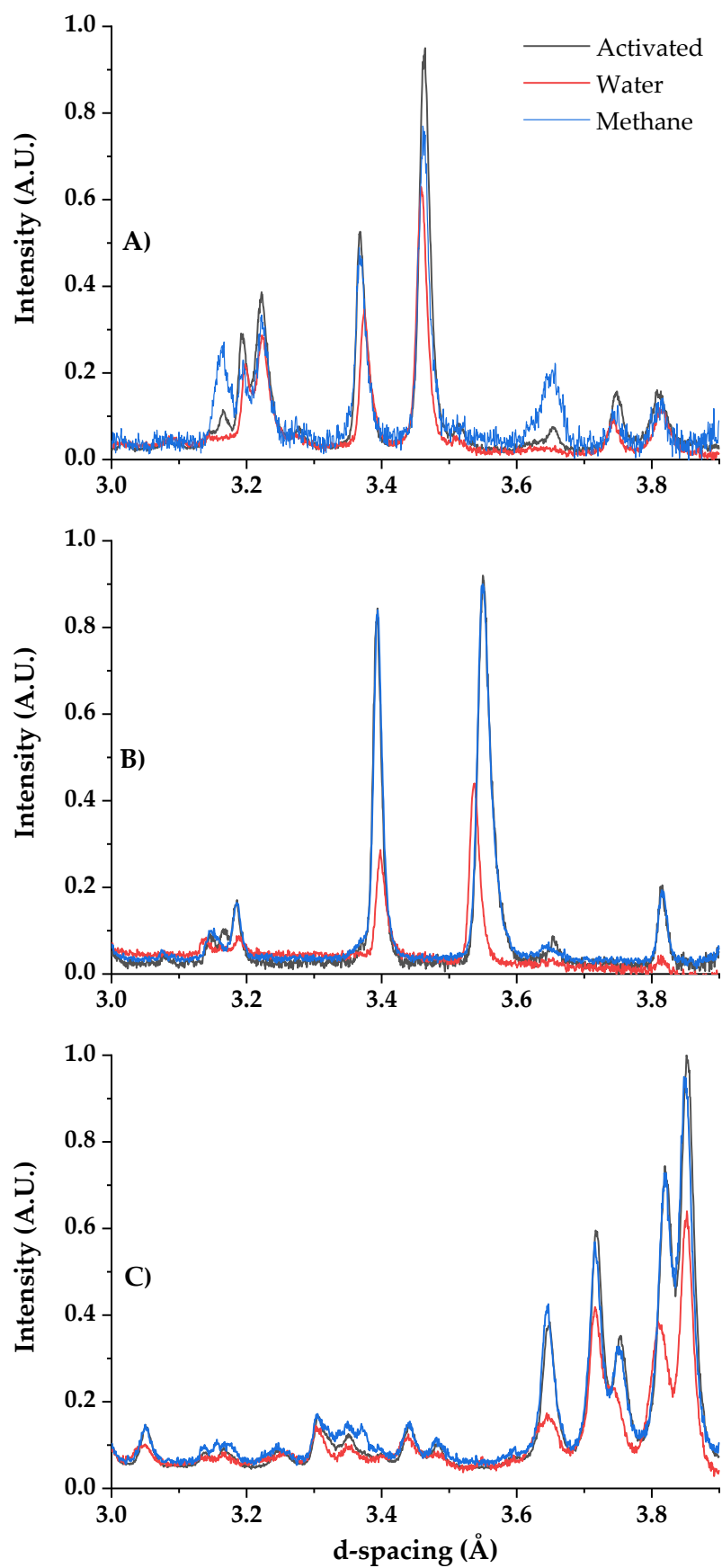


Fig. 4.4.2 Neutron diffraction patterns obtained from Cu-MOR (A), Cu-SSZ-13 (B) and Cu-ZSM-5 (C) after activation and dosing with water and methane.

zeolites as well as those after water and methane dosing were obtained and compared in order to check whether any physical changes are induced upon adsorption of the two different sorbates. For all zeolites, methane adsorption resulted in minimal changes in the diffraction patterns obtained. The most pronounced changes are at  $\sim 3.1$  Å where a slight shift in the peak position can be observed in all three samples. Upon adsorption of water, however, much more significant changes can be observed. Within Cu-mordenite, peaks at 3.1 and 3.65 Å appear diminished; the peaks at 3.2 and 3.35 Å are shifted to slightly lower d-spacing; whilst the peak at 3.3 Å is shifted to a higher d-spacing. The observations within Cu-SSZ-13 are similar, where a shift to higher d-spacing can be observed at  $\sim 3.2$  and 3.4 Å; whilst the peak position at  $\sim 3.55$  Å is moved to lower d-spacing – which is in agreement with the data obtained for the bare SSZ-13. The most minimal changes upon adsorption of water can be seen within the Cu-ZSM-5 sample, with peaks at around 3.75 and 3.8 Å slightly shifted to smaller d-spacing. In all cases however, evidence of anisotropic expansion and/or contraction are evident upon adsorption of water onto the zeolitic framework; whilst some minimal changes can be seen upon adsorption of methane. In all cases however, evidence of anisotropic expansion and/or contraction are evident upon adsorption of water onto the zeolitic framework; whilst some minimal changes can be seen upon adsorption of methane. The latter may be due to lower amounts of methane adsorbed, as discussed in the previous Section 4.2.

### 4.5.3 Conclusions

Mechanical stress in the solid phase has been shown to influence catalytic activity,<sup>40</sup> and the contraction and expansion of zeolites vary depending on the sorbate gases involved.<sup>41–43</sup> These changes in the zeolitic framework geometry can also impact the material's shape selectivity. It is crucial, therefore, to understand the mechanical and chemical effects induced by guest molecules in the pores; particularly under dynamic conditions involving co-adsorption and reaction. The results of this investigation indicate significant structural responses to water adsorption but contrasting with the minimal changes observed upon methane adsorption. The shift of diffraction peaks at various d-spacings highlights the anisotropic expansion and contraction within the zeolitic framework. These findings further underscore the zeolites' dynamic structural adaptability to different sorbates, emphasising the complex nature of optimum catalyst design for various reaction conditions.

## 4.6 Summary

The study employed QENS to investigate the dynamics of water, methane and methanol confined within three Cu-loaded zeolites. Water dynamics varied with temperature: no observable motion at 100 K; rotational dynamics at 200 K; and both rotational and translational motions at 300 K. The diffusion constants for mordenite and SSZ-13 were slower than that in bulk water due to strong interactions between water molecules and copper ions within the pores. Calculated jump lengths in mordenite and SSZ-13 were smaller than the pores of each framework, indicating localised diffusivity within water clusters at cationic sites and BAS. In Cu-ZSM-5, the rotational and translational dynamics could not be separately resolved due to their overlap.

For methane, the QENS measurements revealed no observable dynamics across all temperatures, likely due to low adsorption during the sample pretreatment. This contrasts with previous research where methane dynamics were successfully documented in similar systems, suggesting a need for optimisation of the experimental conditions.

The dynamics of methanol were also studied using QENS and INS, with the results displaying non-Arrhenius behaviour and variability in jump lengths, which is indicative of multiple concurrent processes. INS confirmed the presence of undissociated methanol and possible methoxy group formation; the results therefore likely correspond to dynamics of undissociated methanol as well as those of the methoxy groups formed.

Lastly, the study highlighted the mechanical stress induced by different sorbate gases, which has implications on the activity and shape selectivity in zeolites. The most significant structural changes were observed upon adsorption of water, while minimal changes were visible with methane adsorption. The anisotropic expansion and contraction of the zeolitic framework highlights the dynamic structural adaptability of zeolites, crucial for designing optimal catalysts for a plethora of reactions they are utilised in.

## 4.7 Bibliography

- (1) O'Malley, A. J.; Sarwar, M.; Armstrong, J.; Catlow, C. R. A.; Silverwood, I. P.; York, A. P. E.; Hitchcock, I. Comparing Ammonia Diffusion in NH<sub>3</sub>-SCR Zeolite Catalysts: A Quasielastic Neutron Scattering and Molecular Dynamics Simulation Study. *Physical*

*Chemistry Chemical Physics* 2018, 20 (17).

<https://doi.org/10.1039/c8cp01022f>.

- (2) Matam, S. K.; Catlow, C. R. A.; Silverwood, I. P.; O'Malley, A. J. Methanol Dynamics in H-ZSM-5 with Si/Al Ratio of 25: A Quasi-Elastic Neutron Scattering (QENS) Study. *Topics in Catalysis* 2021, 64 (9–12). <https://doi.org/10.1007/s11244-021-01450-z>.
- (3) Hawkins, A. P.; Zachariou, A.; Parker, S. F.; Collier, P.; Barrow, N.; Silverwood, I. P.; Howe, R. F.; Lennon, D. Effect of Steam De-Alumination on the Interactions of Propene with H-ZSM-5 Zeolites. *RSC Advances* 2020, 10 (39). <https://doi.org/10.1039/d0ra03871g>.
- (4) Corsaro, C.; Crupi, V.; Majolino, D.; Migliardo, P.; Venuti, V.; Wanderlingh, U.; Mizota, T.; Telling, M. Diffusive Dynamics of Water in Ion-Exchanged Zeolites. *Molecular Physics* 2006, 104 (4). <https://doi.org/10.1080/00268970500476131>.
- (5) O'Malley, A. J.; Catlow, C. R. A. Sorbate Dynamics in Zeolite Catalysts. In *Experimental Methods in the Physical Sciences*; 2017; Vol. 49. <https://doi.org/10.1016/B978-0-12-805324-9.00006-6>.
- (6) Mitra, S.; Sharma, V. K.; Mukhopadhyay, R. Diffusion of Confined Fluids in Microporous Zeolites and Clay Materials. *Reports on Progress in Physics*. 2021. <https://doi.org/10.1088/1361-6633/abf085>.
- (7) Jost, S.; Biswas, P.; Schüring, A.; Kärger, J.; Bopp, P. A.; Haberlandt, R.; Fritzsche, S. Structure and Self-Diffusion of Water Molecules in Chabazite: A Molecular Dynamics Study. *Journal of Physical Chemistry C* 2007, 111 (40). <https://doi.org/10.1021/jp073857s>.
- (8) Ray, M. S. Diffusion in Zeolites and Other Microporous Solids, by J. Karger and D. M. Ruthven, John Wiley, New York, USA (1992). ISBN 0-471-50907-8. *Developments in Chemical Engineering and Mineral Processing* 2008, 4 (3–4). <https://doi.org/10.1002/apj.5500040311>.
- (9) Schirmer, W. Molecular Transport and Reaction in Zeolites – Design and Application of Shape Selective Catalysis. *Zeitschrift für Physikalische Chemie* 1995, 191 (2). [https://doi.org/10.1524/zpch.1995.191.part\\_2.282](https://doi.org/10.1524/zpch.1995.191.part_2.282).
- (10) Lin, D. H.; Ducarme, V.; Coudurier, G.; Vedrine, J. C. Adsorption and Diffusion of Different Hydrocarbons in MFI Zeolite of Varying Crystallite Sizes. *Studies in Surface Science and Catalysis* 1989, 46 (C). [https://doi.org/10.1016/S0167-2991\(08\)61016-2](https://doi.org/10.1016/S0167-2991(08)61016-2).

- (11) Millot, B.; Méthivier, A.; Jobic, H.; Moueddeb, H.; Dalmon, J. A. Permeation of Linear and Branched Alkanes in ZSM-5 Supported Membranes. *Microporous and Mesoporous Materials* 2000, 38 (1). [https://doi.org/10.1016/S1387-1811\(99\)00302-9](https://doi.org/10.1016/S1387-1811(99)00302-9).
- (12) Heink, W.; Kärger, J.; Pfeifer, H.; Datema, K. P.; Nowak, A. K. High-Temperature Pulsed Field Gradient Nuclear Magnetic Resonance Self-Diffusion Measurements of n-Alkanes in MFI-Type Zeolites. *Journal of the Chemical Society, Faraday Transactions* 1992, 88 (23). <https://doi.org/10.1039/FT9928803505>.
- (13) Bée, M. *Quasielastic Neutron Scattering: Principles and Applications in Solid State Chemistry, Biology and Materials Science*; 1988.
- (14) Mukhopadhyay, R.; Mitra, S. Molecular Diffusion and Confinement Effect: Neutron Scattering Study. In *Indian Journal of Pure and Applied Physics*; 2006; Vol. 44.
- (15) Zhou, T.; Bai, P.; Siepmann, J. I.; Clark, A. E. Deconstructing the Confinement Effect upon the Organization and Dynamics of Water in Hydrophobic Nanoporous Materials: Lessons Learned from Zeolites. *Journal of Physical Chemistry C* 2017, 121 (40). <https://doi.org/10.1021/acs.jpcc.7b04991>.
- (16) Ari, M. U.; Göktug Ahunbay, M.; Yurtsever, M.; Erdem-Şenatalar, A. Molecular Dynamics Simulation of Water Diffusion in MFI-Type Zeolites. *Journal of Physical Chemistry B* 2009, 113 (23). <https://doi.org/10.1021/jp901986s>.
- (17) Commission, I. Z. A. S. *Database of zeolite structures*. Available on: <http://www.iza-structure.org/databases/> Accessed: June. [https://europe.iza-structure.org/IZA-SC/pow\\_pat.php?STC=MOR&ID=MOR\\_0](https://europe.iza-structure.org/IZA-SC/pow_pat.php?STC=MOR&ID=MOR_0) (accessed 2021-12-22).
- (18) Carlile, C. J.; Adams, M. A. The Design of the IRIS Inelastic Neutron Spectrometer and Improvements to Its Analysers. *Physica B: Physics of Condensed Matter* 1992, 182 (4). [https://doi.org/10.1016/0921-4526\(92\)90047-V](https://doi.org/10.1016/0921-4526(92)90047-V).
- (19) Arnold, O.; Bilheux, J. C.; Borreguero, J. M.; Buts, A.; Campbell, S. I.; Chapon, L.; Doucet, M.; Draper, N.; Ferraz Leal, R.; Gigg, M. A.; Lynch, V. E.; Markvardsen, A.; Mikkelsen, D. J.; Mikkelsen, R. L.; Miller, R.; Palmen, K.; Parker, P.; Passos, G.; Perring, T. G.; Peterson, P. F.; Ren, S.; Reuter, M. A.; Savici, A. T.; Taylor, J. W.; Taylor, R. J.; Tolchenov, R.; Zhou, W.; Zikovsky, J. Mantid - Data Analysis and Visualization Package for Neutron Scattering and  $\mu$  SR Experiments.

*Nucl Instrum Methods Phys Res A* 2014, 764.

<https://doi.org/10.1016/j.nima.2014.07.029>.

- (20) Azuah, R. T.; Kneller, L. R.; Qiu, Y.; Tregenna-Piggott, P. L. W.; Brown, C. M.; Copley, J. R. D.; Dimeo, R. M. DAVE: A Comprehensive Software Suite for the Reduction, Visualization, and Analysis of Low Energy Neutron Spectroscopic Data. *Journal of Research of the National Institute of Standards and Technology* 2009, 114 (6).  
<https://doi.org/10.6028/jres.114.025>.
- (21) Singwi, K. S.; Sjölander, A. Resonance Absorption of Nuclear Gamma Rays and the Dynamics of Atomic Motions. *Physical Review* 1960, 120 (4), 1093–1102. <https://doi.org/10.1103/PhysRev.120.1093>.
- (22) Sharma, V. K.; Mitra, S.; Thakur, N.; Yusuf, S. M.; Juranyi, F.; Mukhopadhyay, R. Dynamics of Water in Prussian Blue Analogues: Neutron Scattering Study. *Journal of Applied Physics* 2014, 116 (3).  
<https://doi.org/10.1063/1.4890722>.
- (23) Mitra, S.; Prabhudesai, S. A.; Chakrabarty, D.; Sharma, V. K.; Vicente, M. A.; Embs, J. P.; Mukhopadhyay, R. Dynamics of Water in Synthetic Saponite Clays: Effect of Trivalent Ion Substitution. *Physical Review E - Statistical, Nonlinear, and Soft Matter Physics* 2013, 87 (6).  
<https://doi.org/10.1103/PhysRevE.87.062317>.
- (24) Sharma, V. K.; Mitra, S.; Kumar, A.; Yusuf, S. M.; Juranyi, F.; Mukhopadhyay, R. Diffusion of Water in Molecular Magnet  $\text{Cu}_{0.75}\text{Mn}_{0.75}[\text{Fe}(\text{CN})_6]_7\text{H}_2\text{O}$ . *Journal of Physics Condensed Matter* 2011, 23 (44).  
<https://doi.org/10.1088/0953-8984/23/44/446002>.
- (25) Grifoni, E.; Piccini, G. M.; Lercher, J. A.; Glezakou, V. A.; Rousseau, R.; Parrinello, M. Confinement Effects and Acid Strength in Zeolites. *Nature Communications* 2021, 12 (1). <https://doi.org/10.1038/s41467-021-22936-0>.
- (26) Jobic, H.; Bée, M. Quasi-Elastic Neutron Scattering Study of the Dynamics of Methane Adsorbed in Na-Mordenite. *Zeitschrift für Physikalische Chemie* 1995, 189 (Part 2).  
[https://doi.org/10.1524/zpch.1995.189.Part\\_2.179](https://doi.org/10.1524/zpch.1995.189.Part_2.179).
- (27) Jobic, H.; Bée, M.; Caro, J.; Bülow, M.; Kärger, J. Molecular Self-Diffusion of Methane in Zeolite ZSM-5 by Quasi-Elastic Neutron Scattering and Nuclear Magnetic Resonance Pulsed Field Gradient Technique. *Journal of the Chemical Society, Faraday Transactions 1: Physical Chemistry in Condensed Phases* 1989, 85 (12).  
<https://doi.org/10.1039/F19898504201>.

- (28) de Souza, N. R.; Klapproth, A.; Iles, G. N. EMU: High-Resolution Backscattering Spectrometer at ANSTO. *Neutron News* 2016, 27 (2). <https://doi.org/10.1080/10448632.2016.1163985>.
- (29) Parker, S. F.; Fernandez-Alonso, F.; Ramirez-Cuesta, A. J.; Tomkinson, J.; Rudic, S.; Pinna, R. S.; Gorini, G.; Fernández Castañón, J. Recent and Future Developments on TOSCA at ISIS. In *Journal of Physics: Conference Series*; 2014; Vol. 554. <https://doi.org/10.1088/1742-6596/554/1/012003>.
- (30) O'Malley, A. J.; Parker, S. F.; Chutia, A.; Farrow, M. R.; Silverwood, I. P.; García-Sakai, V.; Catlow, C. R. A. Room Temperature Methoxylation in Zeolites: Insight into a Key Step of the Methanol-to-Hydrocarbons Process. *Chemical Communications* 2016, 52 (14), 2897–2900. <https://doi.org/10.1039/c5cc08956e>.
- (31) Zachariou, A.; Hawkins, A.; Parker, S. F.; Lennon, D.; Howe, R. F. Neutron Spectroscopy Studies of Methanol to Hydrocarbons Catalysis over ZSM-5. *Catalysis Today* 2021, 368. <https://doi.org/10.1016/j.cattod.2020.05.030>.
- (32) Schenkel, R.; Jentys, A.; Parker, S. F.; Lercher, J. A. Investigation of the Adsorption of Methanol on Alkali Metal Cation Exchanged Zeolite X by Inelastic Neutron Scattering. *Journal of Physical Chemistry B* 2004, 108 (23). <https://doi.org/10.1021/jp049819f>.
- (33) Plant, D. F.; Maurin, G.; Bell, R. G. Molecular Dynamics Simulation of Methanol in Zeolite NaY. In *Studies in Surface Science and Catalysis*; 2005; Vol. 158 B. [https://doi.org/10.1016/s0167-2991\(05\)80436-7](https://doi.org/10.1016/s0167-2991(05)80436-7).
- (34) Woodward, C. L. M.; Porter, A. J.; Morton, K. S. C.; O'Malley, A. J. Methanol Diffusion in H-ZSM-5 Catalysts as a Function of Loading and Si/Al Ratio: A Classical Molecular Dynamics Study. *Catalysis Communications* 2022, 164. <https://doi.org/10.1016/j.catcom.2022.106415>.
- (35) Botchway, C. H.; Tia, R.; Adei, E.; O'malley, A. J.; Dzade, N. Y.; Hernandez-Tamargo, C.; de Leeuw, N. H. Influence of Topology and Brønsted Acid Site Presence on Methanol Diffusion in Zeolites Beta and MFI. *Catalysts* 2020, 10 (11). <https://doi.org/10.3390/catal10111342>.
- (36) Wang, M.; Jaegers, N. R.; Lee, M. S.; Wan, C.; Hu, J. Z.; Shi, H.; Mei, D.; Burton, S. D.; Camaioni, D. M.; Gutiérrez, O. Y.; Glezakou, V. A.; Rousseau, R.; Wang, Y.; Lercher, J. A. Genesis and Stability of Hydronium Ions in Zeolite Channels. *Journal of the American Chemical Society* 2019, 141 (8). <https://doi.org/10.1021/jacs.8b07969>.

- (37) Maache, M.; Janin, A.; Lavalley, J. C.; Benazzi, E. FT Infrared Study of Brønsted Acidity of H-Mordenites: Heterogeneity and Effect of Dealumination. *Zeolites* 1995, 15 (6). [https://doi.org/10.1016/0144-2449\(95\)00019-3](https://doi.org/10.1016/0144-2449(95)00019-3).
- (38) Ma, L.; Cheng, Y.; Cavataio, G.; McCabe, R. W.; Fu, L.; Li, J. Characterization of Commercial Cu-SSZ-13 and Cu-SAPO-34 Catalysts with Hydrothermal Treatment for NH<sub>3</sub>-SCR of NO<sub>x</sub> in Diesel Exhaust. *Chemical Engineering Journal* 2013, 225. <https://doi.org/10.1016/j.cej.2013.03.078>.
- (39) Chen, H. Y.; Sachtler, W. M. H. Activity and Durability of Fe/ZSM-5 Catalysts for Lean Burn NO<sub>x</sub> Reduction in the Presence of Water Vapor. *Catalysis Today* 1998, 42 (1–2). [https://doi.org/10.1016/S0920-5861\(98\)00078-9](https://doi.org/10.1016/S0920-5861(98)00078-9).
- (40) Passos, A. R.; Rochet, A.; Manente, L. M.; Suzana, A. F.; Harder, R.; Cha, W.; Meneau, F. Three-Dimensional Strain Dynamics Govern the Hysteresis in Heterogeneous Catalysis. *Nature Communications* 2020, 11 (1). <https://doi.org/10.1038/s41467-020-18622-2>.
- (41) Ilić, B.; Wettstein, S. G. A Review of Adsorbate and Temperature-Induced Zeolite Framework Flexibility. *Microporous and Mesoporous Materials*. 2017. <https://doi.org/10.1016/j.micromeso.2016.10.005>.
- (42) Sorenson, S. G.; Smyth, J. R.; Noble, R. D.; Falconer, J. L. Correlation of Crystal Lattice Expansion and Membrane Properties for MFI Zeolites. *Industrial and Engineering Chemistry Research* 2009, 48 (22). <https://doi.org/10.1021/ie901073g>.
- (43) Gor, G. Y.; Huber, P.; Bernstein, N. Adsorption-Induced Deformation of Nanoporous Materials - A Review. *Applied Physics Reviews*. 2017. <https://doi.org/10.1063/1.4975001>.

## Attempting to Measure the Dynamics of Copper within Zeolite SSZ-13

### 5.1 Introduction

Metal ions are stabilised in specific crystallographic positions within zeolitic materials and their location is largely dependent on a combination of chemical composition, topology and the nature of the counterion. X-ray diffraction is the primary technique used to probe the location of cations in ordered materials; its application has provided an insight that copper within zeolite SSZ-13 may be migrating from the 6 membered rings to the 8 membered rings during oxygen activation.<sup>1</sup> Further evidence of copper mobility has been documented after ammonia has been shown to liberate copper from the zeolitic framework.<sup>2</sup>

Directly probing the mobility of copper ions is challenging. Paramagnetic relaxation can present problems within nuclear magnetic resonance (NMR) measurements and the low incoherent scattering cross section means advanced spectroscopy such as quasi-elastic neutron scattering (QENS) is not sensitive to this process. However, muon spin spectroscopy ( $\mu$ SR) has been shown to be an effective way for the direct study of ionic diffusion and motion.<sup>3</sup> Indeed, a molecular dynamics study by Paolucci *et al.*<sup>4</sup> revealed that copper solvated by ammonia had a hopping rate of  $6 \times 10^{-6} \text{ s}^{-1}$  at 473 K; a time window ideally suited for  $\mu$ SR measurements. Thus, this study concerns the utilisation of  $\mu$ SR in an attempt to directly observe the dynamics of copper within zeolite SSZ-13 which, to the best of the author's knowledge, is the first such application of muons in the field of zeolite catalysis.

### 5.2 Experimental

#### 5.2.1 Zeolite Preparation

The zeolites were prepared and ion-exchanged with copper as per Section 2.3.1 of Chapter 2. The sample was then dried and activated in oxygen atmosphere

at 723 K, yielding Cu-H-SSZ-13. D<sub>2</sub>O was used instead of H<sub>2</sub>O for the preparation of Cu-D-SSZ13 and D-SSZ13; with the latter ion exchanged without addition of Cu salt.

### 5.2.2 Magnetisation Measurements

Magnetisation Data were taken on a Quantum Design MPMS with a temperature range of 1.8 to 400 K and an applied field range of 0 to 7 T.

### 5.2.3 Muon Spin Spectroscopy

Muon spin spectroscopy ( $\mu$ SR) experiments were performed on the GPS spectrometer at the Paul Scherrer Insitut, Switzerland and the EMU spectrometer at the ISIS Neutron and Muon Source, UK. The different sources enable collection of complementary data; with the former offering enhanced resolution of faster frequencies and temporal scales, while the latter allows the probing of slower, dynamic behaviour. The data was analysed using both WIMDA<sup>5</sup> and MANTID.<sup>6</sup>

In a  $\mu$ SR experiment, 100% spin-polarised positive muons (also known as anti-muons, or  $\mu^+$ , which henceforth will be referred to simply as muons) are implanted into the sample. The muons subsequently undergo a radiative, three body decay, resulting in the emission of a positron and two neutrinos. This decay process occurs with an average lifetime of 2.2  $\mu$ s, with a crucial feature being the preferential emission of the positron along the direction of the muon spin at the time of its decay. Muons possess both spin and charge characteristics and are considered a light isotope of hydrogen, having a mass 1/9th that of a proton. This renders them exceptionally good local probes, capable of interacting with both electronic and nuclear spins within a radius of 2 nm. By analysing the asymmetry in positron emission, one can construct time-dependent spectra that reflect field-induced muon spin flips at the local level. Importantly, this sensitivity allows  $\mu$ SR to discern between static and dynamic phenomena with exceptional precision, rendering it a highly effective technique for investigating both types of behaviour.

Upon implantation, muons undergo thermalisation and interact with the sample in three primary ways. The first two include either a bare muon ( $\mu^+$ ) residing within the crystal structure, or the bare muon forming a dative bond with atoms or ions possessing lone pairs of electrons, commonly observed in

oxygen-muon interactions; with both of these referred to as diamagnetic muon states, or  $\text{Mu}^+$ . The third interaction involves the muon acquiring an electron during thermalisation, forming a neutral hydrogenic atom known as muonium ( $\mu^+ e^-$ ) or  $\text{Mu}^0$ . This state has the positive muon occupying the nucleus, while the electron resides in a 1s orbital, akin to the energy level diagram of hydrogen. The hyperfine interaction between the muon and the electron renders muonium an exceptionally sensitive probe of local fields. In all cases, muons or muonium may diffuse or bond with diffusible species.<sup>7,8</sup>

### 5.3 Results & Discussion

Muon spin spectroscopy experiments measure the decoherence of a muon ensemble through three distinct measurements. The first is the transverse field (TF) measurement, where a magnetic field is applied perpendicular to the initial muon polarisation. This causes the muon spins to precess around the applied TF at a frequency directly proportional to the applied field, as described by the following relationship:

$$\nu = \frac{\omega_\mu}{2\pi} = \frac{\gamma_\mu B}{2\pi}$$

where  $\nu$  is the precessional frequency,  $\omega_\mu$  the Larmor (angular) frequency,  $\gamma_\mu$  the gyromagnetic ratio of the muon and  $B$  the magnitude of the field at the muon site. Any broadening in the field distribution, arising from static or dynamic electronic or nuclear behaviour, results in a relaxation of the precessional signal. Crucially, the presence of muonium leads to rapid depolarisation under high applied fields, manifesting as a missing asymmetry, or a missing fraction. Thus, TF measurements primarily capture diamagnetic muon behaviour. In the second type of measurement, no external magnetic field is applied and the sample is measured under zero-field (ZF) conditions. Any dephasing of the muon polarisation or asymmetry is caused by the interactions between the muon spin and the local electronic and nuclear magnetism. Lastly, a longitudinal field (LF) can be applied along the initial muon polarisation to decouple the muon spin from its local environment and internal fields; a recovery of the muon polarisation can be observed when the applied LF is comparable with the internal magnetic fields.

Given the muon spin's sensitivity to local magnetism, nuclear fields can swamp small signals from the nuclei of interest. To differentiate between the behaviour of the Cu and that of hydrogen, the samples were deuterated as

deuterium has a nuclear moment an order of magnitude smaller than hydrogen.

### 5.3.1 Transverse Field (TF) $\mu$ SR

To probe the states and processes observed by the diamagnetic muons, a measurement in 100 G TF was performed on all three samples, Cu-D-SSZ13, Cu-H-SSZ13 and D-SSZ13, as a function of temperature. These measurements are akin to performing a T2 spin-spin relaxation experiment. The relaxation rate of the muon spin provides insights into the temperature-dependent behaviour of the field distribution, with broadening indicating the initiation of dynamic processes or increasing levels of disorder. The data obtained was fitted using the functional form:

$$G(t) = A \cos(\gamma_{\mu} Bt + \phi) \exp(-\lambda t) + A_{Base}$$

where  $A$  is the relaxing asymmetry,  $\lambda$  is the decay rate,  $\phi$  the phase and  $A_{Base}$  the background that accounts for any non-relaxing muons stopping in the sample cell. Fig. 5.1 illustrates the variations of both the relaxing asymmetry and the relaxation rate as a function of temperature. A quick examination of the data reveals a distinction in the behaviour between the Cu-zeolites and the pure SSZ-13. The relaxing asymmetry in both the Cu-H and Cu-D systems follows a consistent trend and comparable values, suggesting that the processes affecting the relaxation of diamagnetic muons are consistent and distinct from those in SSZ-13. Additionally, the relaxation rates of the Cu-H and Cu-D samples exhibit a similar qualitative trend but differ in absolute

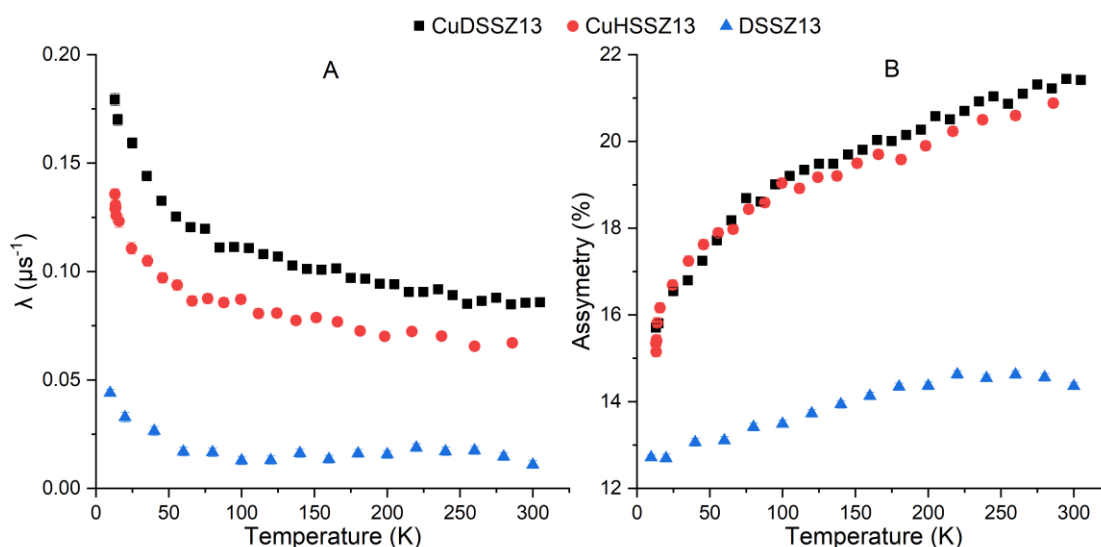


**Fig. 5.1 Relaxation rates ( $\lambda$ ) and the initial asymmetries (%) obtained from the three zeolite samples as a function of temperature, measured in 100 G TF.**

values, likely due to variations in the field distribution due to the presence of deuterium or hydrogen. Referring to Fig. B, the diverse range of asymmetry values serves as an indication of varying quantities or proportions of muons existing in the diamagnetic state. A complete fraction of muons on the EMU spectrometer is considered to be approximately 28%. Consequently, the missing fraction observed in all cases is attributed to the presence of muonium, as the applied TF induces a rapid depolarisation of this state, which is outside of our time window. The variation of the relaxing asymmetry in the Cu-H and Cu-D samples across the temperature range studied is striking: at higher temperatures, muonium formation appears to be reduced; whilst an increase in the muonium fraction and the accompanied reduction in the relaxing asymmetry can be seen upon cooling (higher proportion of missing asymmetry and higher relaxation at low temperature). Noteworthy is the reduction in relaxing asymmetry accelerating upon cooling below 100 K and again below 25 K, which indicate three distinct temperature regions of interest, also reflected in the relaxation rate.

In the case of DSSZ-13, the relaxing asymmetry reaches a plateau at around 200 K, with minimal variations at higher temperatures. The decreasing asymmetry with decreasing temperature is also indicative of muonium formation; again, this is mirrored in the relaxation rate, however one should note that the qualitative shape of these curves is different from those of Cu-doped samples, so the dominant processes is likely to be different.

As the muon thermalises within a sample, prompt muonium can often be formed and it can either remain in this state, or it can further decay into a muon through ionisation. This transition has been documented in semiconductors and has recently been outlined by Vilão *et al.*<sup>9</sup> In the case of silicon, the prompt muonium is trapped within a transitional state. Depending on the energy barrier involved, it can either transition to a bound muonium state or become ionised, leading to a diamagnetic muon state; with the process likely to be thermally mediated. If the energy barrier for the diamagnetic state exceeds that for the bound muonium state, the pathway towards the diamagnetic state becomes more probable at higher temperatures, resulting in a larger diamagnetic fraction. As temperature decreases, the probability of forming the ionised state diminishes, reaching a point where it becomes unfavourable or even impossible. This threshold is likely around 100 K within the Cu-H and Cu-D systems, preventing muonium conversion to the diamagnetic state. Consequently, below this temperature, the asymmetry rapidly decreases, and the relaxation rate increases as the transition process slows down. This observation is consistent with our data; the gradual rise in the relaxation rate shown in Fig. 5.1A reflects the slower transition of  $\text{Mu}^0$  to the ionised  $\text{Mu}^+$ . At

the inflection point around 100 K, muonium remains in its initial state without ionisation with a drop in asymmetry, indicating that, at this temperature, there is insufficient energy to drive  $\text{Mu}^0$  towards the  $\text{Mu}^+$  state, since it is a thermally activated process, and it is commensurate with an excited state within the sample freezing out. Therefore, the hypothesis is that the divergence, observed below 25 K, in the Cu-containing systems is due to the onset of magnetism related to the Cu(II) species (*vide infra*).

### 5.3.2 Longitudinal Field (LF) $\mu\text{SR}$

Given that both the muon and muonium's interaction with their surrounding environment is resonant, it is possible to either decouple this interaction or adjust the resonance condition. When the muon is decoupled from its local environment, there is a noticeable recovery of the asymmetry, offering valuable information on the state and the coupling of the muon or muonium with the surrounding electronic and nuclear fields. Additionally, by increasing the LF, one can modify the resonance condition so the muon/muonium is sensitive to a different part of the spectral density within frequency space, with the muon spin relaxation rate,  $\lambda \propto J(\omega_0, \tau)$ , where  $\omega_0 = \gamma_\mu B$  and  $\tau$  is the characteristic timescale. Therefore, as the LF is increased, the value of  $\lambda$  can provide information on the fluctuations present within the system, where you essentially perform a resonance experiment. Fig. 5.2 shows the asymmetries and relaxation rates at base temperature and at 305 K. The recovery of the asymmetry with increasing LF provides insight into the proportion of

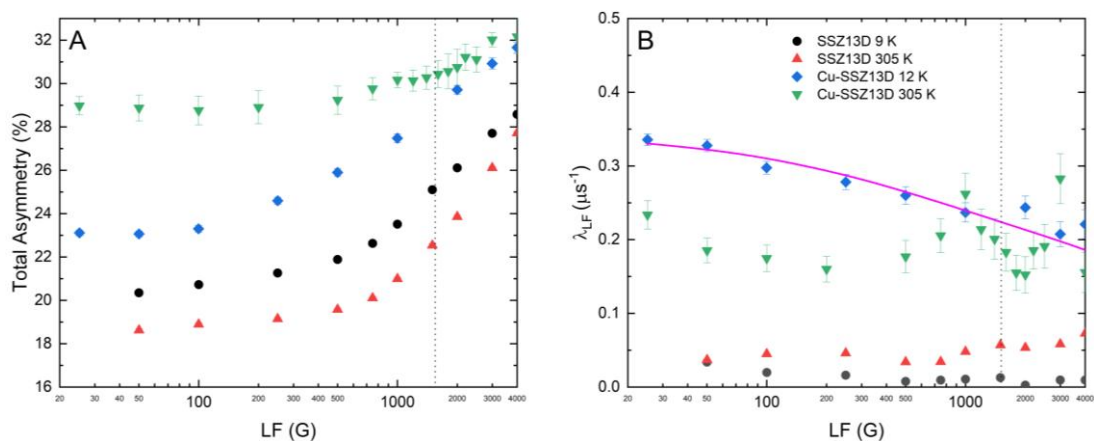


**Fig. 5.2 A: Asymmetry as a function of longitudinal field (the datasets have been offset for clarity). The dashed line shows the expected midpoint of the recovery in asymmetry for vacuum state muonium. B: the muon spin relaxation rate as a function of longitudinal field. The fit to the data for the CuSSZ-13D is described in the text that describes the diffusion of the muonium.**

muonium formed and an estimation of the hyperfine coupling between the  $\mu^+$  and  $e^-$ . Figure 2A illustrates that the magnitude of asymmetry recovery for the Cu-D-SSZ13 sample varies at high and low temperatures, consistent with observations from the TF data shown in Figure 5.1. Inflections within the recovery can provide estimates of anisotropic and isotropic parts of the hyperfine coupling constants. In the data presented in Figure 5.1A, a lack of low-field recovery suggests the muonium is isotropic with no anisotropy. Indeed, the midpoint of recovery, at approximately 1500 G (hyperfine constant = 4463 MHz) and shown by the dashed line in Figure 5.2A, is consistent with the characteristics of isotropic vacuum state muonium. This trend is mirrored for the pure zeolite, D-SSZ13, albeit with a greater amount of muonium formed and only minute temperature variation, again consistent with the observations from the TF data within Fig. 5.1. As the LF is increased, the frequency of the dynamics probed by the muon or muonium also rises. It may be anticipated that if the same or similar processes are influencing the relaxation of the muon, then the LF dependence of  $\lambda$  should exhibit similarity; however, there is a vast disparity between the D-SSZ13 and the Cu-D-SSZ13 samples. In the bare zeolite, a contrast in the magnitude of the value of  $\lambda$  is observed between the high and low temperatures, however there is very little field dependence which suggests that the muonium is not being relaxed by its local environment; thus, it is difficult to provide any detail on the interaction between the muonium and the host material (the zeolite). Nonetheless, in the case of Cu-D-SSZ13, the trends of  $\lambda$  at 12 K and 305 K are disparate. At 12 K, the reduction in  $\lambda$  coupled with the restoration of asymmetry – attributable to isotropic muonium – suggests that the decline is the result of LF altering resonance conditions associated with the muonium and its local environment. The change in  $\lambda$ , and thus the spectral density, can be modelled to understand the dimensionality of muonium diffusion. Generally, for a muonium atom which contains both isotropic and anisotropic coupling to its local environment,  $\lambda$  can be described as:

$$\lambda = \frac{A^2}{4} J(\omega_e) + \frac{D^2}{4} \left[ \frac{7J(\omega_e) + 3J(\omega_\mu)}{5} \right]$$

where  $A$  and  $D$  are the isotropic and the anisotropic parts of the hyperfine coupling, respectively; whilst  $J(\omega_e)$  and  $J(\omega_\mu)$  are the spectral densities associated with the electron and the muon, respectively. If  $D \ll A$ , then the second term in equation the above equation can be ignored, essentially probing the local environment through coupling of the electron within the muonium atom. If the muonium is able to diffuse, then one must consider the time evolution of the correlation between the muonium and its local environment, which is described by:

$$S(t) = \prod_{i=1}^3 e^{-2D_i t} I_0(2D_i t)$$

where  $I_0(x)$  is the zeroth order, modified Bessel Function and  $D_i$  represents diffusion along either a faster, lower energy, parallel direction ( $D_{\parallel}$ ) or a slower, higher energy, perpendicular direction ( $D_{\perp}$ ). In the case of different dimensionalities:

$$D_1 = D_{\parallel}, D_2, D_3 = D_{\perp} \text{ (1 Dimensional)}$$

$$D_1, D_2 = D_{\parallel}, D_3 = D_{\perp} \text{ (2 Dimensional)}$$

$$D_1, D_2, D_3 = D_{\parallel} \text{ (3 Dimensional)}$$

and by taking the Fourier transform of the autocorrelation function for each dimensionality,

$$J(\omega) = 2 \int_0^{\infty} S(t) \cos(\omega t) dt$$

one arrives at an equation that describes the field dependence of  $\lambda$  as a function of longitudinal field, that has a power law dependence,  $t^{-d/2}$ , where  $d$  is the dimensionality. Therefore, in the case of 1D, 2D and 3D spin diffusion, one expects field dependencies of  $B^{-1/2}$ ,  $B^{-1}$  and  $B^{-3/2}$ , respectively.

The low-temperature data obtained from Cu-SSZ13D (Figure 2B) is best modelled using a 2D spin diffusion model (where  $A = 118(2)$  MHz,  $D_{\parallel} = 14520(10)$  MHz and  $D_{\perp} = 50(20)$  MHz) which describes muonium undergoing stochastic motion across a two-dimensional surface. Its polarisation is lost through coupling to electronic and nuclear moments in its local environment, which may arise through contact or dipolar, hyperfine interactions. Within the pores of a zeolite, a cylinder with a sufficiently large diameter may appear as a two-dimensional surface over which the muonium is able to randomly diffuse. It is key that this behaviour is lost at 305 K and neither of the two peaks, present in the data, correspond to the midpoint of the muonium repolarisation (marked by the dashed line in Figure 2B). Thus, we postulate that the muonium is tuning into different processes through the different resonance conditions engendered when the LF is swept and, as previously discussed, the muon's spin is relaxed through a T1 relaxation with the spin of the electron.

### 5.3.3 Temperature Dependence in ZF and LF

It is clear from the previous sections that there is a substantial difference in the muons' response to the pure and the Cu-doped SSZ-13. To further understand the temperature dependent dynamics within these systems, spectra were collected in zero-field and at predetermined longitudinal fields. As the LF is adjusted, the muon is decoupled from its local environment and the resonance conditions are altered, allowing different frequencies to be probed. At higher fields, the diamagnetic muons are decoupled, and the measured relaxation is primarily attributed to muonium – which is typically relaxed by faster processes – allowing access to a faster time-window. In all cases, the muon spectra were fitted using a single exponential relaxation and a baseline, enabling the determination of the relaxing asymmetry, the muon spin relaxation rate,  $\lambda$ , and the baseline. The fastest-time data, which is dominated by a muonium T1 relaxation, could not be reliably fitted due to insufficient temporal resolution afforded by the spectrometer, therefore all data were fit from 0.5  $\mu\text{s}$  onwards.

Fig. 5.3 shows the behaviour of  $\lambda$  for the deuterated and hydrogenated Cu-SSZ13 as well as the deuterated-SSZ13, as a function of temperature. The pure

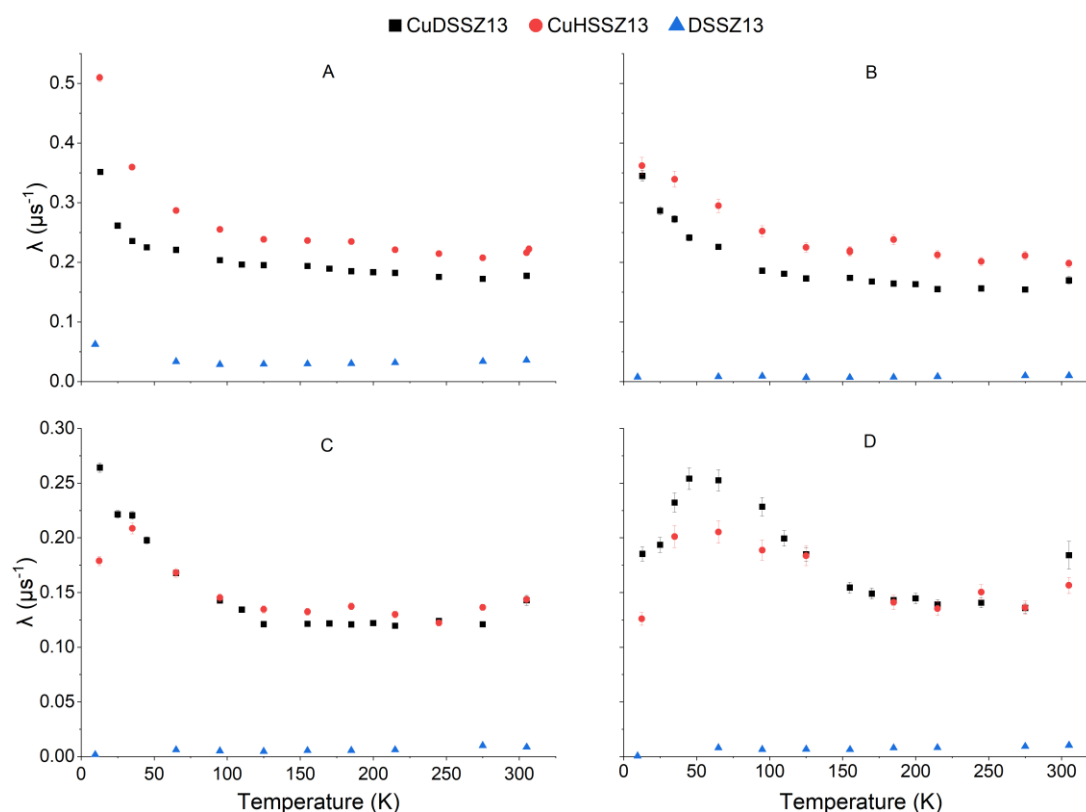


**Fig. 5.3 Muon spin relaxation rates at zero-field (A) and longitudinal fields of 50 G (B), 500 G (C) and 2000 G (D) as a function of temperature for the Cu-DSSZ13, Cu-HSSZ13 and the DSSZ13.**

DSSZ13 shows very little temperature dependence and a much smaller magnitude of  $\lambda$  when compared to the Cu-containing samples. The general trend of  $\lambda$  is similar for both Cu-DSSZ13 and Cu-HSSZ13, however the difference in their values suggests that the diamagnetic muons, which will dominate the relaxation in lower magnetic fields, are likely bound to sites containing either a proton or a deuteron, thereby altering the field distribution. An example of this would be a Bronsted acid site, where either O-H or O-D groups exist. It is widely acknowledged that the diamagnetic muons will bond to lone pairs on oxygen atoms, resulting in highly stable muon sites.

At zero field (ZF) there is no external magnetic field applied, allowing the study of intrinsic muon interactions without external perturbations. Figure 5.3A shows the behaviour of the relaxation rate ( $\lambda$ ) in zero field. The data indicate a noticeable decline in  $\lambda$  as the temperature increases, reaching a plateau between 50 and 100 K. This suggests the system transitions to a motionally narrowed state, where the relaxation rate remains constant. The increase in  $\lambda$  with decreasing temperature correlates with a decrease in asymmetry and an increase in relaxation observed in transverse field (TF) measurements (Figure 5.1). Thus, the increase in relaxation at lower temperatures may be due to the conversion between paramagnetic and diamagnetic muons freezing out. The pure deuterated SSZ13 shows minimal temperature dependence and a much smaller magnitude of  $\lambda$  compared to the Cu-containing samples, indicating different relaxation dynamics in the absence of Cu.

At 50 G (Fig. 5.3B), the applied LF decouples the muons from the local nuclear magnetic fields (such as those of protons or deuterons). This reduces the influence of nuclear spins on the muons. With nuclear fields decoupled, muons are more responsive to electronic magnetic moments, like those from Cu(II) ions. The data show a temperature-dependent relaxation rate ( $\lambda$ ) that plateaus above 50 K, indicating a stable electronic environment at these temperatures. Diamagnetic muons are sensitive to dynamic processes involving electronic moments, such as those associated with Cu(II) ions; the conversion process between  $\text{Mu}^0$  and  $\text{Mu}^+$  may therefore involve the Cu(II) ions. Furthermore, the qualitative differences in the 50 G LF data between the deuterated and protonated samples suggests that the muons may be static, rather than freely able to diffuse.

At the higher LF of 500 G, muons are further decoupled from nuclear magnetic fields, focusing their sensitivity on faster electronic fluctuations. The increased field strength makes muons sensitive to faster dynamic processes, such as rapid spin flips of Cu(II) ions. The relaxation rate ( $\lambda$ ) is lower at 500 G than at 50 G, due to muons interacting with different spectral densities of magnetic

fluctuations. The dynamic processes at this field strength involve faster electronic fluctuations, resulting in less overall muon relaxation. The relaxation behaviour at 500 G further indicates that Cu(II) clusters are involved in the relaxation processes, evidenced by the similar trends seen at 50 G but with different magnitudes. In both Cu-containing samples an anomaly emerges at approximately 30 K, and this is also evident in the TF data. This anomaly likely arises from the freezing of the electronic magnetism within the Cu(II) clusters (*vide infra*).

As the LF reaches 1500 G, the missing fraction associated with the rapid depolarisation of muonium is at the mid-point of recovery. Thus, at 2000 G LF (Fig. 5.3D) one is above the midpoint of the recovery of the muonium polarisation and in the regime probing the spin-lattice,  $T_{1\mu}$ , relaxation associated with the electron on the  $\text{Mu}^0$ . This field strength probes even faster dynamic processes, such as the spin-flip of the electron on the  $\text{Mu}^0$  atom, resulting in muon spin dephasing. The higher field allows for the examination of rapid fluctuations within the Cu-SSZ13 systems. Data suggest that in Cu-SSZ13 systems, the  $\text{Mu}^0$  atom undergoes 2D spin diffusion through the material's pores, with interactions with Cu(II) moments likely causing muonium spin depolarisation. This indicates strong interactions with Cu-active sites at various temperatures. The peak in  $\lambda$  at this field suggests a process entering the measurement time window.

There are two possible scenarios that could be responsible for the increase in relaxation as the temperature reaches 75 K. Firstly, we may be probing a low-energy local rotation or translation of Cu ions, which would imply the Cu active species in the zeolite's pores is mobile to some extent, even at such low temperatures. A second possibility is that we are probing the redox properties of copper, i.e. the Cu(II) accepts an electron from the muonium, to produce a muon and Cu(I). Copper has been shown to auto-reduce even under inert atmosphere during high temperature treatment,<sup>10</sup> which has been observed for Cu-SSZ-13 in the present study (see Section 3.3 in Chapter 3); the reactivity of the muonium may facilitate this process at much lower temperatures. Moreover, these processes may not be mutually exclusive. Andersen *et al.*<sup>11</sup> examined the effects of Cu oxidation state and the distribution thereof within zeolite SSZ-13 by employing a quasi-simultaneous application of XRD and XANES. Their findings revealed a direct correlation between the reduction of Cu(II) to Cu(I) and the migration of these ions from the larger, more accessible 8-membered rings to the smaller, double-6 ring structures, characteristic of the chabazite topology. Our findings, therefore, may be probing both the reduction of Cu(II) and the resultant migration of the copper species.

### 5.3.4 Magnetisation Data

To understand the low temperature  $\mu$ SR data, the magnetisation of the deuterated sample was measured as a function of applied field. Figure 5.4A illustrates sweeps of magnetisation versus applied field at different temperatures. Both the magnitude of the magnetisation and the general behaviour is markedly different between the Cu-doped and the bare SSZ-13 (Fig. 5.4D). This discrepancy strongly suggests that the presence of Cu(II) ions is responsible for these variations. In Fig. 5.4A, the observed magnetisation versus applied field curves align with expectations at higher temperatures where, despite the linear trend indicating the paramagnetic limit, the susceptibility (defined as the slope of  $M/H$ , with  $H$  representing the magnetic field strength) appears to undergo changes. Generally, the magnetisation of small magnetic clusters (where  $J \rightarrow \infty$ ) can be well described by the Langevin function, defined as:

$$M = N\langle m \rangle \mu_B \left( \coth(y) - \frac{1}{y} \right)$$

where

$$y = \frac{\langle m \rangle \mu_B}{k_B T}$$

With  $N$  being the number density of the magnetic moments and  $\langle m \rangle$  the average value of the magnetic moment. Therefore, the data within Figure 5.4A, should scale on a plot of  $M$  vs.  $B/T$ , (see Fig. 5.4B). Given that the data do not directly scale, this is an indication that the number density is changing with temperature. A fit to the lowest temperature resulted in a value of the moment of  $3 \mu_B$ . This is a reasonable value for a cluster of Cu(II) ions since a single Cu ion would result in a moment of approximately  $1.4 \mu_B$ . Given the small moment, the cluster is likely to contain a small number of ions, perhaps even two. This description of the data has been reliably used to delineate small Ni(II) clusters;<sup>12</sup> and other research has documented the copper active sites consisting of small Cu(II) clusters such as dimers and trimers.<sup>13</sup> By keeping the moment fixed at  $3 \mu_B$ , all of the data within Fig 5.4B can be fitted with variation of  $N$ ; and the resultant values are shown in Fig. 5.4C. As the temperature increases, so does  $N$ , with a plateau around 20 K. The low temperature increase in  $N$  is due to the Cu(II) clusters entering a state where the magnetism

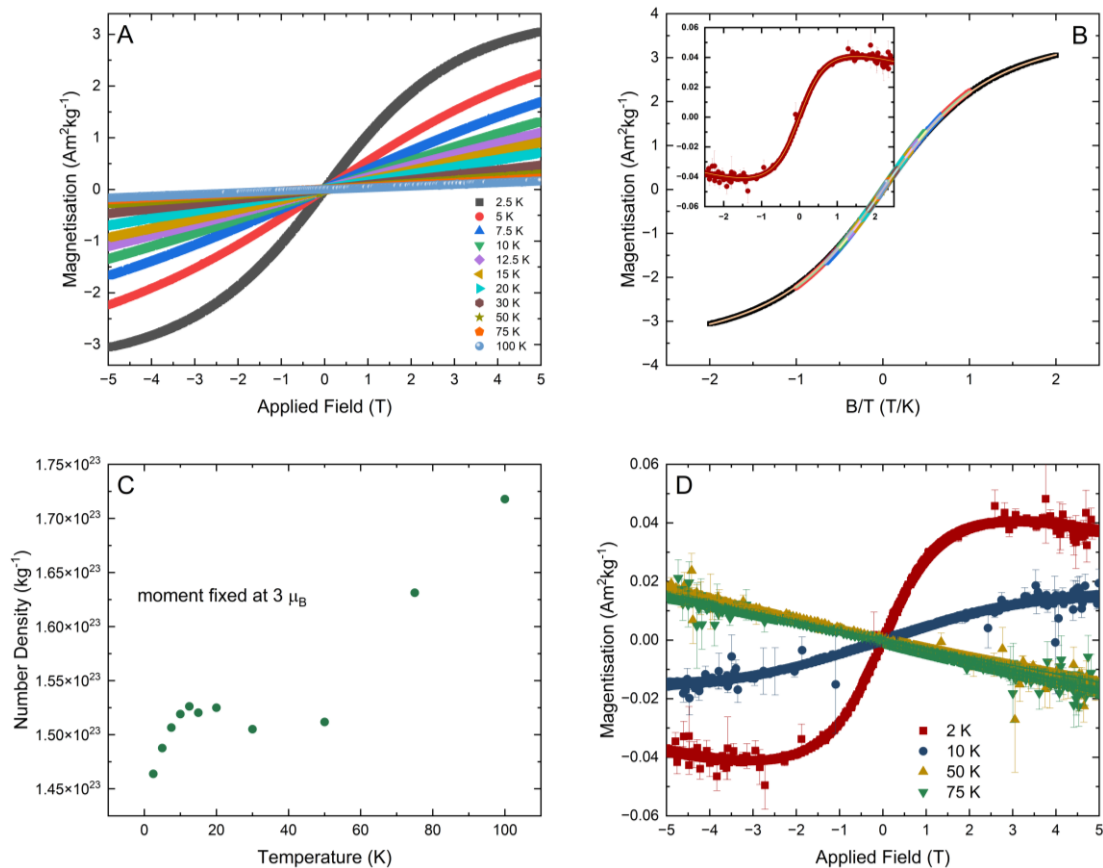


**Fig. 5.4** Data showing the magnetisation of both the deuterated Cu-SSZ13 and the deuterated SSZ13. **A:** The magnetisation vs. applied field for the deuterated Cu-SSZ13 at different temperatures; **B:** magnetisation plotted against  $B/T$ , allowing the datasets to be scaled with the solid lines showing fits to the data using a Langevin function as described within the text; **C:** plots the number density from the fits in graph B; and **D:** the magnetisation as a function of applied field for the deuterated SSZ13 (with no Cu doping) with the inset in graph B showing the 2 K magnetisation data vs  $B/T$  with a fit to the Langevin function that is described within the text.

is no longer frozen, for example if the Cu(II) clusters were changing from an antiferromagnetic to a paramagnetic state. The plateau at 20 K provides an estimate of the interaction, or exchange, of energy between the Cu(II) ions and above this,  $N$  increases rapidly, as the system enters the paramagnetic limit and Curie's law becomes dominant. To fit the magnetisation data of DSSZ13 at 2 K (within the inset of Fig. 5.4B), a higher moment of  $5.01(1) \mu_B$  was extracted, with  $N = 1.43(8) \times 10^{21} \text{ kg}^{-1}$  and in order to produce a reliable fit, a linear component was added. This accounted for a diamagnetic component which began to dominate at high field. Again, the values required for the fits are different from that of the Cu-DSSZ13.  $N$  is orders of magnitude smaller, and this is representative of the lack of Cu(II) within the sample. The inherent difference between the Cu-SSZ13 and the SSZ13 demonstrates that the behaviour observed within Fig. 5.4 A, B and C, is due to the presence of Cu(II);

and that the Cu(II) ions form clusters of an extremely small size, which is commensurate with suggestions from other research.<sup>14</sup>

## 5.4 Conclusions

The use of muon spectroscopy to investigate copper dynamics within zeolite SSZ-13 introduces a novel method for exploring the behaviour of metal ions within zeolitic materials. The transverse field measurements have revealed marked variations in the relaxation rate of muons in Cu-doped SSZ-13 compared to the pure zeolite, indicating dynamic processes associated with Cu ions. Observations of muonium formation and its temperature dependence suggest interactions with Cu(II) ions, especially below 100 K; and these findings imply that the transition between muonium states is influenced by the electronic and magnetic environment of the Cu(II) ions. Further longitudinal field measurements have shown that muonium undergoes two-dimensional spin diffusion, which align with the zeolite geometry. Magnetisation measurements have confirmed the presence of Cu clusters and the temperature-dependant LF data indicates processes involving Cu ions, such as their motion, reduction or both. These findings underscore the complexity of investigating copper dynamics but highlight the potential of  $\mu$ SR as a tool for studying metal ion behaviour in zeolites.

## 5.5 Bibliography

- (1) Beale, A. M.; Lezcano-Gonzalez, I.; Slawinski, W. A.; Wragg, D. S. Correlation between Cu Ion Migration Behaviour and DeNO<sub>x</sub> Activity in Cu-SSZ-13 for the Standard NH<sub>3</sub>-SCR Reaction. *Chemical Communications* 2016, 52 (36), 6170–6173. <https://doi.org/10.1039/c6cc00513f>.
- (2) Paolucci, C.; Parekh, A. A.; Khurana, I.; Di Iorio, J. R.; Li, H.; Albarracin Caballero, J. D.; Shih, A. J.; Anggara, T.; Delgass, W. N.; Miller, J. T.; Ribeiro, F. H.; Gounder, R.; Schneider, W. F. Catalysis in a Cage: Condition-Dependent Speciation and Dynamics of Exchanged Cu Cations in Ssz-13 Zeolites. *J Am Chem Soc* 2016, 138 (18). <https://doi.org/10.1021/jacs.6b02651>.
- (3) McClelland, I.; Johnston, B.; Baker, P. J.; Amores, M.; Cussen, E. J.; Corr, S. A. Muon Spectroscopy for Investigating Diffusion in Energy

- Storage Materials. In *Annual Review of Materials Research*; 2020; Vol. 50, pp 371–393. <https://doi.org/10.1146/annurev-matsci-110519-110507>.
- (4) Paolucci, C.; Khurana, I.; Parekh, A. A.; Li, S.; Shih, A. J.; Li, H.; Di Iorio, J. R.; Albarracin-Caballero, J. D.; Yezerets, A.; Miller, J. T.; Delgass, W. N.; Ribeiro, F. H.; Schneider, W. F.; Gounder, R. Dynamic Multinuclear Sites Formed by Mobilized Copper Ions in NO<sub>x</sub> Selective Catalytic Reduction. *Science* 2017, 357 (6354), 898–903. <https://doi.org/10.1126/science.aan5630>.
  - (5) Pratt, F. L. WIMDA: A Muon Data Analysis Program for the Windows PC. *Physica B: Condensed Matter* 2000, 289–290. [https://doi.org/10.1016/S0921-4526\(00\)00328-8](https://doi.org/10.1016/S0921-4526(00)00328-8).
  - (6) Arnold, O.; Bilheux, J. C.; Borreguero, J. M.; Buts, A.; Campbell, S. I.; Chapon, L.; Doucet, M.; Draper, N.; Ferraz Leal, R.; Gigg, M. A.; Lynch, V. E.; Markvardsen, A.; Mikkelsen, D. J.; Mikkelsen, R. L.; Miller, R.; Palmen, K.; Parker, P.; Passos, G.; Perring, T. G.; Peterson, P. F.; Ren, S.; Reuter, M. A.; Savici, A. T.; Taylor, J. W.; Taylor, R. J.; Tolchenov, R.; Zhou, W.; Zikovskiy, J. Mantid - Data Analysis and Visualization Package for Neutron Scattering and  $\mu$  SR Experiments. *Nucl Instrum Methods Phys Res A* 2014, 764. <https://doi.org/10.1016/j.nima.2014.07.029>.
  - (7) Stephen J. Blundell, Roberto De Renzi, Tom Lancaster, and F. L. P. *Muon Spectroscopy: An Introduction*; Oxford University Press: Oxford, 2021.
  - (8) Hillier, A. D.; Blundell, S. J.; McKenzie, I.; Umegaki, I.; Shu, L.; Wright, J. A.; Prokscha, T.; Bert, F.; Shimomura, K.; Berlie, A.; Alberto, H.; Watanabe, I. Muon Spin Spectroscopy. *Nature Reviews Methods Primers*. 2022. <https://doi.org/10.1038/s43586-021-00089-0>.
  - (9) Vilão, R. C.; Alberto, H. V.; Ribeiro, E. F. M.; Gil, J. M.; Weidinger, A. Muonium Reaction in Semiconductors and Insulators: The Role of the Transition State. In *Journal of Physics: Conference Series*; 2023; Vol. 2462. <https://doi.org/10.1088/1742-6596/2462/1/012056>.
  - (10) Sushkevich, V. L.; Smirnov, A. V.; Van Bokhoven, J. A. Autoreduction of Copper in Zeolites: Role of Topology, Si/Al Ratio, and Copper Loading. *Journal of Physical Chemistry C* 2019, 123 (15). <https://doi.org/10.1021/acs.jpcc.9b00986>.
  - (11) Andersen, C. W.; Borfecchia, E.; Bremholm, M.; Jørgensen, M. R. V.; Vennestrøm, P. N. R.; Lamberti, C.; Lundegaard, L. F.; Iversen, B. B. Redox-Driven Migration of Copper Ions in the Cu-CHA Zeolite as

Shown by the In Situ PXRD/XANES Technique. *Angewandte Chemie - International Edition* 2017, 56 (35).  
<https://doi.org/10.1002/anie.201703808>.

- (12) Berlie, A.; Terry, I.; Szablewski, M. A Magnetic Study of Low Moment Nickel Clusters Formed from the Solid-State Decomposition Reaction of Nickel Bis-1,5-Cyclooctadiene. *Journal of Cluster Science* 2013, 24 (4).  
<https://doi.org/10.1007/s10876-013-0597-9>.
- (13) Newton, M. A.; Knorpp, A. J.; Sushkevich, V. L.; Palagin, D.; Van Bokhoven, J. A. Active Sites and Mechanisms in the Direct Conversion of Methane to Methanol Using Cu in Zeolitic Hosts: A Critical Examination. *Chemical Society Reviews*. 2020.  
<https://doi.org/10.1039/c7cs00709d>.
- (14) Deplano, G.; Martini, A.; Signorile, M.; Borfecchia, E.; Crocellà, V.; Svelle, S.; Bordiga, S. Copper Pairing in the Mordenite Framework as a Function of the CuI/CuII Speciation. *Angewandte Chemie - International Edition* 2021, 60 (49). <https://doi.org/10.1002/anie.202109705>.

### 6.1 Conclusions

The investigation into the dynamics of species relevant to the partial oxidation of methane within Cu-loaded mordenite, SSZ-13 and ZSM-5 zeolites began with material characterisation and the evaluation of their efficacy in carrying out the methane-to-methanol conversion. This initial assessment ensured that the prepared zeolites accurately represented the catalysts commonly employed for this reaction, setting the stage for the subsequent exploration of the dynamics taking place within these materials.

The development of an effective methodology was initially undertaken using the Hiden Catlab microreactor. While this setup showed potential for carrying out the methane-to-methanol conversion, it was afflicted by technical difficulties, particularly with maintaining the integrity of the gas flow and temperature controls. Persistent blockages and equipment failures resulted in significant downtime and hindered the acquisition of reliable data. The approach was thus shifted to using a custom-built multi-capillary reactor designed for X-ray absorption spectroscopy experiments. Despite initially promising results, this setup too encountered challenges, namely the temperature controls, which further delayed the acquisition of meaningful results. These setbacks necessitated further experimental method development.

To overcome these challenges, diffuse reflectance Fourier transform infrared spectroscopy (DRIFTS) was employed to study the surface species formed during the partial oxidation of methane in operando. The zeolite framework modes dominated the spectra below  $2000\text{ cm}^{-1}$ , while distinct O-H stretching modes were observed above  $3500\text{ cm}^{-1}$ , indicating Brønsted acid sites, silanol groups and extra-framework aluminium. Contamination was identified through  $\text{CO}_2$  bands before methane introduction. Upon methane exposure, characteristic C-H stretching and bending vibrations were evident across all samples. Notably, a sharp absorption band at  $2153\text{ cm}^{-1}$ , corresponding to Cu(I) monocarbonyl, was prominent in Cu-SSZ-13, with varying intensity in other zeolites, aligning with the later CO adsorption findings. Nonetheless, it was not possible to determine any methanol produced via the reaction, whether quantitatively or qualitatively, which underscored the importance of

condition optimisation, leading to further experimentation with a custom built setup.

The custom-built reactor setup, comprising a small tube furnace, portable mass-flow controls and a mass spectrometer, was ultimately used to effect the methane-to-methanol conversion. This setup enabled simple yet effective control of experimental parameters such as gas flow rates and methanol desorption conditions; i.e., 5  $\mu\text{L}$  pulses of water, resulting in successful methanol production from all three Cu-loaded zeolites. Cu-mordenite showed the highest activity, with methanol production of 17.80  $\mu\text{Mol/g}_{\text{cat}}$  during the first cycle, while Cu-ZSM-5 showed the lowest activity. The study found that higher copper loading and lower Si/Al ratios correlated with increased catalytic activity, as these factors are crucial for enabling the stabilisation of Cu active sites. Notably, the study demonstrated that the catalysts were stable over five consecutive reaction cycles, with no significant decrease in methanol production. The study also explored the role of water in this reaction, finding that water could act as a soft oxidant, albeit its effectiveness was limited at ambient pressure. The omission of high-temperature activation led to a marked decrease in methanol production – especially within zeolites mordenite and SSZ-13 – indicating that high-temperature pretreatment is critical for the dehydration of the zeolite and regeneration of the active sites. The activity of each zeolite, deduced in this study, was lower than those in many reports. Nonetheless, the focus of the research remained on understanding the dynamics of the species involved rather than maximising methanol yield.

Further characterisation of the materials revealed the occurrence of autoreduction, where Cu(II) spontaneously converts to Cu(I) at elevated temperatures under inert conditions. This was confirmed through DRIFTS after high temperature activation in oxygen-free atmosphere and subsequent addition of CO probe. XANES measurements carried out at different points of the reaction (activation, reaction and extraction) were also in agreement with literature that a mixture of Cu(I) and Cu(II) species is present after reaction. The XANES analysis of the samples post-methanol extraction showed that water is able to re-oxidise Cu(I) back to Cu(II); though the resulting Cu(II) species were less active for methanol conversion, as found during the catalytic testing experiments. These findings highlight the complex relationship between copper speciation and resultant catalytic activity.

Structural changes within the zeolites were also examined, namely dealumination, through  $^{27}\text{Al}$  NMR spectroscopy. The results suggested that dealumination occurred in Cu-loaded mordenite and SSZ-13, particularly after repeated reaction cycles, while ZSM-5 showed greater stability.

Interestingly, the dealumination did not adversely affect the catalytic activity, suggesting that this process may occur in regions of the framework which are not directly involved in methane activation. These findings point to a much more nuanced relationship between structural integrity and catalytic performance than was initially anticipated. Specifically, it was expected that altering the zeolite framework through dealumination would decrease the catalytic activity since the aluminium sites in the zeolite are often linked to the active sites critical for reactions. However, the findings herein suggest that the active sites essential for methane activation are either unaffected by dealumination or are located elsewhere in the framework, where aluminium is not removed. This challenges the simple correlation between structural changes and catalytic performance, revealing that the zeolite's catalytic efficiency can be maintained even when certain parts of the structure are modified.

The primary focus of the research, however, was the exploration of the dynamics of methane, methanol, water and copper within the three zeolites. Notably, while the original intention was to conduct these measurements *in situ* or *operando* to capture real-time catalytic conditions, the complexities introduced by the COVID-19 pandemic necessitated that these experiments be performed *ex situ* in order to simplify the experimental conditions and adhere to access limitations at central facilities.

The study of water dynamics within the three Cu-loaded zeolites revealed some important insights into how the zeolitic environment influences the mobility of water molecules. At low temperatures (100 K), no detectible motions were observed, indicating that water molecules are effectively immobile on the time-scale of the instrument used. As the temperature increased to 200 K, rotational dynamics became evident, with the different Cu-zeolites displaying varying rotational times, primarily influenced by the cation content and cavity size. The most significant finding was the translational motion observed at 300 K, where the diffusion constants for mordenite and SSZ-13 were markedly slower than bulk water. This was attributed to the strong interactions between water molecules and Cu ions, which hindered the movement between adjacent sites. The smallest pore size and highest cation concentration in SSZ-13 resulted in slowest diffusivity, underlining the importance of pore size and cation concentration in influencing water mobility within these materials. Although it is not possible to determine which effects – pore size or cation concentration – are stronger in the present work, this finding leaves scope for further studies to delineate their individual contributions to water diffusivity in such systems.

The investigation of methane dynamics within the same systems revealed a lack of observable motion across the entire temperature range studied (100–300 K). The absence of detectible dynamics was likely due to insufficient methane adsorption, possibly caused by sample loss during pretreatments, or inherently low methane uptake by the zeolites under the experimental conditions used. This contrasts with previous studies on sodium-based zeolites, which successfully observed methane diffusion, suggesting that the type of cation present and the experimental conditions used have significant effects on methane adsorption and mobility. These findings indicate that further optimisation of experimental parameters, including pretreatment processes and measurement conditions, is of paramount importance in order to enhance methane adsorption and enable a successful study of its dynamics within these systems.

The dynamics of methanol within Cu-zeolites were characterised by complex trends which did not follow the anticipated Arrhenius behaviour. The QENS measurements revealed non-Arrhenius behaviour, with variations in jump lengths and residence times indicating the presence of multiple concurrent processes. INS spectra confirmed the presence of undissociated methanol and suggested some degree of methoxy group formation; with the presence of copper in the zeolites likely catalysing methoxylation at lower temperatures than typically reported. The observed methanol dynamics are likely a combination of clustering around cationic sites and the formation of methoxy groups, which occur at similar rates, complicating the separation and characterisation of these processes. These findings highlight the intricate nature of methanol diffusion within zeolites and underscore the need for further research to fully understand the mechanisms involved.

Neutron diffraction studies complemented the dynamics measurements by revealing how the zeolitic framework responds to the adsorption of water and methane. The former induced significant structural changes, characterised by anisotropic expansion and contraction of the zeolite framework, with peak shifts observed at various d-spacings. In contrast, methane adsorption caused minimal structural changes, likely due to the low amount of methane adsorbed. These structural adaptations of the zeolitic framework to different sorbates emphasise the material's dynamic nature and its potential impact on catalytic reactions, particularly in reactions where co-adsorption and mechanical stress play crucial roles. Such adaptability might affect the stability and selectivity of the catalyst, potentially altering reaction pathways or product distribution. On the one hand, this dynamic behaviour could be useful, allowing the zeolite to optimise its structure for different reactants, thereby enhancing efficiency; or enable the catalyst to perform under a broader

range of conditions. On the other hand, excessive structural flexibility could lead to degradation over time, reduced specificity, or unexpected side reactions due to unpredictable nature of the framework under varying conditions. Thus, understanding and controlling these structural adaptations may be critical for optimising catalytic performance for the partial oxidation of methane and beyond.

Lastly, the application of muon spin spectroscopy to investigate Cu dynamics within zeolite SSZ-13 represents a novel approach to understanding the dynamic behaviour of metal ions within zeolitic hosts. The transverse field measurements showed that the relaxation rate of muons in Cu-doped SSZ-13 is significantly different from that in the pure zeolite, with variations suggesting the presence of dynamic processes associated with Cu ions. The observation of muonium formation and its temperature-dependence provides evidence of the interactions between muonium and the Cu(II) species, particularly below 100K. This temperature dependency suggests that the transition between muonium states is influenced by the electronic and magnetic environment of the Cu(II) ions. The longitudinal field (LF) measurements further corroborated the findings and revealed muonium undergoing two-dimensional spin diffusion, consistent with the geometry of the zeolite pores. This aligns with the inherent structure of zeolites, where diffusion is largely confined within the two-dimensional planes of the pore channels. Given the three-dimensional nature of the zeolite framework, however, this suggests that the muonium's movement is restricted to two dimensions within each pore channel, without interaction between adjacent channels in the third dimension. This confinement within the 2D planes may be the result of the pore size, shape or orientation, which together influence the overall diffusion dynamics within the 3D structure. Moreover, the data obtained from LF measurements across different temperatures have indicated a process involving Cu ions coming into the experimental time window, with the said process being the dynamics of Cu ions or the reduction of Cu-ions via oxidation of  $\text{Mu}^0$  to  $\text{Mu}^+$ , or both. While the observation of Cu dynamics remains challenging, this study illustrates the potential of  $\mu\text{SR}$  as a powerful probe for studying metal ion behaviour in zeolites. The findings not only enhance the understanding of Cu-doped zeolites but also suggest that  $\mu\text{SR}$  may offer opportunities for direct observation of the redox behaviour of copper within these systems and beyond.

## 6.2 Future Work

Building on the findings of this study, several key areas for future research are warranted to further explore and elucidate the dynamics of methane, methanol, water and copper within Cu-loaded zeolites and to address the limitations encountered in this study. A central focus for future work should be the implementation of *in situ* or operando quasielastic neutron scattering (QENS) experiments. The inability to do so during the present study due to experimental constraints highlights a critical gap in the pursuit to understand the dynamics taking place during the methane-to-methanol conversion. *In situ* QENS would enable the observation of dynamic processes in real-time, under actual catalytic conditions, providing a comprehensive understanding of the diffusion mechanisms taking place. This approach would facilitate a more accurate characterisation of the dynamics involved in the partial oxidation of methane and enhance the correlation between dynamic behaviour and catalytic performance.

In addition to *in situ* measurements, it is crucial to address the technical challenges experienced with the initial experimental setup. The issues with temperature controls and gas flow in the Hiden Catlab microreactor and the custom-built multi-capillary reactor suggest a need for refinement in experimental techniques. Future work should focus on improving these setups in order to ensure acquisition of reliable and reproducible data. Optimisation of reaction conditions is another critical area. The inability to detect methanol production in early experiments highlights the need for refining of reaction parameters. Future studies should explore a broader range of temperatures and pressures, e.g., by using high-pressure reactors, to identify optimal conditions for methanol synthesis. Systematically varying copper loading and Si/Al ratios in the zeolites could also help elucidate the factors that influence catalytic activity and stability, with the goal of maximising methanol yield and identifying permutations that enhance catalytic performance.

The structural integrity of zeolites, particularly regarding dealumination and its effects on catalytic activity is another important area for future research. Investigating the relationship between structural changes and catalytic performance in more depth could reveal new ways in which the stability and efficiency of a catalyst could be improved. Additionally, exploring the impact of dealumination on the distribution and accessibility of active sites may provide insights into maintaining or enhancing catalytic activity despite structural modifications. A notable finding from this study was the anisotropic expansion and contraction of the zeolite framework upon sorbate adsorption, observed through neutron diffraction. The distinct structural responses to

water and methane adsorption further highlight the zeolites' dynamic nature. Future work should involve a deeper exploration of how these structural adaptations influence catalytic reactions. Research could focus on how structural flexibility influences reaction pathways, stability and selectivity, potentially leading to the design of more robust catalysts.

Investigating the dynamics of water, methane and methanol within the zeolites revealed complexities that warrant further investigation. Future work should focus on optimising experimental conditions to enhance methane adsorption which would enable the subsequent observation of its mobility; potentially by revisiting pretreatment processes and adapting the measurement times. Detailed studies on the role of pore size and cation concentration in influencing the mobility of water could provide clearer insights into their individual effects, helping delineate their contributions to catalytic performance. Additionally, investigating the interactions between water and other species, such as methanol, under varied conditions may offer new perspectives on optimising the catalyst performance and reaction pathways. Methanol dynamics were characterised by non-Arrhenius behaviour, highlighting multiple processes taking place. Further QENS and INS studies over a broader temperature range should help to elucidate whether copper does indeed catalyse methoxylation; and may enable to resolve the dynamics of the disparate processes taking place.

The novel application of muon spin spectroscopy ( $\mu$ SR) to study Cu dynamics presents an exciting avenue for further research. Future investigations should aim to refine the  $\mu$ SR techniques to better understand the dynamic behaviour of Cu ions within zeolites. This could involve probing different temperature ranges and experimental conditions to observe how Cu ions interact with the zeolite framework. Additionally, extending  $\mu$ SR studies to other metal ions and zeolite hosts could provide broader insights into metal ion dynamics and redox processes within these materials.

In conclusion, while progress has been made in understanding the dynamics taking place within Cu-loaded zeolites, there remain numerous areas for further investigation. Addressing the challenges identified in this study and exploring new experimental techniques will be essential for advancing our understanding of zeolite catalysis and improving the efficiency and effectiveness of these important materials.